

INFORMATION TO USERS

This manuscript has been reproduced from the microfilm master. UMI films the text directly from the original or copy submitted. Thus, some thesis and dissertation copies are in typewriter face, while others may be from any type of computer printer.

The quality of this reproduction is dependent upon the quality of the copy submitted. Broken or indistinct print, colored or poor quality illustrations and photographs, print bleedthrough, substandard margins, and improper alignment can adversely affect reproduction.

In the unlikely event that the author did not send UMI a complete manuscript and there are missing pages, these will be noted. Also, if unauthorized copyright material had to be removed, a note will indicate the deletion.

Oversize materials (e.g., maps, drawings, charts) are reproduced by sectioning the original, beginning at the upper left-hand corner and continuing from left to right in equal sections with small overlaps. Each original is also photographed in one exposure and is included in reduced form at the back of the book.

Photographs included in the original manuscript have been reproduced xerographically in this copy. Higher quality 6" x 9" black and white photographic prints are available for any photographs or illustrations appearing in this copy for an additional charge. Contact UMI directly to order.

UMI

A Bell & Howell Information Company
300 North Zeeb Road, Ann Arbor MI 48106-1346 USA
313/761-4700 800/521-0600

**AN INVESTIGATION ON HEAT TRANSFER
DURING THE FREEZING OF CONDENSATE DROPLETS**

A Dissertation

by

YING GONG

Submitted to the Office of Graduate Studies of
Texas A&M University
in partial fulfillment of the requirements for the degree of

DOCTOR OF PHILOSOPHY

May 1996

Major Subject: Mechanical Engineering

UMI Number: 9634745

**UMI Microform 9634745
Copyright 1996, by UMI Company. All rights reserved.**

**This microform edition is protected against unauthorized
copying under Title 17, United States Code.**

UMI
300 North Zeeb Road
Ann Arbor, MI 48103

**AN INVESTIGATION ON HEAT TRANSFER
DURING THE FREEZING OF CONDENSATE DROPLETS**

A Dissertation

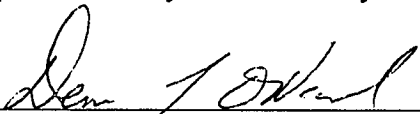
by

YING GONG

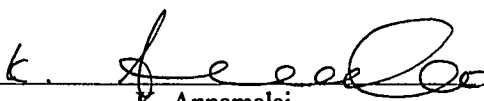
Submitted to the Office of Graduate Studies of
Texas A&M University
in partial fulfillment of the requirements for the degree of

DOCTOR OF PHILOSOPHY

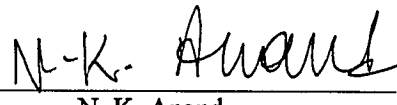
Approved as to style and content by:




D. L. O'Neal
(Chair of Committee)




K. Annamalai
(Member)



N. K. Anand
(Member)



Y. A. Hassan
(Member)



G. P. Peterson
(Head of Department)

May 1996

Major Subject: Mechanical Engineering

ABSTRACT

An Investigation on Heat Transfer
during the Freezing of Condensate Droplets. (May 1996)

Ying Gong,

B.S., Jiaotong University at Xian, China;

M.S., Jiaotong University at Xian, China

Chair of Advisory Committee: Dr. Dennis L. O'Neal

The heat transfer and the freezing process of condensate droplets resting on a cold metal plate have been studied both experimentally and numerically.

The experimental part of the investigation dealt with the measurements of the thermal and flow parameters and the visualization of the freezing process. The parameters which were varied include the ambient air velocity, air-to-plate temperature difference, and the droplet size. The tests performed were the steady-state temperature distribution, transient cooling curve at a location within a droplet, freezing time, average air-side convection coefficient on a cold metal plate covered with droplets, and freezing front motion on the freezing of droplets. Two new dimensionless numbers have been introduced to account for the freezing time and the air-side convection coefficient. Two empirical correlations, one for freezing time and the other for the average air-side convection coefficient, were developed.

A mathematical model based on control volume method was developed to calculate the temperature distributions, heat transfer rates, and phase-change region position during the freezing of hemispherical droplets on a cold metal plate. The model predictions of the freezing of a hemispherical droplet showed that the narrow ring around the droplet perimeter was a good place for continued ice nucleation. The basic structure of a frost layer was composed of two zones: the ice sublayer and the dendritic layer.

The results predicted by the mathematical model have been compared with available analytical solutions, previously published results, and experimental data. The good agreements indicated that the model could be used to predict steady-state and transient temperature distribution, temperature history, freezing front velocity, and freezing time. Combined with other softwares, the mathematical model could also be used to graphically simulate the freezing process.

Dedicated to my parents
Xiangshan Gong and Lanzhen Han

ACKNOWLEDGMENTS

I wish to express my sincere gratitude to Professor Dennis L. O'Neal, who supervised this research, for his many constructive criticisms and his encouragement through the course of the investigation. I thank the other members of my advisory committee, Dr. N. K. Anand, Dr. K. Annamalai, Dr. Y. A. Hassan, and Dr. J. F. Hunter (GCR) for their assistance.

During the experimental study, Dr. John A. Bryant helped setup the test loop for me. I appreciate his unselfish assistance and ingenious ideas. I also thank the fellow graduate students, William Vance Payne, II and Brandon D. Parker, with whom I've been associated while here at Texas A&M University. Their valuable assistance helped immensely.

This experimental work was conducted at the Energy Systems Laboratory of Texas A&M University. I thank all of the technicians who helped me fix the equipment problems.

I would like to thank my wife, Youhong, for her love and understanding. She has been a constant source of encouragement. I have also benefited from her questions and subsequent discussions.

I would like to express thanks to my parents, father and mother-in-law for their understanding and support.

TABLE OF CONTENTS

	Page
ABSTRACT	iii
DEDICATION	v
ACKNOWLEDGMENTS	vi
TABLE OF CONTENTS	vii
LIST OF FIGURES	x
LIST OF TABLES	xvii
LIST OF IMAGES	xviii
 CHAPTER	
I INTRODUCTION	1
1.1 Contribution of This Study	5
1.2 Scope of Investigation	7
II LITERATURE REVIEW	9
2.1 Frost Formation	10
2.2 Temperature Field	15
2.3 The Phase-Change Region Position	20
2.4 The Air-Side Convection Coefficient	22
2.5 Mathematical Methods on Freezing Problems	26
2.6 Summary	29
III MATHEMATICAL MODEL DEVELOPMENT	32
3.1 The Problem	32
3.2 Assumptions	33
3.3 Governing Equations and Discretization	34
IV MATHEMATICAL MODEL RESULTS	54
4.1 Model Predictions	54

TABLE OF CONTENTS (CONTINUED)

CHAPTER	Page
4.2 Grid Sensitivity and Program Validation	83
4.3 Summary	91
V EXPERIMENTAL SETUP	94
5.1 Test Setup	94
5.2 Instrumentation	99
5.3 Experimental Procedure	103
VI EXPERIMENTAL RESULTS AND DATA REDUCTION	107
6.1 Dimensional Analysis	108
6.2 Freezing Time	111
6.3 The Average Air-Side Convection Coefficient	116
6.4 Shape and Velocity of the Freezing Front	123
6.5 Temperature Field	127
6.6 Summary	134
VII COMPARISON OF EXPERIMENTAL AND MODEL RESULTS	135
7.1 Steady-State Temperature Distributions and Nodal Temperature History	135
7.2 Freezing Front Velocity	139
7.3 Freezing Front Position and the Area Fraction of Solid	141
7.4 Freezing Time	142
VIII CONCLUSIONS AND RECOMMENDATIONS	150
8.1 Background and Statement of the Problem	150
8.2 Mathematical and Experimental Investigations	151
8.3 Mathematical Model	152
8.4 Experimental Work	153
8.5 Recommendation for Further Research	155
NOMENCLATURE	157
REFERENCES	159
APPENDIX A EXPERIMENTAL DATA	166

TABLE OF CONTENTS (CONTINUED)

	Page
APPENDIX B EXPERIMENTAL UNCERTAINTY ANALYSIS.....	170
VITA	179

LIST OF FIGURES

FIGURE	Page
1.1 The frost formation on a typical fin of uniform cross section	3
2.1 The average and local convection coefficients	23
3.1 The schematic of the problem	33
3.2 Cross section of one fourth of a two-dimensional spherical region containing a medium at two physical states.	34
3.3 The grid generation for a hemispherical droplet in spherical coordinates.....	37
3.4 A control volume, $r^2 \cos(\theta) \cdot dr \cdot d\theta \cdot 2\pi r \cdot \cos(\theta)$, for conduction analysis in spherical coordinates (r, θ, ϕ)	37
3.5 An interior node and its neighbor nodes	40
3.6 Three kinds of boundary conditions encountered in a droplet	40
3.7 The magnified boundary node and its neighbor nodes.....	42
3.8 The boundary node and its neighbor nodes at the symmetric plane	42
3.9 A node at the phase change region and its adjacent nodes	46
3.10 The flowchart for computational process	51
3.11 The definition of the velocity of the freezing front.....	53
4.1 The temperature distribution in radial direction	56
4.2 The local heat flux through the surface of a droplet.....	56
4.3 Local heat transfer at the surface of a hemispherical droplet.....	58
4.4 The temperature distribution in angular direction	58
4.5 The local heat flux through the base of the droplet	59

LIST OF FIGURES (CONTINUED)

FIGURE	Page
4.6 Local heat transfer at the base of a hemispherical droplet.	59
4.7 Single droplet model of Hurst (1966).....	60
4.8 The temperature distribution in radius direction for limiting case ($h \rightarrow \infty$).....	60
4.9 The temperature distribution in angular direction for limiting case ($h \rightarrow \infty$).....	62
4.10 The local heat flux through the base of a droplet for the limiting case.....	62
4.11 The steady-state temperature distribution in radial direction of a droplet in the solid phase.	63
4.12 The steady-state angular temperature distribution of a droplet in the solid phase	63
4.13 The heat flux through the surface of a droplet in the solid phase.....	65
4.14 The heat flux through the base of a droplet in the solid phase.....	65
4.15 The transient temperature distribution ($r/R=0.68$)	67
4.16 The temperature distribution at the surface of a droplet during freezing ($r/R=1$).....	67
4.17 The positions inside a droplet at which the temperature distributions were plotted in Figures 4.15 and 4.16	68
4.18 The heat flux through the surface of a droplet during freezing ($r/R=1$)	68
4.19 The temperature distribution inside a droplet ($\theta=60.8^\circ$)	70
4.20 The temperature distribution at the symmetric plane of a droplet during freezing ($\theta=90^\circ$)	70
4.21 The positions inside a droplet at which the temperature distributions were plotted in Figures 4.19 and 4.20	71

LIST OF FIGURES (CONTINUED)

FIGURE	Page
4.22 The heat flux through the base of a droplet during freezing ($\theta=0^\circ$).....	71
4.23 The temperature history of a node point of a droplet during freezing ($\theta=15.8^\circ$).....	73
4.24 The angular temperature distribution inside a droplet during freezing ($h \rightarrow \infty$) ..	73
4.25 The radial temperature distribution ($h \rightarrow \infty$)	74
4.26 The heat flux through the base of a droplet during freezing ($h \rightarrow \infty$)	74
4.27 Three regions during freezing of a droplet sitting on a cold plate ($R=1.4$ mm, $T_\infty=280.4$ K, $T_w=263.7$ K, $Re=137.6$, $h=77.8$ W/m ² ·K, $t=1.656$ s).....	76
4.28 Three regions during freezing of a droplet sitting on a cold plate ($R=1.4$ mm, $T_\infty=280.4$ K, $T_w=263.7$ K, $Re=137.6$, $h=77.8$ W/m ² ·K, $t=3.32$ s).....	76
4.29 Three regions during freezing of a droplet sitting on a cold plate ($R=1.4$ mm, $T_\infty=280.4$ K, $T_w=263.7$ K, $Re=137.6$, $h=77.8$ W/m ² ·K, $t=6.656$ s).....	77
4.30 Three regions during freezing of a droplet sitting on a cold plate ($R=1.4$ mm, $T_\infty=280.4$ K, $T_w=263.7$ K, $Re=137.6$, $h=77.8$ W/m ² ·K, $t=9.984$ s).....	77
4.31 Three regions during freezing of a droplet sitting on a cold plate ($R=1.4$ mm, $T_\infty=280.4$ K, $T_w=263.7$ K, $Re=137.6$, $h \rightarrow \infty$, $t=1.656$ s).....	78
4.32 Three regions during freezing of a droplet sitting on a cold plate ($R=1.4$ mm, $T_\infty=280.4$ K, $T_w=263.7$ K, $Re=137.6$, $h \rightarrow \infty$, $t=3.32$ s).....	78
4.33 Three regions during freezing of a droplet sitting on a cold plate ($R=1.4$ mm, $T_\infty=280.4$ K, $T_w=263.7$ K, $Re=137.6$, $h \rightarrow \infty$, $t=6.656$ s).....	79
4.34 Three regions during freezing of a droplet sitting on a cold plate ($R=1.4$ mm, $T_\infty=280.4$ K, $T_w=263.7$ K, $Re=137.6$, $h \rightarrow \infty$, $t=9.984$ s).....	79
4.35 Three regions during freezing of a droplet sitting on a cold plate ($R=1.4$ mm, $T_\infty=280.4$ K, $T_w=263.7$ K, $Re=137.6$, $h \rightarrow \infty$, $t=20.0$ s).....	80

LIST OF FIGURES (CONTINUED)

FIGURE	Page
4.36 Three positions for the calculations of the freezing front	82
4.37 The freezing front velocities at three positions shown in Figure 4.36	82
4.38 The predicted freezing time for a droplet sitting on a cold plate.....	84
4.39 Transient temperature distributions in the radial direction predicted by the mathematical model for grid sizes.....	84
4.40 The sensitivity test of the mathematical model to time step.....	86
4.41 Comparison of present numerical results and Neumann's exact solution for Stefan problem.....	86
4.42 A hollow sphere with isothermal surface conditions	89
4.43 The comparison of analytical solution and model results.....	89
4.44 Central temperature history: Comparison between model results and exact solution	90
4.45 Comparison of present numerical results with Neilson's simulation and experimental data.....	90
5.1 The schematic of experimental setup.....	96
5.2 The sketch of the test channel	98
5.3 A cross-section of the test cell	98
5.4 Schematic diagram of experimental setup.....	100
6.1 Effect of Am on freezing time for hemispherical droplets	112
6.2 Effect of flow field on freezing time for hemispherical droplets	112
6.3 Effect of heat transfer on freezing time for hemispherical droplets.....	113

LIST OF FIGURES (CONTINUED)

FIGURE	Page
6.4 The comparison of correlation predictions and experimental data	113
6.5 Experiment for measuring the average air-side convection coefficient \bar{h}	118
6.6 The equivalent circuit for Figure 6.5	118
6.7 Effect of Am on convective heat transfer	120
6.8 Effect of Re on convective heat transfer.....	120
6.9 Effect of Am on average convective coefficient.....	122
6.10 The comparison of correlation predictions and experimental data	122
6.11 Sketch of flat plate flow with an unheated starting length.....	124
6.12 Freezing front acquired by the camera at (a) $t=0.12$ s, $f_s=0.14$, (b) $t=0.3$ s, $f_s=0.28$, (c) $t=0.75$ s, $f_s=0.52$, (d) $t=1.62$ s, $f_s=0.8$, ($R=0.9$ mm, $T_w = 263.3$ K, $T_\infty = 280.2$ K, $Re = 89.65$)	125
6.13 The locations of freezing front at different time.....	126
6.14 The measured freezing front velocity during freezing	126
6.15 The schematic of inserting a thermocouple into a droplet with a micromanipulator	128
6.16 Micro-thermocouple placed in a 2.3 mm diameter water droplet	128
6.17 The position and the traverse line of a thermocouple in a droplet.....	130
6.18 The temperature distribution along a traverse line ($R=0.83$ mm).....	130
6.19 The temperature distribution along a traverse line ($R=1.32$ mm).....	131
6.20 The temperature distribution along a traverse line ($R=1.02$ mm).....	131

LIST OF FIGURES (CONTINUED)

FIGURE	Page
6.21 The temperature distribution along the traverse line in Figure 5.14 ($R=1.4$ mm)	132
6.22 The temperature history at a point within a droplet	132
6.23 The cooling curve at nodal element ($r=0.77$ mm, $\theta=36^\circ$).....	133
7.1 Temperature distribution along a vertical line: Comparison between model and experiment ($R=0.83$ mm).....	136
7.2 Temperature distribution along a vertical line: Comparison between model and experiment ($R=1.32$ mm).....	136
7.3 Temperature distribution along a vertical line: Comparison between model and experiment ($R=1.02$ mm).....	137
7.4 The temperature history: Comparison of model and experiment ($r=0.39$ mm, $\theta=81.2^\circ$)	137
7.5 The temperature history: Comparison of model and experiment ($r=0.33$ mm, $\theta=79.4^\circ$)	140
7.6 The velocity of the freezing front: Comparison of the numerical predictions and the experimental results	140
7.7 The velocity of the freezing front: Comparison of the numerical predictions and the experimental results	143
7.8 Freezing front position measured with the image acquisition system at $t=0.12$ s ($R=0.9$ mm, $T_w = 263.3$ K, $T_\infty = 280.2$ K, $Re = 89.65$).....	144
7.9 Freezing front position predicted with the mathematical model at $t=0.12$ s ($R=0.9$ mm, $T_w = 263.3$ K, $T_\infty = 280.2$ K, $Re = 89.65$).....	144
7.10 Freezing front position measured with the image acquisition system at $t=0.3$ s ($R=0.9$ mm, $T_w = 263.3$ K, $T_\infty = 280.2$ K, $Re = 89.65$).....	145

LIST OF FIGURES (CONTINUED)

FIGURE	Page
7.11 Freezing front position predicted with the mathematical model at $t=0.3$ s ($R=0.9$ mm, $T_w = 263.3$ K, $T_\infty = 280.2$ K, $Re = 89.65$).....	145
7.12 Freezing front position measured with the image acquisition system at $t=0.75$ s ($R=0.9$ mm, $T_w = 263.3$ K, $T_\infty = 280.2$ K, $Re = 89.65$).....	146
7.13 Freezing front position predicted with the mathematical model at $t=0.75$ s ($R=0.9$ mm, $T_w = 263.3$ K, $T_\infty = 280.2$ K, $Re = 89.65$).....	146
7.14 Freezing front position measured with the image acquisition system at $t=1.62$ s ($R=0.9$ mm, $T_w = 263.3$ K, $T_\infty = 280.2$ K, $Re = 89.65$).....	147
7.15 Freezing front position predicted with the mathematical model at $t=1.62$ s ($R=0.9$ mm, $T_w = 263.3$ K, $T_\infty = 280.2$ K, $Re = 89.65$).....	147
7.16 The area fraction of solid: Comparison of the experimental and numerical results.....	149
7.17 The freezing time: Comparison of the experimental and numerical results.....	149

LIST OF TABLES

TABLE	Page
A.1 Experimental results for freezing of hemispherical water droplets.....	166
A.2 Experimental results for heat transfer from a horizontal plate covered with water droplets.....	168

LIST OF IMAGES

IMAGE	Page
5.1 The experimental setup	95

CHAPTER I

INTRODUCTION

When the outdoor heat exchanger (evaporator) surface of a heat pump operating in the heat mode is cooled below 0°C, the moisture from the surrounding air condenses onto the surface and then freezes to form frost. The accumulation of frost blocks the air flow area and insulates the evaporator surfaces from heat transfer with the surrounding air (Kondepudi, 1988). As a result, the performance of a heat pump can decrease appreciably. Defrosting is periodically accomplished by reversing the refrigeration cycle to pump hot gas through the outdoor coil or using the strip resistance heaters to heat the outdoor coil surfaces. Because energy is needed to conduct the defrosting operation, the efficiency of a heat pump is reduced.

There have been a number of studies (Kondepudi, 1988, O'Neal, 1982, Stoecker, 1960) that have considered the frost properties and the effect of the frost layer on heat exchanger performance. A few researchers have investigated the frost structure and formation mechanism from a microscopic point of view. A common misconception of frost formation is that during the initiation of frost formation, frost is deposited directly from moist air onto a cold surface (Hayashi, 1977). This mode only occurs at cryogenic temperatures and not at conditions found in normal cooling, refrigeration or heat pump (heating) systems (Brian and Reid, 1969). At the thermal and air flow conditions

Journal model is the *ASME Journal of Heat Transfer*.

commonly occurring in these systems, frost formation exhibits several stages of growth (Tao and Besant, 1993). Gong, Bryant, and O'Neal (1995) proposed a five-stage model for the frost formation on a typical fin of uniform cross section, as shown in Figure 1.1. When the surface temperature of a heat exchanger is below the dew point of the surrounding air, water vapor condenses from the ambient air stream onto the cold surface. The condensate initially forms many tiny droplets (stage I). Then, the droplets grows through continued direct condensation and by coalescing with neighboring droplets (stage II). As time progresses, the droplets supercool to a temperature that is favorable for the formation of ice embryos. When this occurs, the droplets undergo a rapid phase change (stage III) from supercooled liquid to the solid phase (ice). The crystals then begin to branch out from these ice droplets (stage IV) and ultimately form a dense matrix (called "frost", stage V) that impedes air flow and thus deteriorates heat exchanger performance (Cremers and Mehra, 1980, Brian and Reid, 1970).

By examining the aforementioned stages, the frost formation process includes both the liquid and solid phases of water. Because the thermophysical properties change significantly from liquid water to porous frost, the frost formation process is influenced by time and by the history of frost layer. There is a need to conduct research on the initial stages of frost formation so as to bridge gaps in our knowledge of frost layer growth as it makes the transformation from the liquid to solid phase.

This study focused on quantifying the effect of plate surface temperature, air flow, and droplet size on the rate of freezing and heat transfer during the freezing of

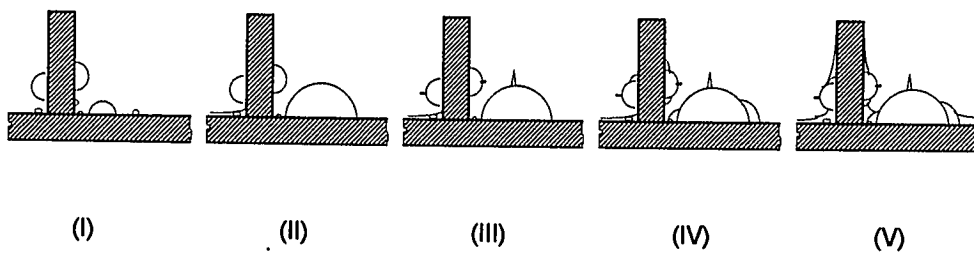


Figure 1.1 The frost formation on a typical fin of uniform cross section.

water droplets on a cold metal surface. The phase transition process was mathematically modeled and experimentally investigated.

The experimental portion of this study quantified the temperature field for a single droplet and the average air-side convection coefficient for a surface covered with many droplets. A digital imaging system was employed to visualize the progress of the freezing front and to record a complete freezing process of a hemispherical droplet on a videotape.

The experimental investigation included two parts. First, the conventional data acquisition system was used to perform the flow parameter measurements, such as temperature, heat flux, velocity, etc.. Because of the limitation of the instrumentation, the air-side convection coefficient at the individual droplet surface was not measured, while an existing correlation (Whitaker, 1972) was used to approximate the local air-side convection coefficient for the energy equations. The experimental data in this part were mainly used to verify the mathematical model predictions.

Second, a stereo microscope was used to view the microscopic stages of the freezing process of a hemispherical droplet. The images from the microscope system were either recorded on videotape or acquired by a digital image capture board installed in a micro-computer. These images were then analyzed with measurement imaging software for droplet size, micro-thermocouple placement, freezing front position, and freezing time.

The analytical investigation included the development of the mathematical model to simulate the two-dimensional transient phase change (freezing) process for a single condensate droplet during frost formation on a cold surface. The numerical formulation was based on the control-volume finite-difference method (Patankar, 1980) with non-moving mesh technique. The advantage of this technique was that once a mesh had been established it was not changed even though the phase-change region moved through the mesh.

In the mathematical model, the heat transfer mode in the droplet was assumed to be conduction only with a forced convection boundary condition at the surface. The thermal properties of each phase were assumed to be constant and the phase change took place at one temperature level. A spherical coordinate system was used for the droplet, and the problem then became symmetrical about the central plane. The mathematical model was adaptable to different geometries and allowed a variety of boundary conditions.

1.1 Contribution of This Study

A finite-difference mathematical model was developed to solve the two-dimensional freezing of hemispherical droplets in spherical coordinates. Results were obtained for the transient temperature distributions at three phase regions, the heat transfer rates through boundaries, solid fraction, and the transient freezing front position could also be calculated. Some generalized principles (Patankar, 1980) were introduced

in the development of the mathematical model to ensure that the mathematical model could be adapted to other geometries and boundary conditions.

In the process of the detailed analysis of temperature distribution within a droplet, it was found that the lowest temperature always happened around the perimeter of a droplet. The crystal growth (stage IV shown in Figure 1.1) should started to grow at the perimeter area of a droplet, tending to form an ice sublayer on the cold metal surface. A computer program was developed to graphically simulate the progress of the phase-change region in a hemispherical droplet during freezing.

In the experimental study, a new dimensionless number and some combinations of classical dimensionless numbers were introduced for the freezing of hemispherical droplets on a cold horizontal surface. Two correlations, one for dimensionless freezing time and another for interfacial convection coefficient at the water droplet surface, were developed from experimental data.

The temperature distributions were measured at several locations along a vertical line within a droplet. The transient temperature history at a location (from the liquid phase to the solid phase) within a droplet was also measured. The locations of thermocouple junctions were measured by imaging process software.

The freezing time, the solid fraction, and the velocity of the phase-change region were obtained by measuring the digitized images.

1.2 Scope of Investigation

In this investigation the freezing of a hemispherical droplet was mathematically modeled and experimentally investigated. Chapter II contained a comprehensive literature survey on the mechanism of frost formation, temperature field of a hemispherical droplet, heat transfer through the boundaries of a hemispherical droplet, freezing front velocity, freezing time, and mathematical approaches on freezing problems. More of the discussions were focused on the single droplet analysis because this was of primary concern in the present study.

The development of the mathematical model was detailed in Chapter III. It included the mathematical description of the problem, the discretization of the partial differential equations and boundary conditions, the solutions of the discretized equations, the systematic assessment of the numerical errors. Some typical model predictions were presented and discussed in Chapter IV.

An experimental setup was described in Chapter V. Schematic diagrams and images of the test setup and descriptions of the individual components which comprised the test loop and instruments were included.

Detailed experimental results and data reduction were presented in Chapter VI. A new dimensionless numbers were introduced for the study of the freezing problems. Plots of relevant experimental data, such as freezing time, the average air-side convection coefficient, transient locations of the freezing front, and temperature profiles, both in dimensional and non-dimensional form, were presented in the form of graphs.

Two empirical correlations for freezing time and the average air-side convection coefficient were developed.

In Chapter VII, the model predictions obtained by the proposed model of freezing time, transient locations of the freezing front, and the temperature field of a hemispherical droplet were compared to relevant experimental data, results reported by previous investigators and available analytical solutions.

Some important conclusions from this investigation were presented in Chapter VIII. The contribution of this study was also presented and discussed with respect to the present status of the problem. Some recommendations for the future work were also presented.

CHAPTER II

LITERATURE REVIEW

Correlations have been developed by a number of investigations for the average properties of frost and the overall effect of the frost layer on heat exchanger performance (O'Neal and Tree, 1985, Saito and Tokura, 1991). Some researchers have investigated the very early stages of the condensation and frosting phenomena. Hayashi and Aoki (1977) indicated that during the first stage of frost growth, frost was deposited directly onto the cold surface. This mode only occurs at cryogenic temperatures and not at conditions found in normal cooling, refrigeration or heat pump (heating) systems. At the thermal and air flow conditions commonly occurring in these systems, the frost growth process begins with the condensation of water from moist air onto the cold surface. For the case of dropwise condensation, the condensate forms many droplets. These droplets grows by continued direct condensation and by coalescence with the neighboring droplets. When the surface temperature is much below the freezing temperature of water, these droplets would freeze to ice, which is an important phase-change stage in the early frost formation process.

The available literature was divided into five main categories:

- Frost formation — General information was presented on the history of research on frost formation. It allowed the investigators to focus on some less studied areas of frost formation.

- **Temperature field** — This was the basic starting point for every heat transfer investigation and it acted as a base on which the investigators could obtain heat transfer rates and simulate the freezing process.
- **Phase-change region position** — This was of particular importance to phase change problems. The phase-change region, or the phase-change front, was a special zone with its own properties and was always at the freezing temperature. The shape of the phase-change region evolved with time and was an important criterion for investigators to check the reasonability of model predictions.
- **Air-side convection coefficient** — It was of importance to the engineers in the design of heat transfer equipment. The available information on this area was very limited.
- **Mathematical methods on freezing problems** — Most of the algorithms that had been proposed to solve phase-change problems were limited to the simple geometries such as half infinite space, rectangular container (Lemmon,1981, Crank, 1981). There was a need to develop a mathematical model for the freezing of a hemispherical droplet.

2.1 Frost Formation

As frost forms on a cold surface, the microscopic crystal structure varies significantly for different air velocities, air moisture content, surface temperatures, and surface finishes. If the wall temperature is very low, such as the cryogenic condition, the

frost will directly form on the cold surface (Brian, Reid, and Brazinsky, 1969). At conditions found in normal heating, cooling, and refrigeration systems, the properties of the frost layer is heavily dependent on the freezing of liquid condensate on the wall surface. However, these properties can change by an order of magnitude (O'Neal and Tree, 1985).

The average properties of frost were needed as input into the governing equations for the frost heat and mass transfer study. Some empirical correlations for average thermal conductivity and density were developed by previous investigators (Sanders, 1974, Yonko and Sepsy, 1967, Marinyuk, 1980). Because a correlation could not take all the possible variables into account, there was a wide spread in the properties predicted by the proposed correlations. Hayashi et al. (1977) defined a three-stage frost formation, i.e., crystal growth, frost layer, and frost layer full growth. They obtained an empirical correlation of the frost density with the cold surface temperature. Tao, Besant, and Rezkallah (1992) proposed a two-stage model, in which frost growth on a flat plate was divided into two periods: (1) a crystal growth period, and (2) a fully developed frost layer growth period. In the early stage of frost formation, many ice columns were hypothesized to grow at the surface where liquid nucleation occurred. Each ice column was postulated as a growing circular fin on a constant temperature base. The diameter of a circular fin changed with increasing time caused by continued direct condensation. It was assumed that the air-side convection coefficient at the ice column surface was the same value as that at the cold plate. The one dimensional, transient temperature field and the growing rate of an ice column were obtained by solving pure conduction

governing equations. In the fully developed frost growth period, the frost layer was modeled as a homogeneous porous medium. The governing equations for porous material were solved to get the transient temperature distribution in the frost layer. All the properties of frost were defined with average values with porosity as a parametric variable.

Tao et al. concentrated mainly on the fully developed frost growth period. There was no obvious linkage of the temperature distribution and frost growth between the two periods. The study of frost formation focused on a calculation of the temperature distribution in a porous material. However, this study presented a frost growth model that divided the frost formation process into several stages and introduced some microscopic points of view to the study of frost formation.

Mao, Besant, and Rezkallah (1993) performed some frost experiments with airflow over a flat plate. Several correlations for frost height, average density, apparent thermal conductivity, apparent Nusselt number were presented. The independent variables were distance from leading edge, humidity ratio, temperature, Reynolds number, and Fourier number. Ranges of test conditions were: wall temperature, from -5 to -15°C, air temperature, from 15 to 23°C, air velocity, from 1.15 to 2.67 m/s, and air humidity ratio, from 0.004 to 0.01. It was not clear from this paper whether the average frost properties predicted from these correlations could be extrapolated satisfactorily.

One noticeable experimental study that dealt with the early stage of frost formation was Tao, Besant, and Mao (1993). The frost growth process was classified into two stages: subcooled water and ice column growth. A microscope of 100×

magnification mounted above the test section was used to observe and photograph the frost formation process. They observed that the average radius of condensate droplets depended on the wall temperature.

There were two important things that were not clear in this paper. First, the transition time between periods was not measured because the subcooling temperature of water was a random value. Second, the camera fixed at the top of the test section could not get the side-view photographs. The images presented in the paper were not good enough to show that frost formation began from the top of a droplet. In fact, the model results conducted by Gong, Bryant, and O'Neal (1995) showed that the heat transfer around the perimeter area of a droplet was much higher than that at the top of a droplet. Ice crystals was observed to grow at the perimeter area of a condensate droplet and had a tendency to form a solid glaze of ice on a heat exchanger surface. The ice would act to insulate the wall surface from heat transfer with ambient air.

Kondepudi (1988) studied the frost formation on heat exchanger surfaces. In his frost growth model, one of the assumptions was that part of the water vapor, which converted to frost, went to increase the frost density and the rest to increase the frost height. It was difficult to get the percentages at which the condensate broke up into the density and the growth components. If 50% of the mass was assumed for each part, the frost height from the model predictions would be higher than that of the experimental results, and the frost density predicted by the model was smaller than that obtained by the experiments. Kondepudi also studied frost formation on finned heat exchangers with different fin types such as louvered, flat plate, wavy, corrugated and spine fins. He

concluded that the louvered fin had the maximum frost accumulation under similar conditions when compared to the other fins; The flat fin type had the lowest frost growth. The geometry of the heat exchanger surface could influence the departure diameter of the condensate droplet. The complex geometry made it possible for condensate droplets to spread and to coalesce into a thin film, while only small droplets could stay at a flat fin surface. The drainage of condensate became more important as soon as the condensation happened on a heat exchanger surface.

Knowledge about the frost growth is indispensable for understanding the mechanism of the frost formation. Schneider (1978) developed a correlation for frost growth that was independent of Reynolds number. The frost height was approximately 0.47 power dependence on time. O'Neal (1982) reported a correlation for frost growth within a parallel plate geometry, in which the frost height was dependent on Reynolds number.

In summary, the aforementioned investigations correlated the average properties and growth of frost with some heat transfer and flow variables. For this reason, there was not a similarity relation among these empirical correlations. Detailed observation of frost formation indicated that it would be inaccurate to use one empirical correlation to obtain the average properties over the entire frost formation process. To precisely correlate the average properties of frost, the entire process should be divided into several stages with the frost height as an indicator.

2.2 Temperature Field

The temperature field in condensate droplets resulting from conditions imposed on its boundaries is indispensable for calculating the transient heat flux and the phase change at any point in a condensate droplet or on its surface.

There were different types of mathematical models used to calculate the temperature field during phase-change process. Some of them were based on the premise that there was internal circulation which might be caused either by buoyancy force or surface tension force. Sparrow (1981) performed experiments to study the freezing of a liquid on a cooled surface. The objective was to provide fundamental information about the roles of solid-phase conduction and liquid-phase natural convection in freezing. If the liquid was isothermal at its freezing temperature, natural convection did not occur. This mode of freezing might be termed conduction-controlled freezing. When the temperature of a liquid was above the freezing value, there would be temperature nonuniformities through the liquid, and natural convection would generally occur. Experimental evidence supporting this internal circulation emerged from several investigators (Bathelt and Viskanta, 1979). Sparrow (1979) demonstrated that the presence of natural convection could change the temperature field, slow down the freezing process, and ultimately terminate freezing. The stronger the natural convection, the thinner the frozen layer. Flemings (1974) studied the effect of convection on the crystal growth of a liquid metal. He found that convection became important only when

a metal size was big enough. Put another way, a metal droplet could be considered a “lump” when its diameter D was smaller than a critical value, $0.1k/h$.

Trefethen (1958) suggested that the temperature distribution in a large drop could be affected if there was a significant internal circulation. With a simple model he predicted an increase of heat transfer 170 times higher than that predicted by the conduction solution alone. No experiments substantiated his claim.

Some investigators postulated that the contribution of natural convection to the temperature distribution was insignificant. Lorenz (1970) considered a hemispherical water drop on a flat isothermal surface. He assumed that the drop growth was quasi-steady. Because the heat capacity of the growing drop was small compared to the heat flux through the drop, the transient effects were negligible on the temperature distribution. He tried to determine the effects of thermocapillary flow on heat transfer in dropwise condensation by simultaneously solving the momentum and energy equations with an appropriate set of boundary conditions. A complete solution to the problem that predicted the actual heat transfer rates through each drop was not attempted. Instead, the solution presented was primarily concerned with showing the percentage increase in heat transfer over the conduction solution.

By introducing the stream function, he handled the non-linear and coupling between velocity and temperature in governing equations and boundary conditions by iteratively solving linearized finite-difference equations. He plotted the stream function and steady-state temperature distribution inside the drop. The maximum value of surface velocity increased with Bi for $Bi < 50$ and decreased for $Bi > 50$. The position of the

maximum velocity moved to the perimeter with increasing Bi , indicating that most of the temperature variations at the surface was concentrated near the corner for higher Bi . In other words, the internal circulation increased the temperature gradient near the perimeter. He concluded that the thermocapillary flow did not contribute significantly in the dropwise condensation of water. The increase in heat transfer was not higher than a few percentage over the one predicted by neglecting internal circulation.

Hurst in his Ph.D. Dissertation (1966) explained the reason why the primary mechanism of heat transfer within the droplet resting on a cold plate was pure conduction. For an upward facing condensing surface, the condensate in the droplet would be arranged with the hotter liquid on top and the cooler liquid below. Thus, the density changes in the liquid would act to oppose, rather than encourage, natural circulation. Furthermore, some simple experiments were run with very fine titanium dioxide particles were sprinkled onto the condensing surface so that they were picked up by the growing condensate droplets. The motion of the titanium dioxide particles within the droplets showed that, at least within nearly hemispherical droplets, circulation existed in noticeable magnitude only during coalescence of droplets, and died out very quickly afterwards.

Hurst (1973) performed an experiment to measure the steady-state temperature distribution inside the drop. In his test rig, the dropwise condensation occurred on the upper side of a 0.001-in-thick horizontal copper condensing surface. The lower side of the condensing wall was convectively cooled, and the cooled-side temperatures under growing droplets were measured using infrared-radiation technique. He only measured 2

to 3 points for each droplet and concluded that the surface temperature increased as the edge of the droplet was approached from the inner part of the droplet. The graphs in his paper could roughly verify that his conclusions were correct.

Hurst also developed a finite-element scheme to analyze the drop and condensing surface with the assumption that heat transfer through droplet was driven primarily by conduction. The part of the condensing surface that was in contact with the condensing vapor, but which was outside the area covered by the droplet, was considered to be adiabatic. Grid generation consisted of two parts: one was in cylindrical coordinates for the droplet and the other was in rectangular coordinates for the copper condensing wall. He studied a single droplet from a number of similar droplets resting on the surface. An equivalent interfacial "film" coefficient was defined to calculate the coupled heat and mass transfer rates from the saturated vapor to the condensate surface as functions of the temperature difference between the vapor and the droplet. Several graphs qualitatively showed the steady-state isotherms. He concluded that the thickness of the copper condensing wall affected the temperature distribution significantly. The mean temperature under a small droplet was higher than the mean temperature under a large droplet. He believed that a steady-state-temperature solution assuming an isothermal droplet base was reasonable for most practical applications.

Boger and Westwater (1967) conducted measurements of transient and steady-state temperature profiles during the freezing and melting of water. They concluded that

the Rayleigh number was very important. If the Rayleigh number was sufficiently large, the internal circulation affected temperature field significantly. The onset of natural convection was at a Rayleigh number of about 1700.

Hale (1980) performed experiments in several different materials and concluded that natural convection was very important to temperature field for unstable situations that arisen during freezing from above.

When a gas stream flows over a droplet surface, the viscous effects produce a circulation in the droplet, which causes forced convection inside the droplet. Chiang, Raju, and Sirignano (1992) examined a cold fuel droplet that was suddenly injected into a hot gas stream in a combustion device. The fuel droplet vaporized in the convective gas stream to form the air-fuel mixture. This paper presented the effects of variable thermophysical properties, transient heating and internal circulation of liquid, deceleration of the flow caused by the drag of the droplet, boundary layer blowing, and moving phase-change region on temperature field and velocity profile. The heat transfer mechanism within the droplet was initially dominated by conduction. When the internal flow gained strength, the main heat transfer switched to convection. Finally, the reduction of the surface shear stress caused the internal circulation to decrease, with conduction again becoming the dominant mechanism.

Prakash and Sirignano (1978) analyzed a liquid droplet moving through a gas for a burning air-fuel spray mixture in a typical combustor. The internal circulation was a axisymmetric quasi-steady liquid motion with a spherical core vortex surrounding by a viscous boundary layer and an internal wake. The vortex strength was determined as a

function of the shear stress along the droplet surface. The internal circulation affected the heat conduction in the liquid core.

2.3 The Phase-Change Region Position

The freezing of condensate droplets on a cold plate is an important phase-change stage early in the frost formation process. The essential features of systems undergoing liquid-to-solid phase-change heat transfer are that a phase-change region separates the two phases of different thermophysical properties and is a location where energy is liberated. Phase transition usually occurs at a fixed temperature or over a limited temperature interval when a foreign substance is presented. For this reason, phase change problems are referred to as moving boundary problems (phase-change region was an isothermal or quasi-isothermal boundary between liquid and solid).

To solve the phase-change problem, it is necessary to determine the rate at which the phase change front evolved with time. Neumann (1916) developed the most important exact solution for the Stefan problem, the freezing of a semi-infinite region above a metal plate. The liquid filled half-space region and the metal plate were initially at a constant temperature which was greater than the freezing temperature. The temperature of the plate was suddenly lowered to a value much below the freezing temperature of the liquid. The liquid began to cool and after a period of supercooling the liquid would nucleate to solid. In Neumann's model, the density of the solid was the same as that of the liquid, but the other physical properties of the two phases were

assumed to be different and to be constant. A dimensionless number, the Stefan number, was used to help qualifying the phase-change process:

$$\text{Ste} = \frac{C_s(T_\infty - T_w)}{h_f} \quad (2.1)$$

If Ste was small, the phase-change region position predicted by the model would have a power dependence of 0.5 with time. An experimental study for the phase-change region position of the solidification of n-octadecane in a rectangular test cell was performed by Hale and Viskanta (1980). Good agreement was obtained between experimental data and Neumann's analytical predictions, which verified Neumann's model for a small Stefan number.

A microscopic study of solid-liquid phase-change region during freezing was conducted by Thomas and Westwater (1963). The test material was contained in a square tube designed to maintain a unidirectional heat flux. A 16-mm camera was attached to a 6X objective lens in the microscope. All measurements from the motion picture films were taken on a motion analyzer. In the freezing front velocity versus time curves the experimental line reached immediately to a maximum value after solid nucleation and then decreased gradually. The experimental values for the velocity of the freezing front during freezing were compared with those predicted by Murray-Landis mathematical model (1959). The comparison of the results showed that the measured values were as much as 100% higher than those predicted mathematically. Thomas and Westwater observed that the phase-change region was constantly changing shape during

freezing, which resulted in average freezing front velocity variations from 60 to 200% at individual point.

Solidification heat transfer from a vertical side wall has been studied. Gau and Viskanta (1986) measured the positions of the phase-change boundary for melting and solidification taking place in a rectangular test cell heated or cooled from one of the vertical walls. The buoyancy-induced convection affected the phase-change region position during melting and made the phase-change region morphology irregular during solidification.

A computational study of solidification of a binary Na_2CO_3 solution in a horizontal cylindrical annulus with a control-volume based, finite-difference scheme was performed by Neilson and Incropera (1990). The numerical simulation took 15 hours of supercomputer CPU time to solve the governing equations. The agreement between the model predictions for the solid thickness as a function of angular position and experimental results had significant differences. Neilson and Incropera concluded that the discrepancy was attributed to the model's inability to resolve the true nature of the solutally driven plume, to uncertainties in the material property data base and to model assumptions such as validity of the Kozeny-Carmen equation.

2.4 The Air-Side Convection Coefficient

For a condensing surface covered with condensate droplets, various investigations have developed different definitions of the air-side convection coefficient.

As shown in Figure 2.1, let \bar{h} stand for the average air-side convection coefficient for the entire surface, and h_1 , h_2 stand for the local convection coefficients at the bottom and the surface of the droplet, respectively.

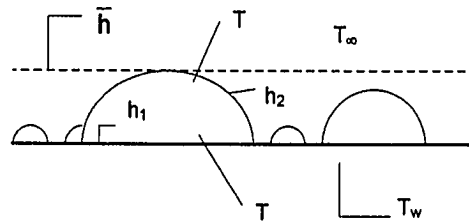


Figure 2.1 The average and local convection coefficient.

A large number of studies focused on the average air-side convection coefficient of the condensing surface. Tanasawa (1978) noted considerable discrepancies existed among the experimental data. A number of factors influenced the air-side convection coefficient of dropwise condensation. Tanasawa listed those factors as following: (1) moist air velocity above the cold plate, (2) coatings or promoters on the cold surface, (3) finishes of the cold surface, (4) non-condensable gases, (5) surface supercooling, and (6) experimental technique and instruments or method.

From the definition of the air-side convection coefficient, the most important variables should be temperature difference and heat flux. The temperature of a condensing surface varies significantly with time and location because of the random distribution of condensate. For dropwise condensation, it is very difficult to control this

surface temperature at a uniform value. It leads to the uncertainty in the measurement of the air-side convection coefficient.

Two techniques have evolved for measuring surface heat flux: thin-film surface thermometry and thick-film calorimetry (Scott, 1976). The first method recorded instantaneous surface temperature from which instantaneous heat flux rates were deduced using classical heat conduction theory. In the second method, the gauge absorbed the total heat input to the surface, and the instantaneous heat flux rate was determined to be the time rate of change of temperature of the gauge.

Silver and Simpson (1961) considered equilibrium interactions between the molecules leaving the surface and those approaching the surface. They derived an equation to calculate the local convective coefficient:

$$h_i = \left[\frac{2\hat{\sigma}}{2 - \hat{\sigma}} \right] \left(\frac{h_{iv}^2}{T_v \nu_{iv}} \right) \left(\frac{\bar{M}}{2\pi \bar{R} T_v} \right)^{1/2} \left(1 - \frac{P_v \nu_{iv}}{2h_{iv}} \right) \quad (2.2)$$

The h_i value depended on the condensation accommodation coefficient. The definition of this coefficient was the ratio of the vapor molecules that would not be reflected but be captured by the liquid phase to the total number of vapor molecules that hit the liquid surface. The reported values ranged from 0.04 to 0.2.

The above analysis assumed that the fluxes of condensing and vaporizing molecules could be derived from kinetic theory for each flux direction separately and the results superimposed to obtain the net flux.

Umer and Griffith (1965) used Eq.(2.2) to obtain the local air-side convection coefficient in the analytical solution for growth of hemispherical droplets during condensation. Transfer of sensible heat from the vapor to the droplet was assumed negligible compared to the transport of latent heat as a result of condensation.

The air-side convection coefficient predicted by Eq.(2.2) reaches a magnitude of $10^5 \text{ W/m}^2\cdot\text{K}$. It is not suitable to the analysis of dropwise condensation found in normal cooling, refrigeration or heat pump systems. Vliet and Leppert (1961) considered a single sphere suspended in a channel through which a fluid was flowing. An empirical relation was recommended for calculate the average heat-transfer coefficient from a sphere to water in forced convection:

$$\overline{\text{Nu}} = (2.7 + 0.12\text{Re}^{0.66})\text{Pr}^{0.5} \left(\frac{\mu}{\mu_w}\right)^{0.25} \quad (2.3)$$

Whitaker (1972) divided the heat transfer from the sphere into two parallel processes. In the laminar boundary layer region the contribution to the Nusselt number should be of the form $\text{Re}^{1/2} \cdot \text{Pr}^{1/3}$, while in the wake region the contribution should be of the form $\text{Re}^{2/3} \cdot \text{Pr}^{1/3}$, so that Eq.(2.3) could be expressed as

$$\overline{\text{Nu}}_D = 2 + (0.4\text{Re}_D^{1/2} + 0.06\text{Re}_D^{2/3})\text{Pr}^{0.4} \left(\frac{\mu}{\mu_w}\right)^{1/4} \quad (2.4)$$

$$0.71 < \text{Pr} < 380$$

$$3.5 < \text{Re}_D < 7.6 \times 10^4 \quad (2.5)$$

$$1.0 < \left(\frac{\mu}{\mu_w}\right) < 3.2$$

The correlation was accurate to within $\pm 30\%$ for the range of parameter values listed. All properties except μ_w should be evaluated at T_∞ , while μ_w was evaluated at T_w .

For liquid metals, Witte (1968) suggested the following correlation:

$$\bar{Nu}_D = 2 + 0.386(Re_D Pr)^{1/2} \quad (2.6)$$

$$\begin{aligned} Pr &\leq 0.03 \\ 3.6 \times 10^4 &< Re_D < 1.5 \times 10^5 \end{aligned} \quad (2.7)$$

As an approximation, this correlation may also be used for flow past conventional liquid droplets. It was found that the predicted air-side convection coefficient could be within $\pm 20\%$ of the observed values.

In summary, the data relating air-side convection coefficient showed a wide variation in value. Knowledge of how the air-side convection coefficient changes during the freezing of a condensate droplet is critical because it influences the temperature field, and affects the freezing process.

2.5 Mathematical Methods on Freezing Problems

A literature review given by Crank (1981) summarized the state-of-the-art and extensive lists of references to previous and current work on freezing problems. Other surveys were given by Viskanta (Lane, 1983) and Samarskii (1993), all with useful bibliographies.

The first published discussion of this kind of problem was presented by Stefan in 1891 in a study of the thickness of polar ice. Because an phase-change region separating

two regions of different thermophysical properties existed and moved as a function of time, the problem was strongly nonlinear and there were a few exact solutions available. Neumann (1912) presented an exact solution of the initially half-space with the surface maintained at a lower than the freezing temperature, which was the most notable breakthrough. It has been a standard exact solution used to check approximate solutions of problems of this kind. In recent years, Neumann's solution was also frequently used to verify the mathematical methods to related problems.

Beyond those few exact solutions many mathematical methods and correlations have been developing in last twenty years. Goodman (1961) applied heat balance integral methods to the one-dimensional heat conduction problem with temperature-dependent thermal properties. He used a polynomial to represent the temperature profile for each phase and reduced a system of integral equations to a set of ordinary differential equations, which yielded the velocity of the moving boundary. The position of the nodes was changed at each time step to approximate the phase change boundary by a piecewise-linear curve. Unless the problem geometry is very simple, analytical solutions of these kinds are not available.

Baxter (1962) applied the enthalpy method to one-dimensional problems. The enthalpy was related to temperature and included the effects of both specific and latent heat. The enthalpy form of the conservation equation was equivalent to three differential equations: one in each of the two single phase regions and the third at the phase-change region. The problem was equivalent to a nonlinear conduction problem without phase change. Shamsundar (1975) verified that the enthalpy method could be used to a

multidimensional case. The enthalpy method assumed the densities of the solid and liquid phases were identical and uniform. The other thermodynamic properties may differ between the two phases and may also depend on temperature. This method circumvented successfully the moving phase-change region problems. Carnes-Pintaux (1986) proposed a finite element enthalpy method to solve problems in which the phase change occurred at a given temperature. He considered the enthalpy to be a function of an auxiliary variable and tried to avoid the problem of the temperature history of a point displaying a pronounced steplike behavior. Crowley (1978) extended the enthalpy method to multidimensional problems. He obtained the numerical solution for the freezing of a square cylinder when the surface temperature decreased at a constant rate. Enthalpy method can only be used in pure conduction problems and required that the phase-change process took place at the freezing temperature.

Ghosh (1993) tried to use an arbitrary Lagrangian-Eulerian kinematics description in the finite-element formulation to impart flexibility to the motion of the nodes. By detaching the nodes from the underlying material, nodes could be monitored to follow the evolving front to maintain shapes of the elements. Bushko (1991) introduced an exact specific heat method for finite element analysis of transient heat transfer with phase change. This method was originally suited for metals and alloys that exhibited discontinuous specific heat functions across the phase transition temperature. He used an exact representation of the specific heat function and exploited its mathematical properties in obtaining the latent heat matrix. Runnels (1993) introduced a domain-decomposition strategy for finite-element simulation of phase change. This

strategy exploited nonlinear subdomain iteration to improve the efficiency of the computation by taking advantage of the local nature of the latent effect. The principle idea was to identify the discrete values at each nonlinear iteration and to define a domain decomposition for the reduced linearized subsystem.

Special numerical techniques to smooth the deforming front and to avoid continuous remeshing have been introduced. Gupta (1987) constructed a short-time analytical solution for heat conduction problems in spherical geometry. Tao (1967) proposed a mathematical method and an analytical solution for a one-dimensional moving phase-change region problem of cylinders and spheres. His solution was based on steady state and could not be extended to the two-dimensional or initial-boundary problems. In recent years, Vick (1993) attempted to use the boundary element method to reduce the phase change problem to a nonlinear set of integral equations. These integral equations could be solved numerically using simple basis functions for the unknown boundary data, with no need to discretize the entire domain.

The control-volume methods are very powerful in dealing with heat transfer and computational fluid dynamics. Within the author's knowledge, no paper was found to apply this method to phase-change problems.

2.6 Summary

Several conclusions could be drawn from the above survey of the literature available.

- Frost formation process based on dropwise condensation can be classified into five periods: condensate nucleation, droplet growth, freezing, crystal growth, frost layer growth. Such a division of the frost formation process has not been done in the past. However, it seems to be effective in helping understand the complex nature of the frost growth process.
- The freezing of condensate droplets is an important phase-change process. A more comprehensive study on a single droplet might be helpful to understand the basic mechanism of frost formation.
- A large amount of work has been done to study the phase-change process in simple geometries. These geometries include rectangulars, semi-infinite slab, cylinders and annuli. The literature available on the freezing of spheres and hemispheres is limited.
- It should be desirable to be able to predict the temperature field and heat transfer for a water droplet during phase transition.
- A mathematical model based on the basic heat transfer equations is needed to simulate the phase-change process in different geometries. The adaptability of control-volume methods makes this kind of mathematical manipulation possible.
- More experimental work is needed to elaborate the early stages of frost formation and to supply validations to the mathematical model.
- Some generalized correlations among the varying test conditions, the measured data, the size of a droplet, and the thermophysical properties could be very useful for the phase-change studies.

- There is still a need for better data on the average and local air-side convection coefficients.
- Numerous attempts have been made to quantify the relationship between the frost thermal conductivity and density, but the data still show significant scatter.
- Further studies are recommended to supply important information to improve the heat exchanger designs, to develop new cooling devices based on phase-change, and to extend the freezing study to its inverse process, melting.

CHAPTER III

MATHEMATICAL MODEL DEVELOPMENT

Frost formation and growth on a cold heat exchanger surface was divided into several stages by Hayashi et al. (1977), Tao et al. (1992). Previous researchers have focused primarily on crystal growth stage in order to get the average properties and the average growth rate of a frost layer. Because the complicated nature of the frost structure, there was need to study and qualify the phase transition from liquid to solid for condensate droplets during the frost formation process. The present study was undertaken to provide fundamental information about the temperature field and heat transfer for a single condensate droplet during freezing. This chapter described the development of a mathematical model and its computational procedure. The next chapter presented some of the typical predicted numerical results of the model.

3.1 The Problem

Figure 3.1 shows a hemispherical water droplet resting on a flat horizontal surface. The droplet had an initial temperature higher than its freezing point and the ambient air with the same temperature flew over the droplet. At a certain time when the surface temperature suddenly dropped to a value much below the freezing point, the droplet began to cool and after a period of supercooling the liquid would nucleate to ice.

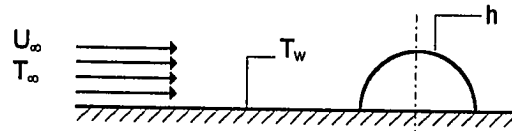


Figure 3.1. The schematic of the problem.

3.2 Assumptions

The hemispherical droplet (Figure 3.1) was assumed to be initially at a uniform temperature above the freezing temperature and was assumed to rest on a flat horizontal surface. Air at a constant temperature and moisture content flew in parallel over the surface. Any internal convective flows in the droplet associated with the effects of fluid shear on the droplet surface were neglected in the presented model. Additionally, internal convection due to temperature gradients in the droplet was neglected. Conduction was assumed to be the only mode of heat transfer. In Figure 3.1, heat conduction was axisymmetric to the center line of the droplet. It was also assumed that the temperature within a droplet did not change with the azimuth angle and the thermal properties of each phase were assumed to be constant.

3.3 Governing Equations and Discretization

Consider a connected, two-dimensional region Ω and its boundary Γ . Because of the symmetry, the computational domain may be simplified to a one-fourth section of the hemispherical droplet. A cross section of such a region is shown in Figure 3.2.

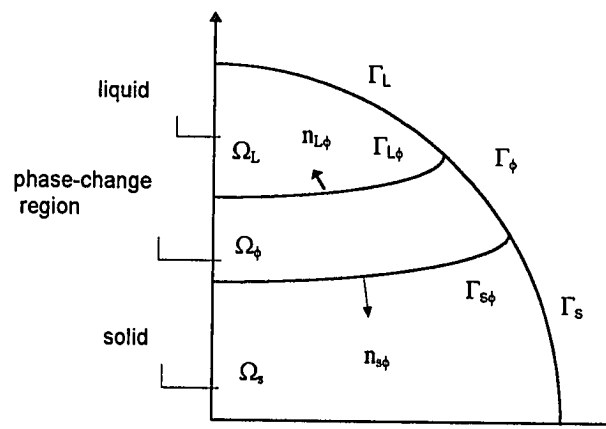


Figure 3.2. Cross section of one fourth of a two-dimensional spherical region containing a medium at two physical states.

Governing Equations

Let Ω initially contain a uniform phase (liquid), and a second phase (solid) form and progress into the region Ω . Let the regions and boundaries occupied by the liquid, solid, and phase change zones be Ω_L , Γ_L , Ω_S , Γ_S , and Ω_ϕ , Γ_ϕ respectively. The freezing temperature of water is commonly accepted as 0°C at standard atmospheric pressure. In

reality, water can be cooled well below the thermodynamic freezing point before it freezes (Fletcher, 1966). Water that has been cooled below the freezing point is subcooled and is metastable. The transformation from this subcooled metastable state to a stable thermodynamic saturated state occurs when the water nucleates to the solid phase at its freezing point. In this study, it was assumed that the freezing process occurred at the triple point of water so that the phase transition region would have a uniform temperature and the latent heat would be a constant value. The temperatures $T_L(r, \theta, t)$, $T_S(r, \theta, t)$, and $T_\phi(r, \theta, t)$ satisfied the following relations, respectively.

$$\nabla^2 T_L(r, \theta, t) = \frac{1}{\alpha_L} \frac{\partial T_L(r, \theta, t)}{\partial t} \quad t > 0, (r, \theta) \text{ in } \Omega_L \quad (3.1)$$

$$\nabla^2 T_S(r, \theta, t) = \frac{1}{\alpha_S} \frac{\partial T_S(r, \theta, t)}{\partial t} \quad t > 0, (r, \theta) \text{ in } \Omega_S \quad (3.2)$$

where

$$\nabla^2 T(r, \theta, t) = \frac{\partial^2 T}{\partial r^2} + \frac{2}{r} \frac{\partial T}{\partial r} + \frac{1}{r^2 \sin(\theta)} \frac{\partial}{\partial \theta} \left(\sin(\theta) \frac{\partial T}{\partial \theta} \right)$$

the boundary and initial conditions were given by

$$-k_L \frac{\partial T_L(r, \theta, t)}{\partial r} \Big|_{r=R} = h (T|_{r=R} - T_\infty) \quad t > 0, (r, \theta) \text{ on } \Gamma_L \quad (3.3)$$

$$-k_S \frac{\partial T_S(r, \theta, t)}{\partial r} \Big|_{r=R} = h (T|_{r=R} - T_\infty) \quad t > 0, (r, \theta) \text{ on } \Gamma_S \quad (3.4)$$

$$T(r, \theta, 0) = T_i \quad (r, \theta) \in \Omega \cup \Gamma \quad (3.5)$$

with the phase-change region conditions

$$T_L = T_S = T_\phi \quad (3.6)$$

$$k_s \frac{\partial T_s}{\partial n} = h_{sf} \rho_s \frac{\partial \varepsilon}{\partial t} + k_L \frac{\partial T_L}{\partial n} \quad t > 0, (r, \theta) \text{ on } \Omega_\phi \quad (3.7)$$

The above equations represented two initial boundary value problems related to each other by the nonlinear phase-change region conditions. During the phase change process, the interfaces $\Gamma_{L\phi}$, $\Gamma_{S\phi}$ changed their shapes and positions with time, while in the liquid and solid regions, the temperature and the area of each region changed continuously. All of these were strong functions of time.

Discretization of the Governing Equations

Some of the papers on heat and mass transfer derived the finite-difference equation via the Taylor-series method and then demonstrated that the resulting equation was consistent with a heat balance over a small region surrounding a grid point (Smith, 1978, Shih and Chen, 1983).

This study employed a control-volume formulation to discretize the governing equations and boundary conditions. The continuous physical space (hemispherical droplet) was divided into a number of non-overlapping control volumes in the (r, θ) plane such that there was one control volume surrounding each grid point. The differential equation was integrated over each control volume. Figure 3.3 shows a 20×20 grid (20 nodes in the radial direction and 20 nodes in the angular direction).

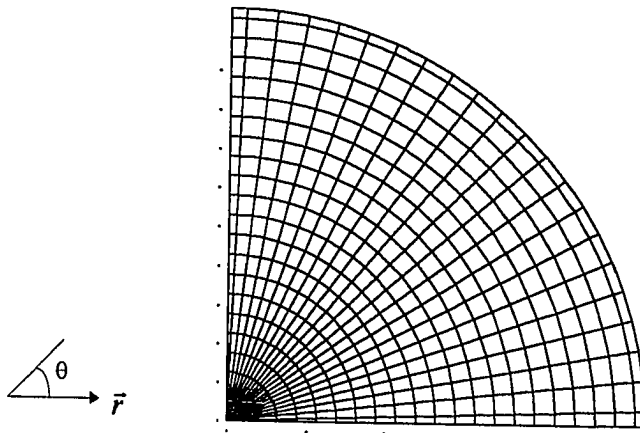


Figure 3.3 The grid generation for a hemispherical droplet in spherical coordinates.

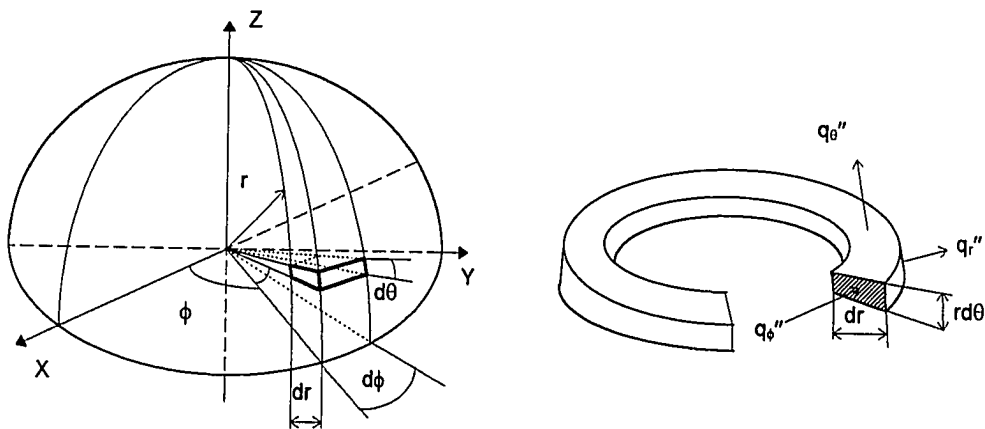


Figure 3.4 A control volume, $r^2 \cos(\theta) \cdot dr \cdot d\theta \cdot 2\pi r \cos(\theta)$, for conduction analysis in spherical coordinates (r, θ, ϕ) .

The most attractive feature of the control-volume formulation is that the resulting solution would imply that the integral conservation of energy is exactly satisfied over any group of control volumes and over the whole calculation domain. This characteristic exists for any number of grid points — not just in a limiting sense when the number of grid points becomes large. Thus, even the coarse-grid solution exhibits exact integral balances (Patankar, 1980).

Considered a hemispherical droplet in which temperature gradients existed and the temperature distribution $T(r, \theta, t)$ was expressed in spherical coordinates. Following the methodology of applying conservation of energy, a ring control volume $r^2 \cos(\theta) \cdot dr \cdot d\theta \cdot 2\pi r \cdot \cos(\theta)$ was picked (Figure 3.4). Choosing to formulate the first law of thermodynamics at an interval of time, the energy processes that were relevant to this ring control volume were considered. If there were temperature gradients, conduction heat transfer would occur across each of the control surfaces. The conduction heat flux perpendicular to each of the control surfaces at the r, θ, ϕ coordinate locations were indicated by the terms q_r'' , q_θ'' , q_ϕ'' , respectively.

$$q_r'' = -k \frac{\partial T}{\partial r} \quad (3.8)$$

$$q_\theta'' = -\frac{k}{r} \frac{\partial T}{\partial \theta} \quad (3.9)$$

$$q_\phi'' = -\frac{k}{r \cos(\theta)} \frac{\partial T}{\partial \phi} \quad (3.10)$$

If the temperature did not change in ϕ -direction, then the governing equation would be in the form in Eqs.(3.1) and (3.2).

Figure 3.5 shows a magnified interior node and its neighbor nodes. Applying the energy balance to the control volume shown in Figure 3.5, yielded:

$$\begin{aligned}
 & \Delta r \cdot r \Delta \theta \cdot \frac{\pi}{2} r \cos(\theta) \cdot \rho C_p \frac{[T(i, j) - T^0(i, j)]}{\Delta t} = \\
 & k \cdot \Delta r \cdot \frac{\pi}{2} r \cos(\theta) \cdot \frac{[T(i+1, j) - T(i, j)]}{r \Delta \theta} \\
 & + k \cdot \Delta r \cdot \frac{\pi}{2} r \cos(\theta) \cdot \frac{[T(i-1, j) - T(i, j)]}{r \Delta \theta} \quad (3.11) \\
 & + k \cdot r^2 \Delta \theta \cdot \frac{\pi}{2} \cos(\theta) \cdot \frac{[T(i, j+1) - T(i, j)]}{\Delta r} \\
 & + k \cdot r^2 \Delta \theta \cdot \frac{\pi}{2} \cos(\theta) \cdot \frac{[T(i, j-1) - T(i, j)]}{\Delta r}
 \end{aligned}$$

Eq.(3.11) was simplified to:

$$\begin{aligned}
 & \Delta r \cdot r \Delta \theta \cdot \rho C_p \frac{[T(i, j) - T^0(i, j)]}{\Delta t} = k \cdot \frac{\Delta r}{r \Delta \theta} \cdot [T(i+1, j) - T(i, j)] \\
 & + k \cdot \frac{\Delta r}{r \Delta \theta} \cdot [T(i-1, j) - T(i, j)] + k \cdot \frac{r \Delta \theta}{\Delta r} [T(i, j+1) - T(i, j)] \quad (3.12) \\
 & + k \cdot \frac{r \Delta \theta}{\Delta r} [T(i, j-1) - T(i, j)]
 \end{aligned}$$

The discretization equation had the form:

$$\begin{aligned}
 & a(i, j)T(i, j) = a(i+1, j)T(i+1, j) + a(i-1, j)T(i-1, j) \\
 & + a(i, j+1)T(i, j+1) + a(i, j-1)T(i, j-1) \quad (3.13) \\
 & + a^0(i, j)T(i, j) + b
 \end{aligned}$$

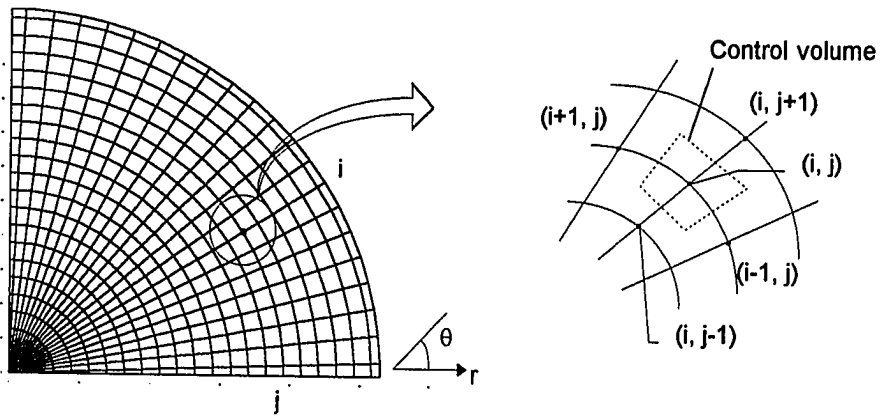


Figure 3.5 An interior node and its neighbor nodes.

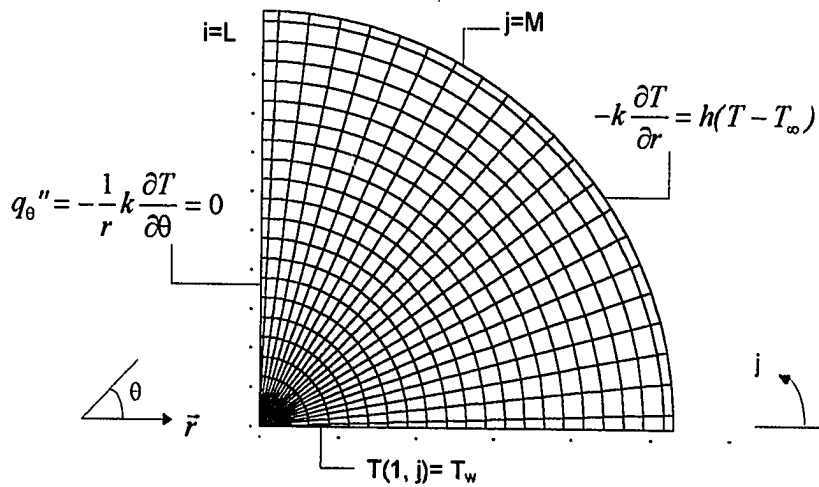


Figure 3.6 Three kinds of boundary conditions encountered in a droplet.

Comparing Eqs.(3.12) and (3.13), the coefficients in the discretization equation could be written as:

$$\begin{aligned} \alpha(i, j+1) &= k \frac{r\Delta\theta}{\Delta r} \\ \alpha(i, j-1) &= k \frac{r\Delta\theta}{\Delta r} \\ \alpha(i+1, j) &= k \frac{\Delta r}{r\Delta\theta} \end{aligned} \quad (3.14)$$

$$\begin{aligned} \alpha(i-1, j) &= k \frac{\Delta r}{r\Delta\theta} \\ \alpha^0(i, j) &= \rho C \frac{r\Delta r\Delta\theta}{\Delta t} \\ b &= 0 \end{aligned} \quad (3.15)$$

$$a(i, j) = \alpha(i, j+1) + \alpha(i, j-1) + \alpha(i+1, j) + \alpha(i-1, j) + \alpha^0(i, j)$$

Next, the control volume method was applied to the nodes at the three boundaries of a droplet. Figure 3.6 shows three different kinds of boundary conditions in this study. Figure 3.7 is a magnified boundary node with its neighborhood nodes.

Applying an energy balance on the control volume surrounding node (i, j) :

$$\begin{aligned} &\frac{\Delta r}{2} \cdot r\Delta\theta \cdot \frac{\pi r}{2} \cos(\theta) \cdot \rho C_p \cdot \frac{[T(i, j) - T^0(i, j)]}{\Delta t} = \\ &h \cdot r\Delta\theta \cdot \frac{\pi r}{2} \cos(\theta) \cdot [T_\infty - T(i, j)] \\ &+ k \cdot \frac{\Delta r}{2} \cdot \frac{\pi r}{2} \cos(\theta) \cdot \frac{[T(i+1, j) - T(i, j)]}{r\Delta\theta} \\ &+ k \cdot \frac{\Delta r}{2} \cdot \frac{\pi r}{2} \cos(\theta) \cdot \frac{[T(i-1, j) - T(i, j)]}{r\Delta\theta} \\ &+ k \cdot r\Delta\theta \cdot \frac{\pi r}{2} \cos(\theta) \cdot \frac{[T(i, j-1) - T(i, j)]}{\Delta r} \end{aligned} \quad (3.16)$$

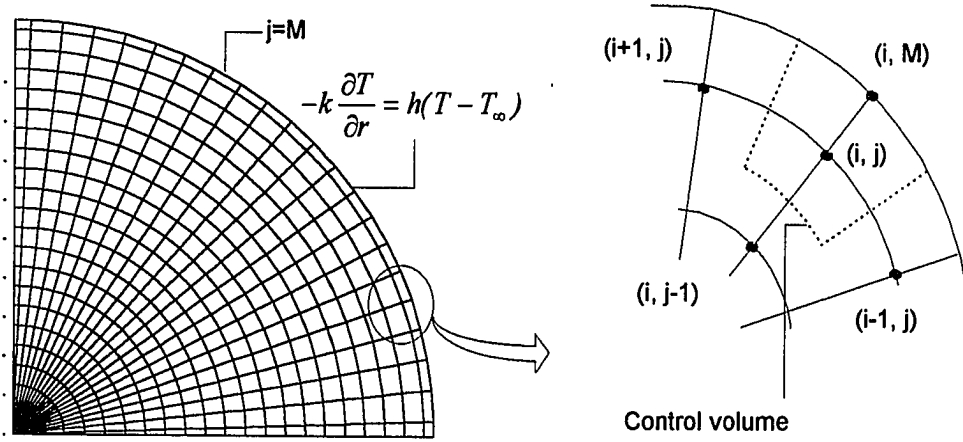


Figure 3.7 The magnified boundary node and its neighbor nodes.

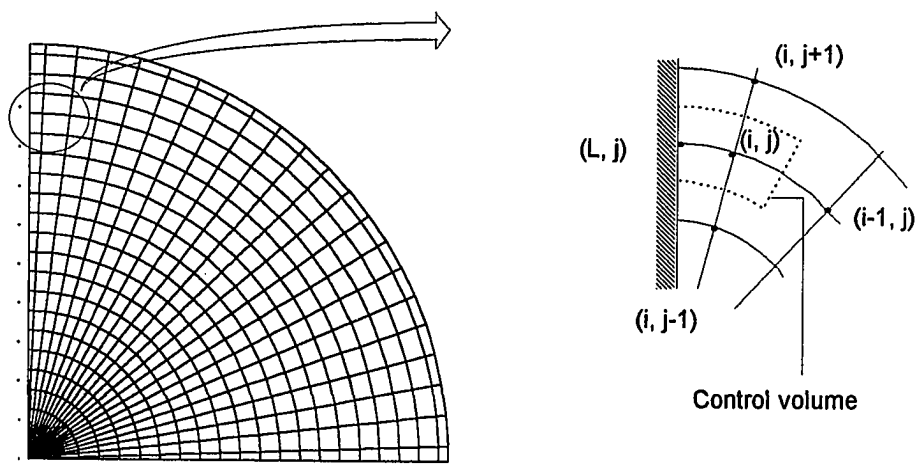


Figure 3.8 The boundary node and its neighbor nodes at the symmetric plane.

The above expression could be simplified and written as:

$$\begin{aligned} \frac{\Delta r}{2} \cdot r \Delta \theta \cdot \rho C_p \cdot \frac{[T(i, j) - T^0(i, j)]}{\Delta t} = \\ h \cdot r \Delta \theta \cdot [T_\infty - T(i, j)] + \frac{k \Delta r}{2r \Delta \theta} \cdot [T(i+1, j) - T(i, j)] \\ + \frac{k \Delta r}{2r \Delta \theta} \cdot [T(i+1, j) - T(i, j)] + k \frac{r \Delta \theta}{\Delta r} [T(i, j-1) - T(i, j)] \end{aligned} \quad (3.17)$$

The discretization equation of the above could be written as:

$$\begin{aligned} a(i, j)T(i, j) = a(i, j+1)T(i, j+1) + a(i, j-1)T(i, j-1) \\ + a(i-1, j)T(i-1, j) + a(i+1, j)T(i+1, j) \\ + a^0(i, j)T^0(i, j) + b \end{aligned} \quad (3.18)$$

where the coefficients in the discretization equation were:

$$\begin{aligned} a(i, j+1) &= h \cdot r \Delta \theta \\ a(i, j-1) &= \frac{k \cdot r \Delta \theta}{\Delta r} \\ a(i-1, j) &= \frac{k \cdot \Delta r}{2r \Delta \theta} \\ a(i+1, j) &= \frac{k \cdot \Delta r}{2r \Delta \theta} \\ a^0(i, j) &= \frac{r \Delta \theta \Delta r}{2} \rho C_p \\ b &= 0 \end{aligned} \quad (3.19)$$

$$a(i, j) = a(i, j+1) + a(i, j-1) + a(i-1, j) + a(i+1, j) + a^0(i, j)$$

Figure 3.8 shows the magnified boundary node and its neighbor nodes at the symmetric plane of a hemispherical droplet. Applying the first law of thermodynamics to the control volume and simplifying yielded:

$$\begin{aligned}
 & \Delta r \cdot \frac{r\Delta\theta}{2} \cdot \frac{\pi r}{2} \cos(\theta) \cdot \rho C_p \cdot \frac{[T(i, j) - T^0(i, j)]}{\Delta t} = \\
 & k \cdot \frac{r\Delta\theta}{2} \cdot \frac{\pi r}{2} \cos(\theta) \cdot \frac{[T(i, j+1) - T(i, j)]}{\Delta r} \\
 & + k \cdot \frac{r\Delta\theta}{2} \cdot \frac{\pi r}{2} \cos(\theta) \cdot \frac{[T(i, j-1) - T(i, j)]}{\Delta r} \\
 & + k \cdot \Delta r \cdot \frac{\pi r}{2} \cos(\theta) \cdot \frac{[T(i-1, j) - T(i, j)]}{r\Delta\theta}
 \end{aligned} \tag{3.20}$$

Simplifying the above equation led to:

$$\begin{aligned}
 \Delta r \cdot \frac{r\Delta\theta}{2} \cdot \rho C_p \cdot \frac{[T(i, j) - T^0(i, j)]}{\Delta t} &= k \cdot \frac{r\Delta\theta}{2} \cdot \frac{[T(i, j+1) - T(i, j)]}{\Delta r} \\
 + k \cdot \frac{r\Delta\theta}{2} \cdot \frac{[T(i, j-1) - T(i, j)]}{\Delta r} &+ k \cdot \Delta r \cdot \frac{[T(i-1, j) - T(i, j)]}{r\Delta\theta}
 \end{aligned} \tag{3.21}$$

Where the discretization equation can be written as:

$$\begin{aligned}
 a(i, j)T(i, j) &= a(i, j+1)T(i, j+1) + a(i, j-1)T(i, j-1) \\
 + a(i-1, j)T(i-1, j) &+ a(i+1, j)T(i+1, j) \\
 + a^0(i, j)T^0(i, j) &+ b
 \end{aligned} \tag{3.22}$$

The coefficients in the discretization equation were given by:

$$\begin{aligned}
 a(i, j+1) &= \frac{kr\Delta\theta}{2\Delta r} \\
 a(i, j-1) &= \frac{k \cdot r\Delta\theta}{2\Delta r} \\
 a(i-1, j) &= \frac{k \cdot \Delta r}{r\Delta\theta} \\
 a(i+1, j) &= 0 \\
 a^0(i, j) &= \frac{r\Delta\theta\Delta r}{2} \rho C_p \\
 b &= 0
 \end{aligned} \tag{3.23}$$

$$a(i, j) = a(i, j+1) + a(i, j-1) + a(i-1, j) + a(i+1, j) + a^0(i, j)$$

Figure 3.9 shows the node at the phase change region and its adjacent nodes. For the freezing of a hemispherical droplet sitting on a cold plate, the freezing front was expected to be a concave layer as shown in Figure 3.9. Since the orthogonal grid was in spherical coordinates, the surrounding nodes of a node might be in liquid, or phase change, or solid region. It was because of this reason that the phase change region appeared in a zone, rather than a zero thickness interface. Here a typical case was employed to show the development of discretization equation in the phase change region. Figure 3.9 shows the magnified nodal network.

Applying the energy conservation requirement to the control volume associated with (i, j) node:

$$\begin{aligned}
 h_{sf} \cdot \rho(i, j) \cdot \Delta r \cdot r \Delta \theta \cdot \frac{\pi r}{2} \cos(\theta) = & \\
 k(i, j+1) \cdot r \Delta \theta \cdot \frac{\pi r}{2} \cos(\theta) \cdot \frac{[T(i, j+1) - T(i, j)]}{\Delta r} & \\
 + k(i, j-1) \cdot r \Delta \theta \cdot \frac{\pi r}{2} \cos(\theta) \cdot \frac{[T(i, j-1) - T(i, j)]}{\Delta r} & \quad (3.24) \\
 + k(i+1, j) \cdot \Delta r \cdot \frac{\pi r}{2} \cos(\theta) \cdot \frac{[T(i+1, j) - T(i, j)]}{r \Delta \theta} & \\
 + k(i-1, j) \cdot \Delta r \cdot \frac{\pi r}{2} \cos(\theta) \cdot \frac{[T(i-1, j) - T(i, j)]}{r \Delta \theta} &
 \end{aligned}$$

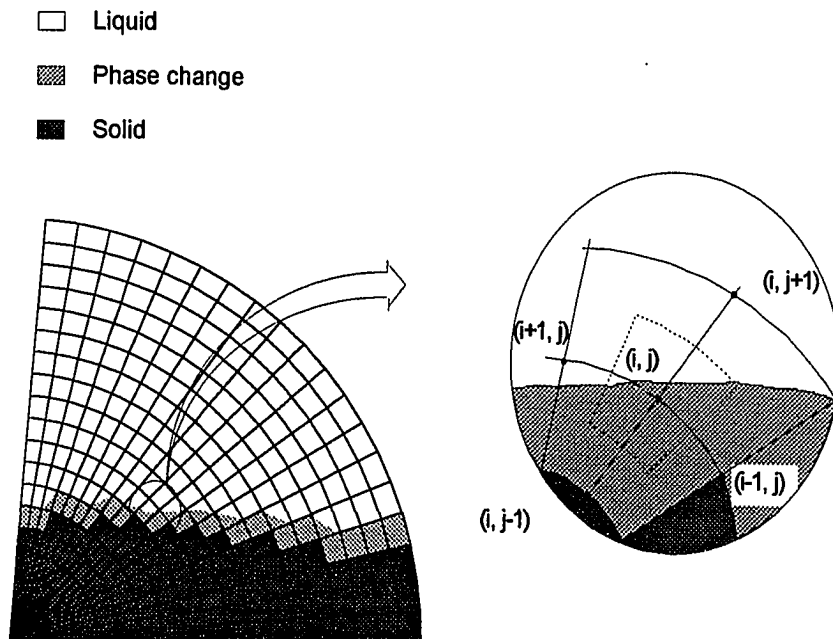


Figure 3.9 A node at the phase change region and its adjacent nodes.

The above could be simplified:

$$\begin{aligned}
 h_{sf} \cdot \rho(i, j) \cdot \Delta r \cdot r \Delta \theta &= k(i, j+1) \cdot r \Delta \theta \cdot \frac{[T(i, j+1) - T(i, j)]}{\Delta r} \\
 &+ k(i, j-1) \cdot r \Delta \theta \cdot \frac{[T(i, j-1) - T(i, j)]}{\Delta r} + \\
 k(i+1, j) \cdot \Delta r \cdot \frac{[T(i+1, j) - T(i, j)]}{r \Delta \theta} & \\
 &+ k(i-1, j) \cdot \Delta r \cdot \frac{[T(i-1, j) - T(i, j)]}{r \Delta \theta}
 \end{aligned} \tag{3.25}$$

The discretization equation for Eq.(3.25) was:

$$\begin{aligned}
 a(i, j)T(i, j) &= a(i, j+1)T(i, j+1) + a(i, j-1)T(i, j-1) \\
 &+ a(i-1, j)T(i-1, j) + a(i+1, j)T(i+1, j) \\
 &+ a^0(i, j)T^0(i, j) + b
 \end{aligned} \tag{3.26}$$

where the coefficients in the discretization equation were given by:

$$\begin{aligned}
 a(i, j+1) &= \frac{k(i, j)r\Delta\theta}{\Delta r} \\
 a(i, j-1) &= \frac{k(i, j-1) \cdot r\Delta\theta}{\Delta r} \\
 a(i-1, j) &= \frac{k(i-1, j) \cdot \Delta r}{r\Delta\theta} \\
 a(i+1, j) &= \frac{k(i+1, j) \cdot \Delta r}{r\Delta\theta} \\
 a^0(i, j) &= 0 \\
 b &= -h_{sf} \cdot \rho(i, j) \cdot r \Delta r \Delta \theta \\
 S_c &= h_{sf} \cdot \rho(i, j)
 \end{aligned} \tag{3.27}$$

$$a(i, j) = a(i, j+1) + a(i, j-1) + a(i-1, j) + a(i+1, j) + a^0(i, j)$$

The model assumed that all thermophysical properties depended on phase state only and were uniform throughout the liquid, solid, and phase change region, respectively. If a node was in the phase change region, its neighbor nodes could be in one of the three regions. The harmonic-mean formula (Patankar, 1980) was used to handle the discontinuities in the distributions of properties for Eq.(3.27). The nodes (i, j) , $(i+1, j)$, $(i-1, j)$, $(i, j+1)$, $(i, j-1)$ shown in Figure 3.9 were taken as an example to show how this assumption worked.

$$\begin{aligned}
 k(i, j) &= \frac{2k_s k_l}{k_s + k_l} \\
 k(i, j+1) &= k_l \\
 k(i, j-1) &= k_s \\
 k(i+1, j) &= k_l \\
 k(i-1, j) &= \frac{2k_s k_l}{k_s + k_l}
 \end{aligned} \tag{3.28}$$

After the discretization of governing equations and boundary conditions, every node (i, j) ($i=1, 2, 3, \dots, L, j=1, 2, 3, \dots, M$) had a equation like the following:

$$\begin{aligned}
 a(i, j)T(i, j) &= a(i, j+1)T(i, j+1) + a(i, j-1)T(i, j-1) \\
 &+ a(i-1, j)T(i-1, j) + a(i+1, j)T(i+1, j) \\
 &+ a^0(i, j)T^0(i, j) + b
 \end{aligned} \tag{3.29}$$

Eq.(3.29) was a set of simultaneous algebraic relations. Advanced numerical methods were available for solving such algebraic equations to get temperature at each node.

Based on the temperature field, the heat transfer study was calculated by applying the Fourier's law. The heat transfer through three boundaries of the hemispherical

droplet were calculated. For a quarter of a hemispherical droplet, the heat transfer through the symmetric plane ($i=L$) should be zero. The local heat transfer rate through the surface at $\theta=\theta_1$ was

$$q|_{\theta=\theta_1} = -k \left[\frac{T(i, M-1) - T(i, M)}{\Delta r} \right] \quad (3.30)$$

and the local heat transfer rate through the base of a droplet at $r=r_1$

$$q|_{r=r_1} = -k \left[\frac{T(2, j) - T(1, j)}{r_1 \Delta \theta} \right] \quad (3.31)$$

by using Eqs.(3.30) and (3.31), the distributions of heat transfer rates at the surface and the base of a droplet can be obtained. These equations provided the information about where the heat transfer was largest.

After obtaining the local heat transfer rates, the total heat transfer rate through the surface of a quarter of a hemispherical droplet can be calculated by:

$$Q_s = \sum_{i=1}^L -k \left[\frac{T(i, M-1) - T(i, M)}{\Delta r} \right] r \Delta \theta \frac{\pi R \cos(\theta)}{2} \quad (3.32)$$

and the total heat transfer rate through the base was:

$$Q_b = \sum_{j=1}^M -k \left[\frac{T(2, j) - T(1, j)}{r \Delta \theta} \right] \Delta r \frac{\pi r \cos(0)}{2} \quad (3.33)$$

At this point, the credibility of the results of the mathematical model could be checked by the results obtained from Eq.(3.32) with results obtained by Eq.(3.33) when the droplet was in steady state. If they were equal to each other, the model results satisfied the first law of thermodynamics.

The flowchart for the start-up of the computational method is shown in Figure 3.10. The model calculation demanded an initial temperature for each of the interior nodes. Before entering the equation solving loop, an inner loop, temperature tracker, compared the temperature at each of the nodes with the freezing point of water and gave a special value to every node as a phase indicator (called flag value in this study). For example, 0 stood for liquid state, 1 for two phase regions, and 2 for solid state. Those flag values were saved in an independent data file during numerical iteration. At $t=0$, all of the flag values at the interior nodes should be 0, which indicated that it was initially a water droplet. Then the new nodal values were computed by using algebraic equations at next time Δt . The interior nodes would fall into three groups according to their temperatures. For these nodes whose temperatures were higher than the freezing point of water, they would stay in the liquid region for one or more time steps. The water properties and 0 (flag value) were assigned to this point. If the temperature at a node was at the freezing point of water, it just entered the phase change region. 1 (flag value) and the water properties at the triple-point were given to this node. Eq.(3.24) was used to decide when this node would get out of the phase transition process. Put it straight, if the total amount of energy transferred out of the node was greater than the latent enthalpy of freezing of water, this node was completely frozen. Thus, 2 (flag value) and ice properties were assigned to this node.

The flag values for all of the nodes were saved in an independent data file during numerical iteration. By using a spectral plot (Figure 3.9), these three different flag

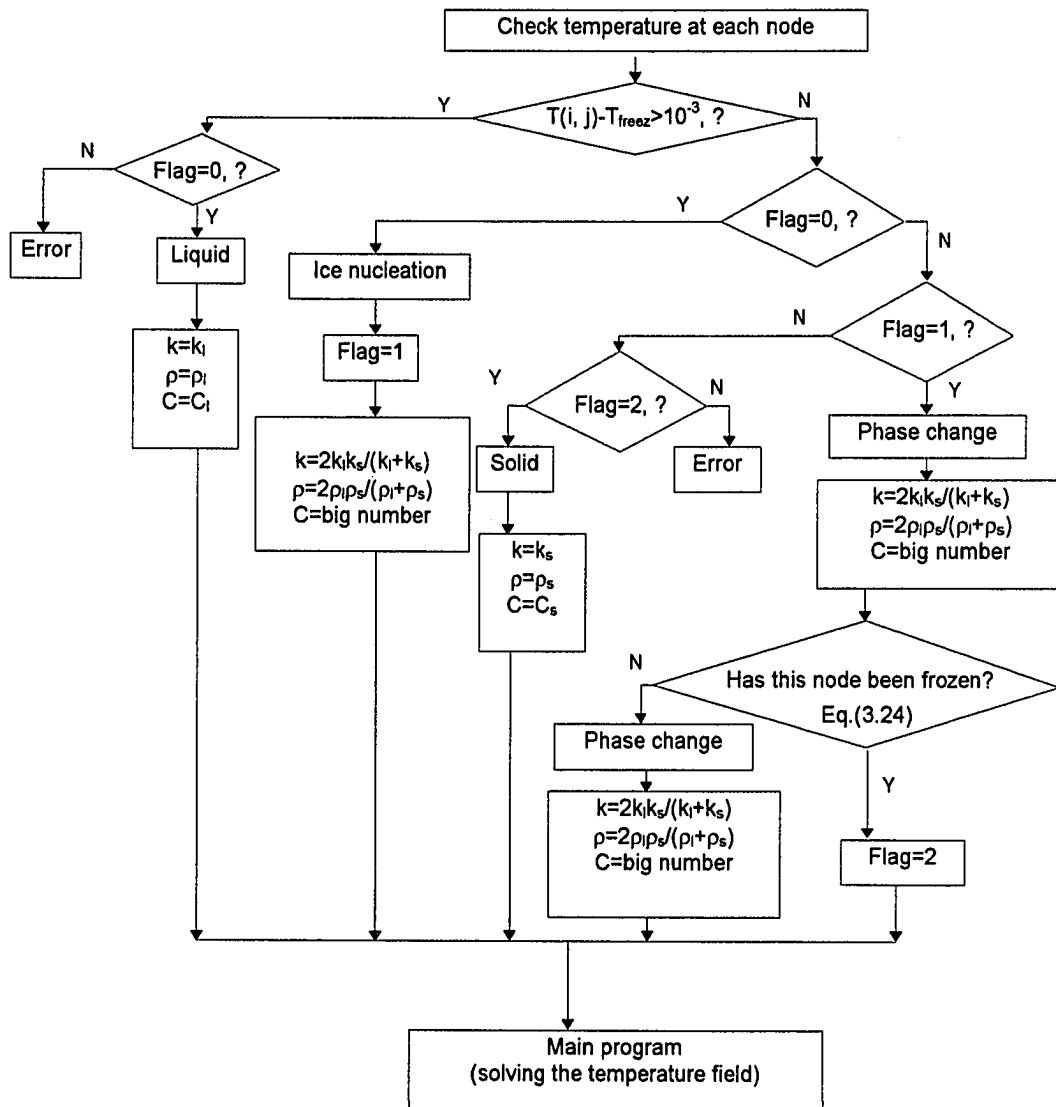


Figure 3.10 The flowchart for computational process.

values at a time were presented with three different colors. This colorful layout of the model results acted as one frame of a motion picture. Movie-making software was needed to take continuous snapshots of individual frames and a mini-movie was made to simulate the entire freezing process of a hemispherical droplet.

The transient information about the state of every nodal element made it possible to calculate the velocity of the freezing front. In this study, a simple definition was introduced to show the magnitude of the freezing front velocity. Figure 3.11 shows a spectral plot of the transient state information for a hemispherical droplet during freezing. At time t_1 , the node (i_1, j_1) starts to freeze. The freezing front moved upward to node (i_2, j_2) at time t_2 . If the distance covered by the freezing front during this time period $\Delta t = t_2 - t_1$ was ΔS , then the local average velocity was defined by

$$V_i = \frac{\Delta S}{\Delta t} \quad (3.34)$$

In this study, a mathematical model was developed to solve the partial differential energy equations under some boundary and initial conditions. Because the implicit scheme was chosen, the calculation procedure would be unconditionally stable. The time step Δt might be chosen as large as one wanted but the inaccuracy of the model results increased with increasing Δt . However, even if $\Delta t \rightarrow 0$, neither mathematical model was “exact”, the inaccuracy depending on the crudeness of the spatial mesh size

Δr and $\Delta\theta$. For most cases, a relative convergence of 10^{-4} was specified as

$$\left| \frac{T^{n+1}(i, j) - T^n(i, j)}{T^{n+1}(i, j)} \right| \leq 10^{-4} \quad (3.35)$$

where i and j represent the arbitrary nodes, and the superscript n represents the n th iteration.

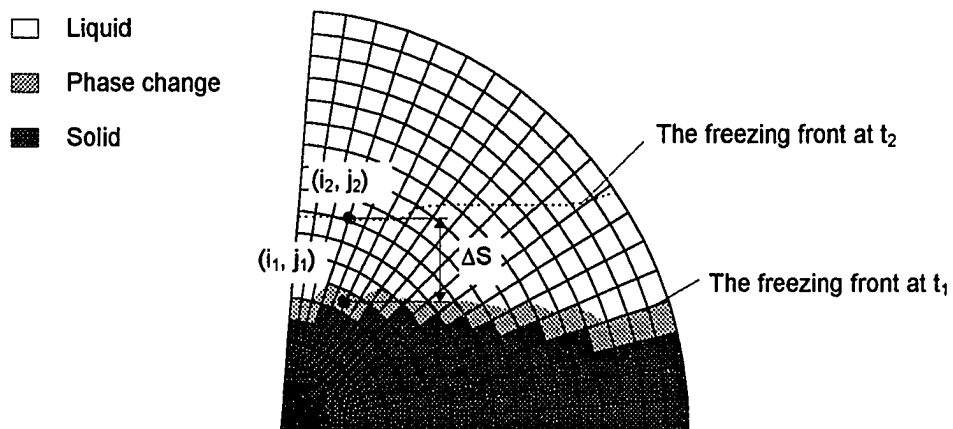


Figure 3.11 The definition of the velocity of the freezing front.

CHAPTER IV

MATHEMATICAL MODEL RESULTS

4.1 Model Predictions

The flowchart for the mathematical model was given in Figure 3.10. At time $t=0$, an arbitrary temperature ($T>0^{\circ}\text{C}$) was assumed to each node in the computational domain. Eqs.(3.1) and (3.2) were solved subject to the boundary conditions in Eqs.(3.3) to (3.7) by using a finite-difference scheme. Thus, the temperature distribution, the heat transfer rates through the boundaries, the velocity of the freezing front, the area fraction of solid, the position of the freezing front, and the freezing time could be obtained. At every time step, the temperature at each node point was compared with the freezing temperature and a flag value designed for the spectral plot was assigned to each of the nodes during the successive calculations.

Steady-State Temperature Distribution and Heat Transfer in the Liquid Phase

If the cold metal plate temperature was higher than the freezing temperature of water, the temperature at each nodal element in the computational domain would be higher than the freezing temperature and the entire droplet should be in the liquid phase. Hence, the problem was reduced to the solving of a two-dimensional steady-state

temperature distribution in a hemispherical droplet under two different boundary conditions.

Consider a hemispherical droplet with a 1.32 mm radius that was initially at the ambient air temperature of 25.6°C and was formed on a cold metal plate with $T_w = 3.8^\circ\text{C}$. If the cooling of the droplet began at time $t=0$, the temperature at every point inside the droplet would decrease for time $t>0$, until it eventually reached a steady value.

The computation domain was assumed to have 40×40 nodes and made use of uniform increments in both radial and angular directions. The air-side convection coefficients used in the Eqs.(3.3) and (3.4) were measured values, which were discussed in Chapter VI. Following are some results and discussions.

Figure 4.1 shows the dimensionless temperature Ξ ($\Xi = (T-T_\infty)/(T_w-T_\infty)$) in the radial direction at $\theta=15.8^\circ$, 60.8° , and 90° , respectively. The radial temperature distribution corresponding to a large θ was approximately linear, while around the perimeter area where θ was small, the temperature gradient increased with increasing radial location.

The local heat flux $q''(\theta, R)$ at the surface of the droplet was calculated with Eq.(3.29) and the results were presented in Figure 4.2. The heat flux was large in the vicinity of the perimeter, and then it kept dropping down with increasing θ . The same conclusion could be obtained by comparing the temperature gradient at the right-hand end of their respective curves in Figure 4.1. Results showed that approximately 40% of

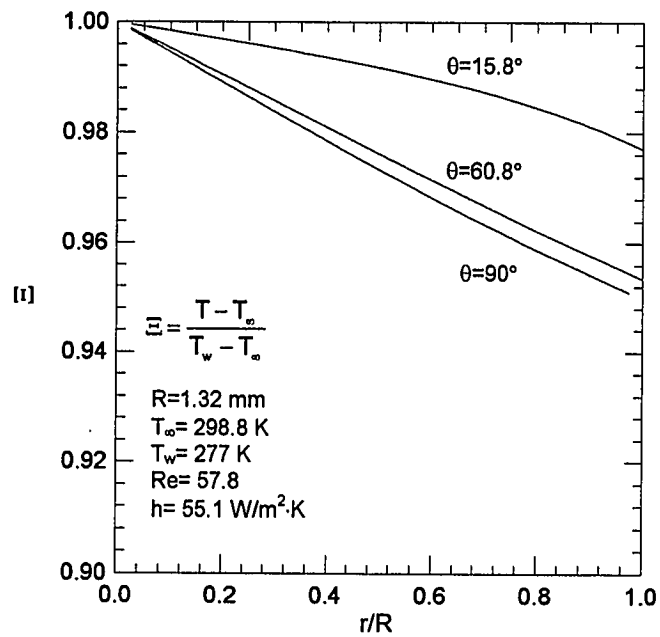


Figure 4.1 The temperature distribution in radial direction.

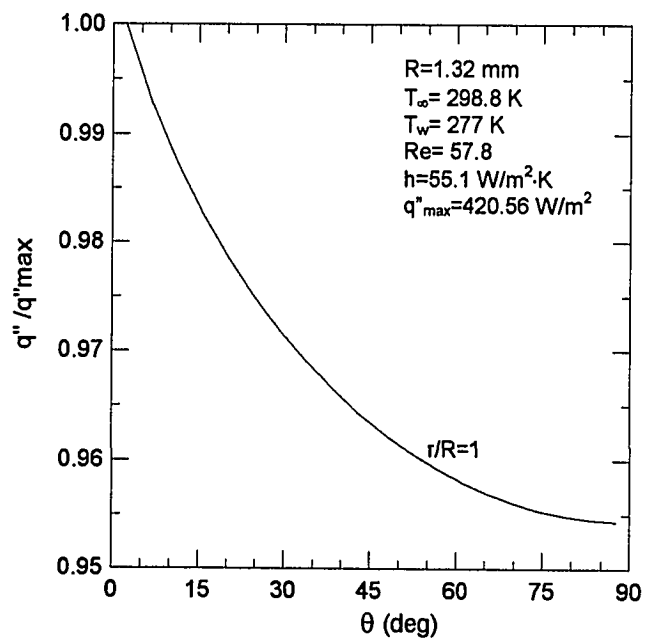


Figure 4.2 The local heat flux through the surface of a droplet.

the total heat transfer through the surface of a hemispherical droplet ($Q=2.75 \times 10^{-3}$ W) occurred in the $0^\circ < \theta < 20^\circ$ ring area, as shown in Figure 4.3.

Figure 4.4 illustrates how the temperature Ξ ($(T-T_\infty)/(T_w-T_\infty)$) varies with respect to θ while holding the radial location r constant. The results showed that the maximum temperature gradient occurred at $\theta=0^\circ$, which was where the droplet contacted the cold metal surface. The temperature Ξ ($(T-T_\infty)/(T_w-T_\infty)$) decreased with increasing θ . It was obvious that the temperature at the base of a hemispherical droplet which closed to the metal surface temperature was lower than the temperature at the upper part of the droplet, implying that the density at the base was higher than the other places. The density changes in a liquid droplet would act to oppose, rather than encourage natural convection.

Figure 4.5 shows that the local heat flux calculated with Eq.(3.30) at the base of a droplet increases with increasing radial location r . The perimeter area with $0.76 < r/R < 1$ shown in Figure 4.6, accounted for 50% of the total amount heat transferred through the base of a hemispherical droplet ($Q=2.75 \times 10^{-3}$ W).

Hurst's results (1966) supported this conclusion. As illustrated in Figure 4.7, he performed the analysis of a single condensate droplet on a cold metal plate. It consisted of two parts: a droplet of fixed diameter together with the condensing surface immediately under it, and a surrounding section of the condensing surface, which was assumed to be condensate free. Hurst used the finite-element method to develop the mathematical model and his results showed that the temperature increased as the edge of the droplet was approached from the core of the droplet. It was found that 83 to 98

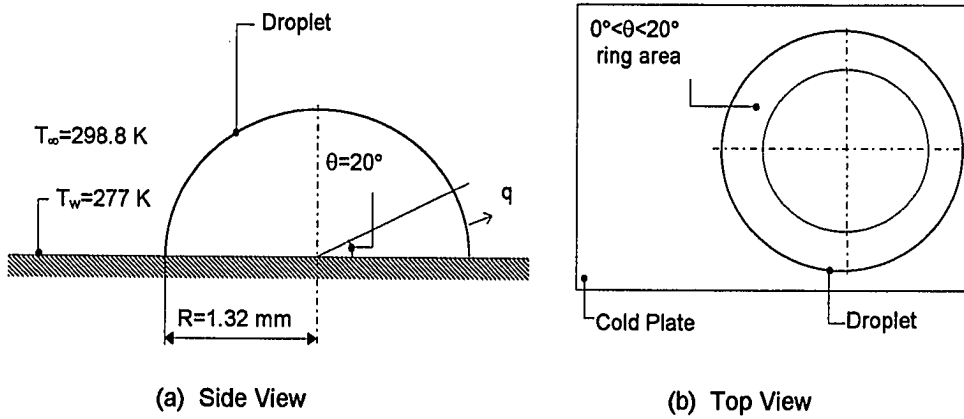


Figure 4.3 Local heat transfer at the surface of a hemispherical droplet.

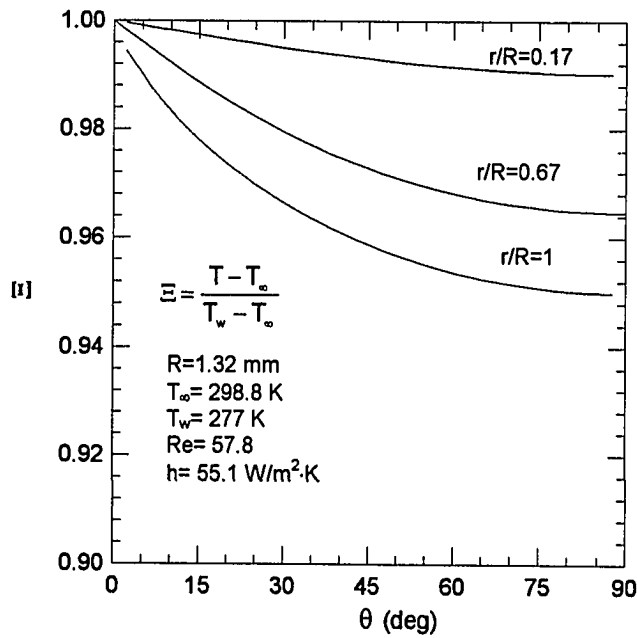


Figure 4.4 The temperature distribution in angular direction.

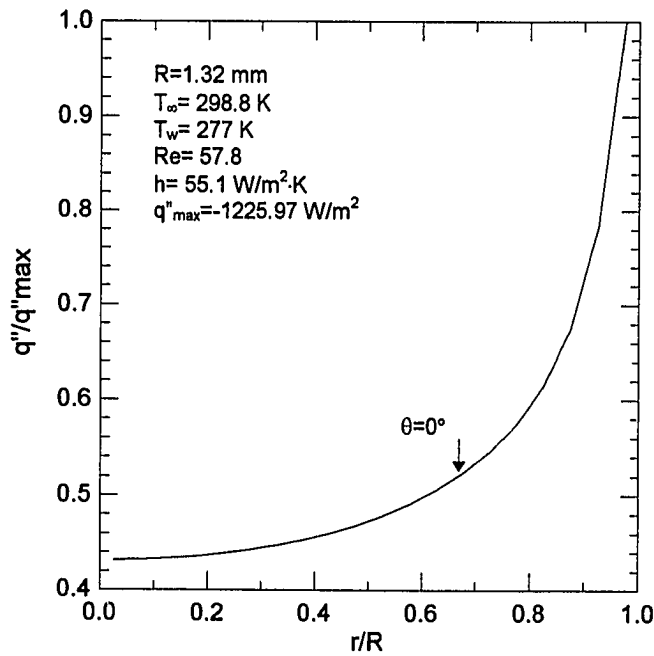


Figure 4.5 The local heat flux through the base of the droplet.

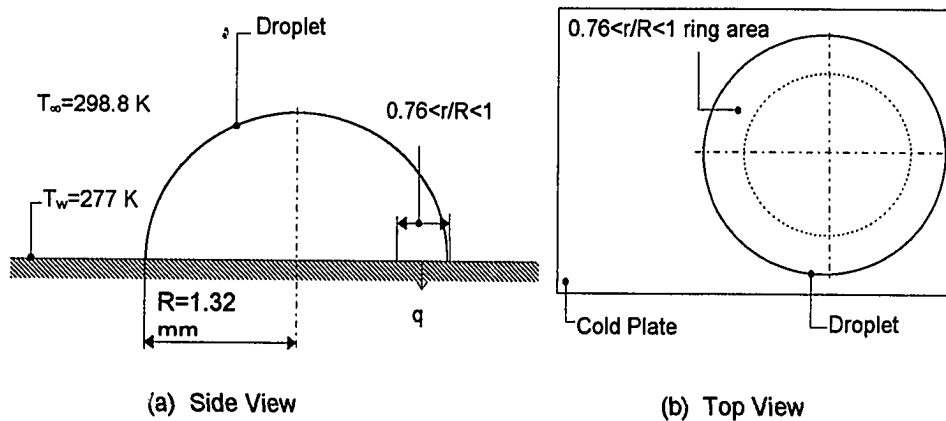


Figure 4.6 Local heat transfer at the base of a hemispherical droplet.

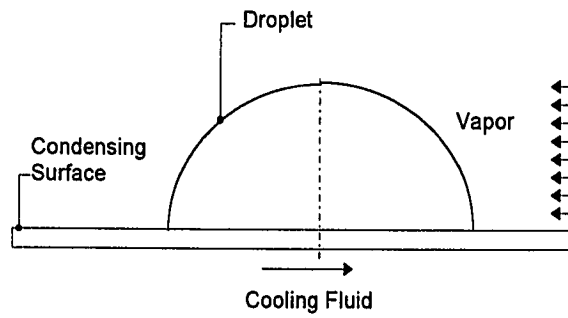


Figure 4.7 Single droplet model of Hurst (1966).

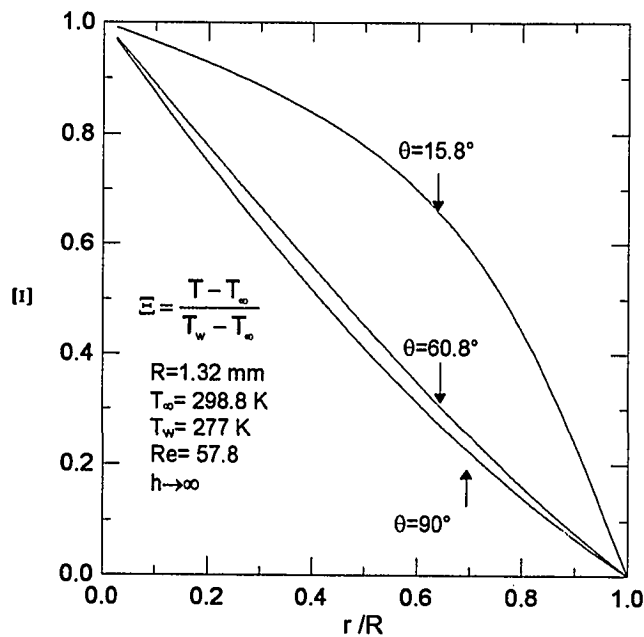


Figure 4.8 The temperature distribution in radius direction for limiting case ($h \rightarrow \infty$).

percent of the calculated total heat transfer through a droplet was coming in through the “corner” element ($0^\circ < \theta < 15^\circ$) where the hemispherical surface of the droplet intersected the plate surface.

One limiting case, an infinite air-side convection coefficient at the surface of the droplet, was studied to check the adaptability of the mathematical model and the reasonability of the temperature field. Figure 4.8 displays the radial temperature distribution with θ as a parameter. The infinite air-side convection coefficient led to a zero thermal resistance between the droplet surface and the ambient air. As a result, all of the curves approached the same point which equaled to the surface temperature of the ambient air (Figure 4.8). But the temperature gradients at the droplet surface varied with the θ angle nevertheless.

In angular direction, Figure 4.9 shows that the temperature distribution at the limiting case had the same trend as that shown in Figure 4.4. The Biot number was driven to infinity because of the infinite air-side convection coefficient at the droplet surface. As a result, the temperature difference across the droplet was much larger.

The local heat flux at the base of the droplet for the limiting case was shown in Figure 4.10. It displayed similar trends with the results presented in Figure 4.5. Sixty-six percent of the heat transfer through the droplet ($Q=3.98 \times 10^{-2} \text{W}$) occurred around the droplet perimeter with $0.76 < r/R < 1$.

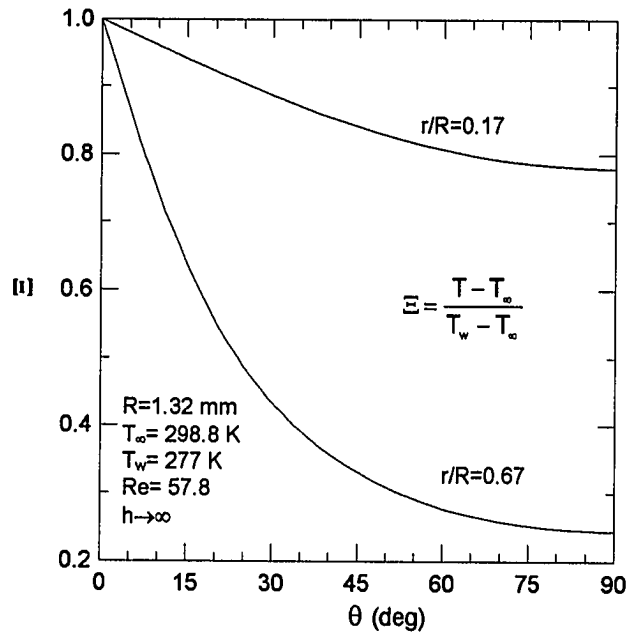


Figure 4.9 The temperature distribution in angular direction for limiting case ($h \rightarrow \infty$).

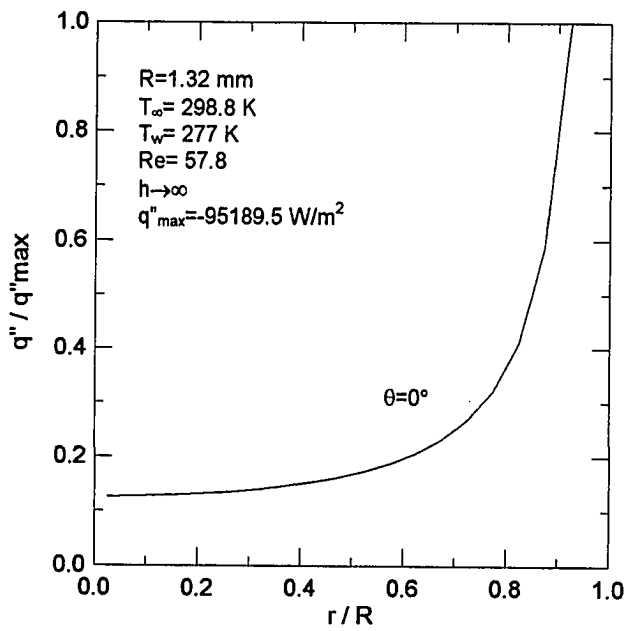


Figure 4.10 The local heat flux through the base of a droplet for the limiting case.

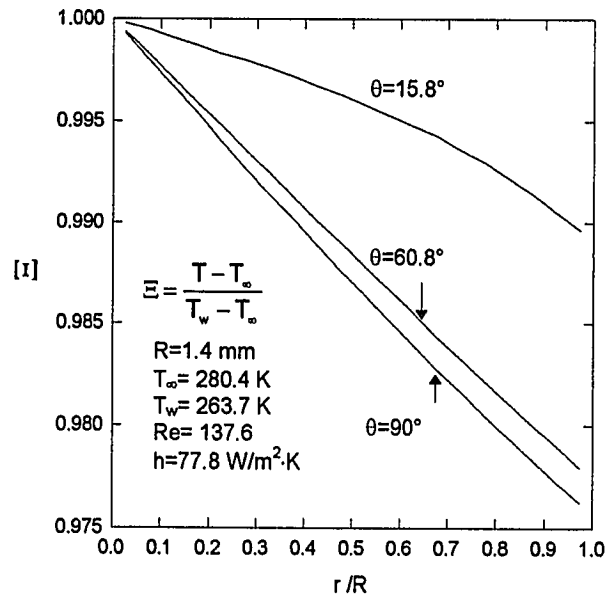


Figure 4.11 The steady-state temperature distribution in radial direction of a droplet in the solid phase.

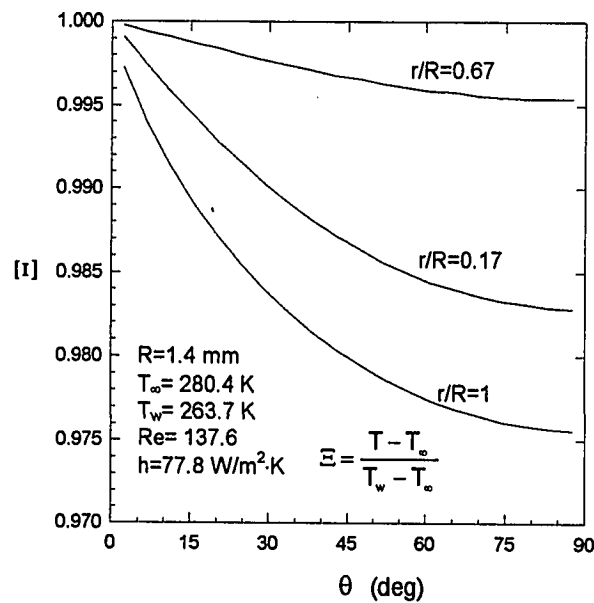


Figure 4.12 The steady-state angular temperature distribution of a droplet in the solid phase.

Steady-State Temperature field and Heat Transfer in the Solid Phase

The next important task was to run the mathematical model with the droplet as a solid, i.e., after a liquid droplet had frozen completely. The temperature field for an ice hemisphere with a 1.4 mm radius, ambient air temperature of 7.2°C, and plate temperature of -9.5°C was calculated. The air-side convection coefficient used in the model was a measured value (see Chapter VI). The mesh in the solid phase consisted of 40×40 nodes (40 nodes in radial direction and 40 nodes in angular direction) with $\Delta\theta=2.25^\circ$ and $\Delta r=0.035$ mm.

Figures 4.11 and 4.12 show the steady-state temperature distribution in the ice hemisphere. Figures 4.13 and 4.14 show the local heat fluxes at the surface and at the base of the ice hemisphere. Because the conduction was assumed the only heat transfer mode for both the solid and the liquid phases, the temperature distributions and the local heat fluxes in a liquid hemisphere and in an ice hemisphere had the same trend. The only difference was the magnitude of the values, which was caused by the difference of the thermophysical properties.

Transient Temperature Field and Heat Transfer During Freezing

The important behavior of freezing in a liquid droplet is characterized by a formation of the phase change zone, which separates two phases of differing thermophysical properties and at which the latent heat is released. To solve the problem

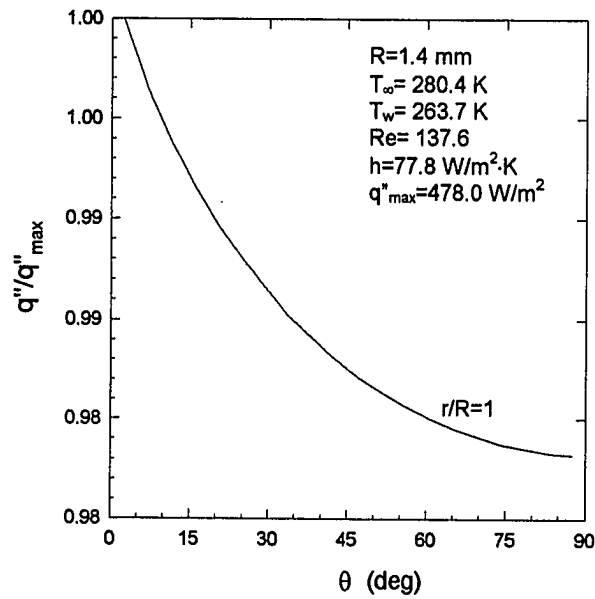


Figure 4.13 The heat flux through the surface of a droplet in the solid phase.

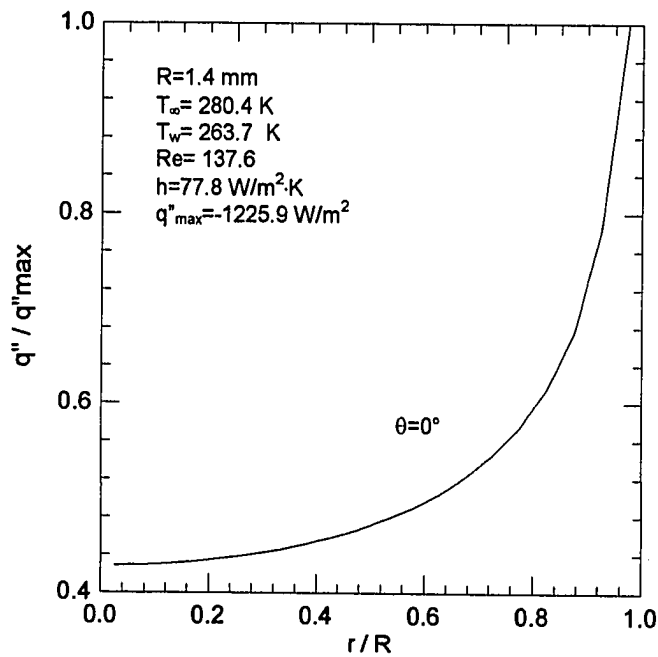


Figure 4.14 The heat flux through the base of a droplet in the solid phase.

with phase transition, a phase identifying subroutine was added to the numerical code and a computational procedure was detailed in Figure 3.10. The freezing of a hemispherical droplet was solved as an example, as illustrated in Figures 3.1 and 3.3. A hemispherical droplet of radius 1.4 mm was initially at temperature $T_{\infty}=280.4$ K. The metal plate temperature was then suddenly lowered to $T_w=263.7$ K while the air flow over the plate was kept at a low velocity.

The grid size employed in this case was 40×40 (40 nodes in radial direction and 40 nodes in angular direction) and the time step $\Delta t=0.03$ s was held constant for the entire time. Typical model results of transient temperature distribution and heat transfer for a hemispherical droplet during freezing were presented as followings. Figures 4.15, and 4.16 show the angular temperature distribution at $r/R=0.68$ and at the surface ($r/R=1$) of the partially frozen droplet illustrated in Figure 4.17. Because both of these two spherical surfaces cross the phase change region, each curve was composed of three portions, with each portion representing the temperature distribution in the solid, liquid, and phase change regions at the same time, respectively. In Figure 4.17, the phase change region was very thin comparing with the other two regions. There might be only one nodal element in the phase change region if an uniform mesh was selected. In Figures 4.15 and 4.16, the transient freezing front was at the bend of a curve corresponding an angle θ^* . For $\theta < \theta^*$, the part of the curve represented the transient temperature distribution in the solid region, which resembled the curves in Figure 4.11. And for $\theta > \theta^*$, it gave the temperature distribution in the liquid region, which had the same trend as the one in Figure 4.4. Figure 4.18 illustrated the transient distribution of

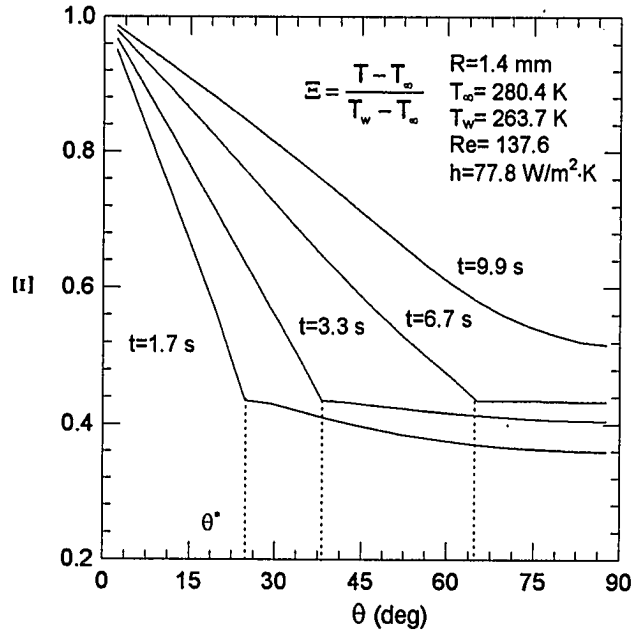


Figure 4.15 The transient temperature distribution ($r/R=0.68$).

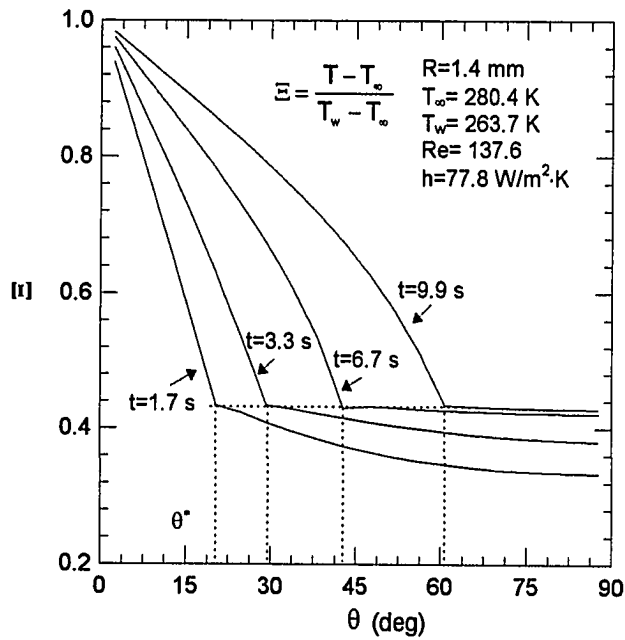


Figure 4.16 The temperature distribution at the surface of a droplet during freezing ($r/R=1$).

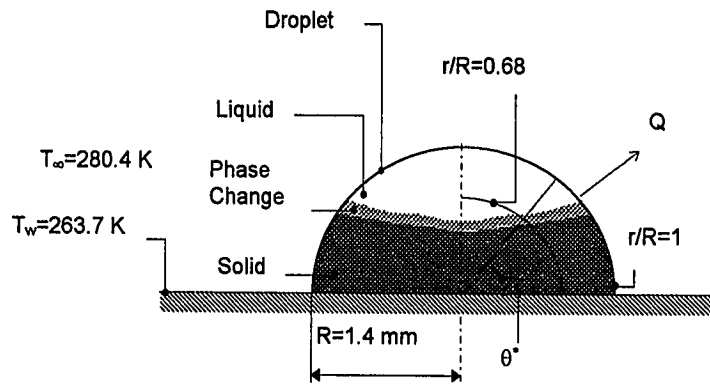


Figure 4.17 The positions inside a droplet at which the temperature distributions were plotted in Figures 4.15 and 4.16.

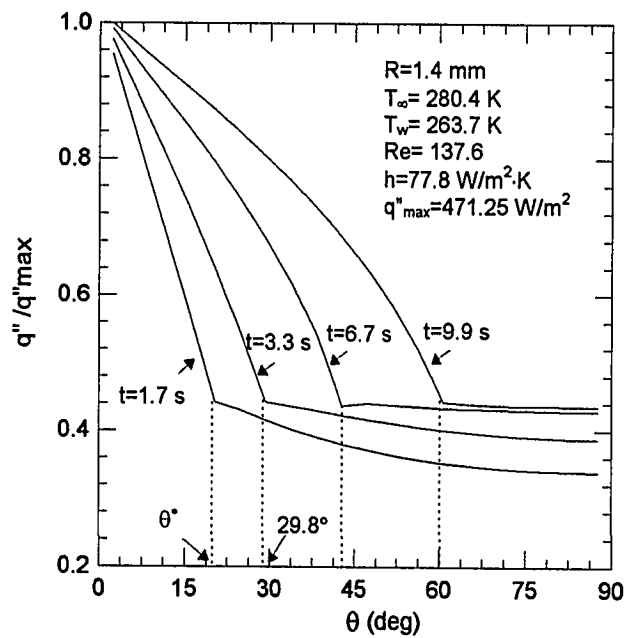


Figure 4.18 The heat flux through the surface of a droplet during freezing ($r/R=1$).

local heat flux at the droplet surface shown in Figure 4.17. The heat transfer in the solid region of the droplet was higher and decreased to lower values in the liquid region. For example, at $t=3.3$ s, the heat transfer through the solid region ($\theta < \theta^*$, $\theta^*=29.8^\circ$) took 71% of the total heat transfer through the surface of the droplet. In the liquid region of the surface, the local heat flux did not change appreciably with increasing θ .

In Figures 4.19 and 4.20, the transient radial temperature distributions are plotted at $\theta=60.8^\circ$ and $\theta=90^\circ$ shown in Figure 4.21. The curves verified the expectations and illustrated the transient temperature distributions in different phase regions. If r^* was used to represent the phase-change interface in the radial direction, it was noticed that r^* in Figure 4.20 was smaller than that in Figure 4.19 corresponding to the same time t , which implied that the freezing front progressed slower at the symmetric plane ($\theta=90^\circ$) than it did at the plane with $\theta=60.8^\circ$.

The transient distribution of local heat flux at the base of the droplet during freezing is illustrated in Figure 4.22. During freezing, the maximum heat flux occurred at somewhere between the center and the edge of the droplet. This trend was quite different from that of single phase shown in Figures 4.5 and 4.14, with the maximum heat flux occurring in the vicinity of the perimeter. Further inspection of the temperature distribution within the droplet (Figures 4.15, 4.16, 4.19, and 4.20) showed that the temperature at these nodes near the base of the droplet was driven to the cold plate temperature immediately after the freezing began. The local heat flux through the base of the droplet calculated by using Eq.(3.30) was influenced significantly by the freezing

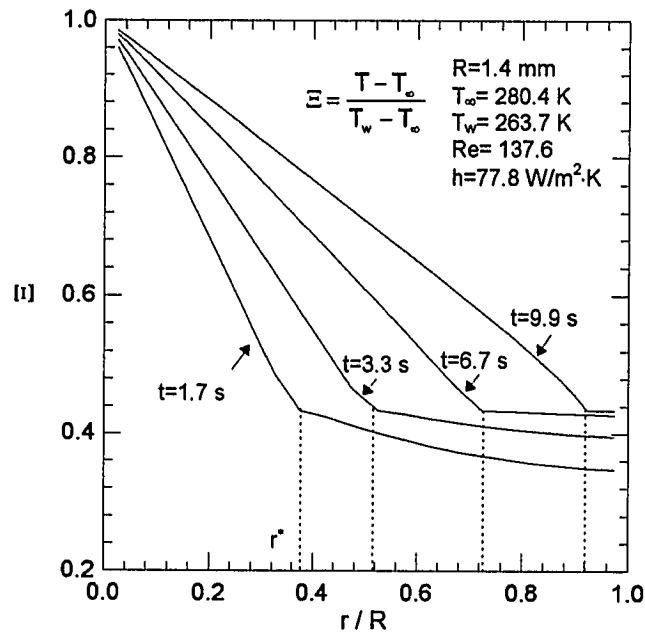


Figure 4.19 The temperature distribution inside a droplet ($\theta=60.8^\circ$).

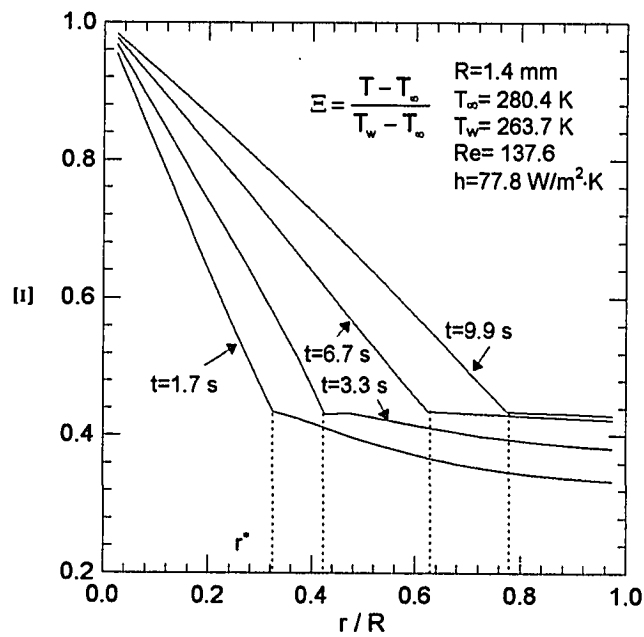


Figure 4.20 The temperature distribution at the symmetric plane of a droplet during freezing ($\theta=90^\circ$).

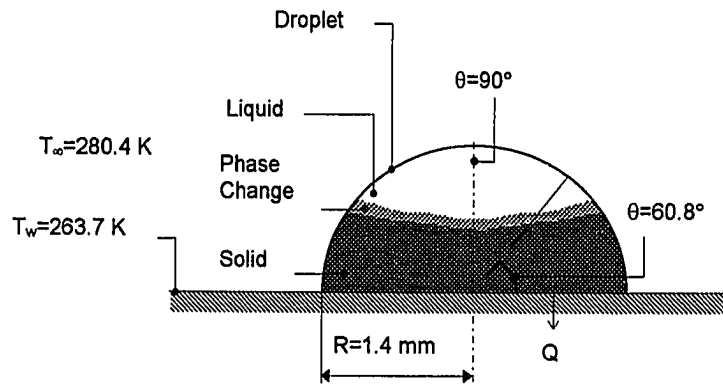


Figure 4.21 The positions inside a droplet at which the temperature distributions were plotted in Figures 4.19 and 4.20.

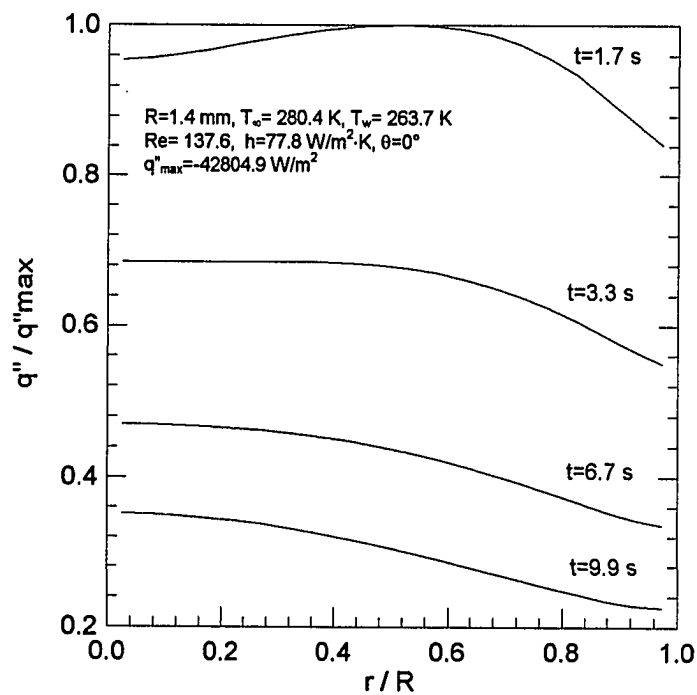


Figure 4.22 The heat flux through the base of a droplet during freezing ($\theta=0^\circ$).

of upper layer nodes. So that the maximum local heat flux through the base of a droplet changed its position all the time during freezing.

Figure 4.23 displays the temperature histories (or the cooling curves) at three positions of the droplet. During freezing, every node experienced three cooling processes: cooling in the liquid region, constant temperature in the phase change region, and cooling in the solid region. Eventually, the temperature at each node reached to a stable value and a steady-state temperature distribution could be obtained as shown earlier in Figures 4.11 and 4.12 for a solid droplet.

The mathematical model was also used to calculate the temperature field and heat transfer for a hemispherical droplet during freezing with the infinite air-side convection coefficient at the droplet surface, a.k.a., the limiting case. Figure 4.24 shows the angular temperature distribution for limiting case at $r/R=0.68$. At time $t=1.7$ s, the freezing front did not arrive to the spherical surface corresponding to $r/R=0.68$. It could be seen that the curve represented the temperature distribution in liquid region. With increasing time, the solid region grew gradually towards the edge of the droplet and intersected the spherical surface at $r/R=0.68$. During the freezing process, the nodal element temperature remained at freezing point for a finite time. Thus, the freezing front could be identified from the temperature distributions shown in Figure 4.24.

The radial temperature distribution was shown in Figure 4.25. One important phenomenon should be noted was that the droplet would never totally freeze to ice and three regions existed within the droplet all the time. The bends in the curves were caused by the differences of thermophysical properties between water and ice. Because

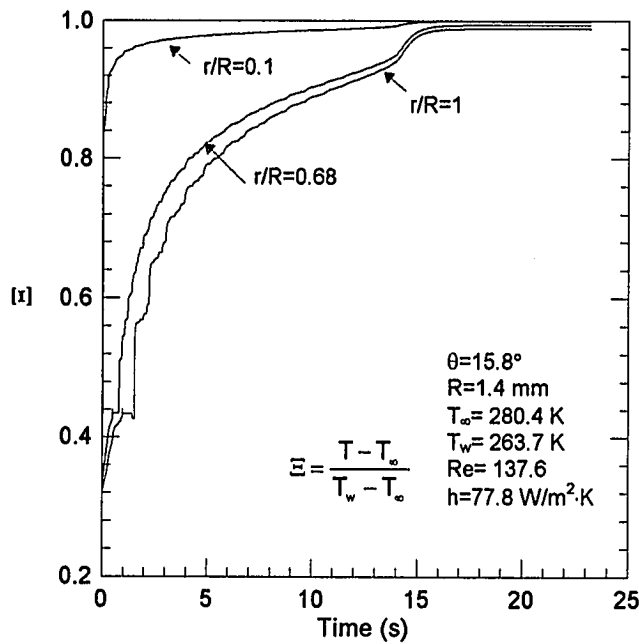


Figure 4.23 The temperature history of a node point of a droplet during freezing ($\theta=15.8^\circ$).

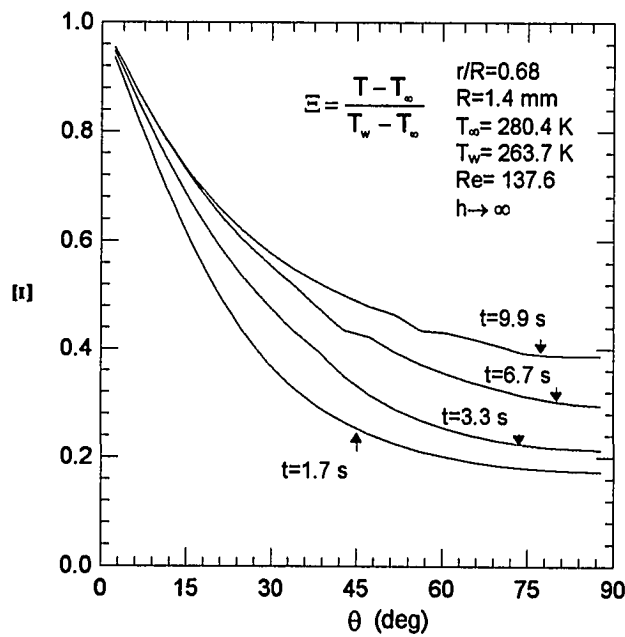


Figure 4.24 The angular temperature distribution inside a droplet during freezing ($h \rightarrow \infty$).

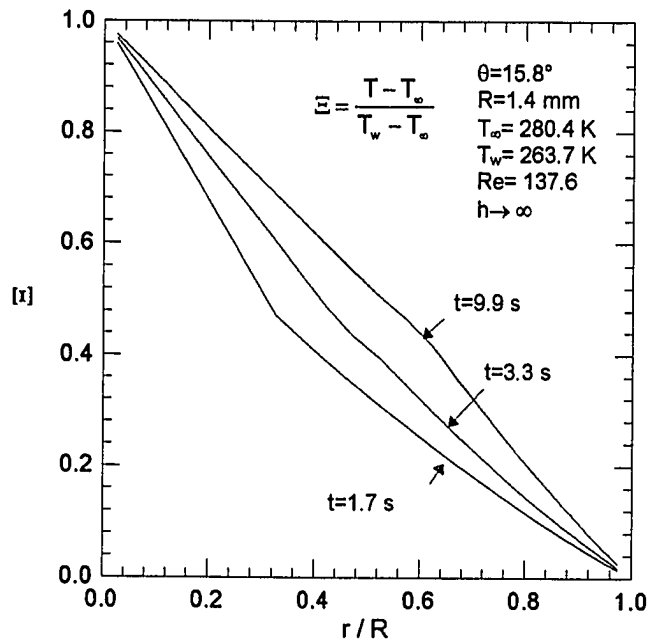


Figure 4.25 The radial temperature distribution ($h \rightarrow \infty$).

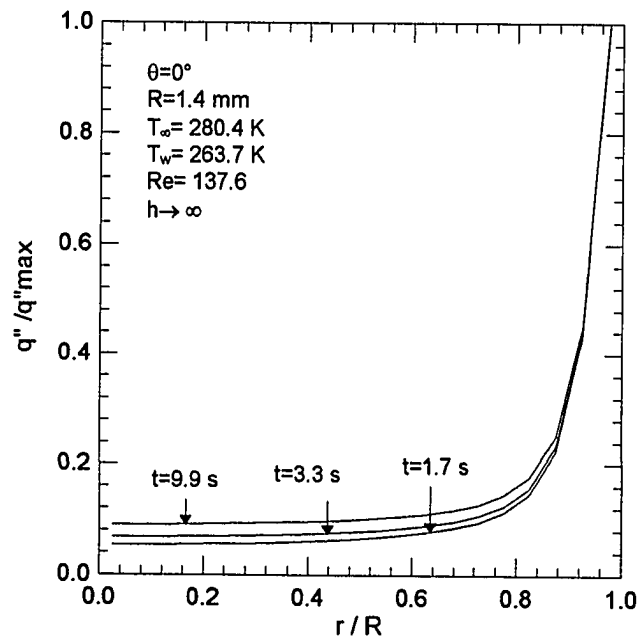
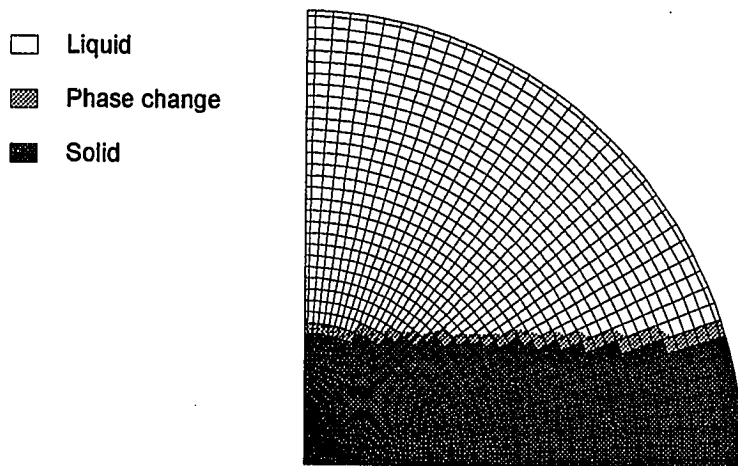


Figure 4.26 The heat flux through the base of a droplet during freezing ($h \rightarrow \infty$).

of the infinite air-side convection coefficient, the surface temperature was kept at the same temperature as that of the surrounding air. The local heat flux had a maximum value in the vicinity of the droplet perimeter, as shown in figure 4.26. Examination of the results revealed that about 77% of the heat transfer through a droplet ($Q = 0.197\text{W}$) came in around its perimeter ($0.8 < r/R < 1$).

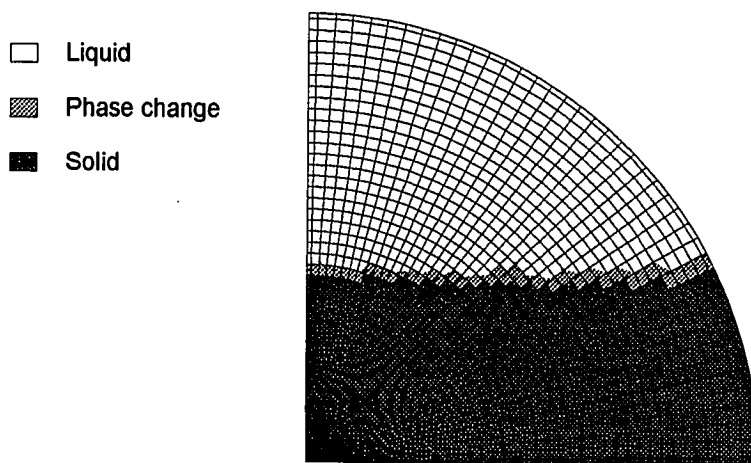
Numerical Simulation of the Freezing

Numerical simulation of the freezing process for a droplet with a 1.4 mm radius, ambient temperature of 7.2°C , plate surface temperature of -9.4°C , and air-side convection coefficient of $77.8 \text{ W/m}^2\cdot\text{K}$ are presented in Figures 4.27 through 4.35 in spectral plots. The simulations using a 40×40 spatial mesh and 0.03s time step employed three colors to represent different phase regions. These plots showed that the phase-change region was not a zero-thickness zone, but a region with finite width and concave shape. The transient fractions of solid could be determined by counting how many nodes had been frozen to ice with the mathematical model. For example, in Figure 4.30, the area fraction of solid was 87.9% at a time of 9.984s, which meant that 87.9% of the nodes had been either frozen to ice or were in the phase-change zone. When at $t=13.8 \text{ s}$, the area fraction of solid reached 100%, which meant that the droplet had been totally frozen to an ice hemisphere. From Figure 4.27 through 4.30, one important conclusion



$t = 1.656 \text{ s}$, $f = 37.6\%$

Figure 4.27 Three regions during freezing of a droplet sitting on a cold plate ($R=1.4$ mm, $T_\infty=280.4$ K, $T_w=263.7$ K, $Re=137.6$, $h=77.8$ W/m²·K, $t=1.656$ s).



$t = 3.32 \text{ s}$, $f = 52.3\%$

Figure 4.28 Three regions during freezing of a droplet sitting on a cold plate ($R=1.4$ mm, $T_\infty=280.4$ K, $T_w=263.7$ K, $Re=137.6$, $h=77.8$ W/m²·K, $t=3.32$ s).

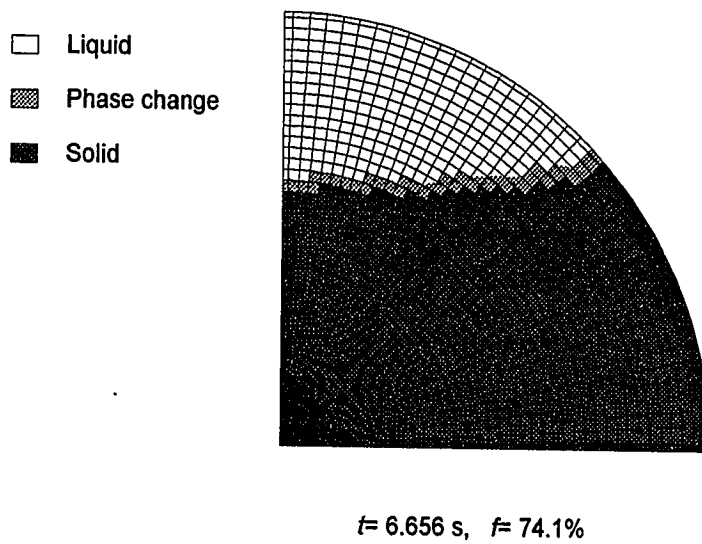


Figure 4.29 Three regions during freezing of a droplet sitting on a cold plate ($R=1.4$ mm, $T_\infty=280.4$ K, $T_w=263.7$ K, $Re=137.6$, $h=77.8$ W/m²·K, $t=6.656$ s).

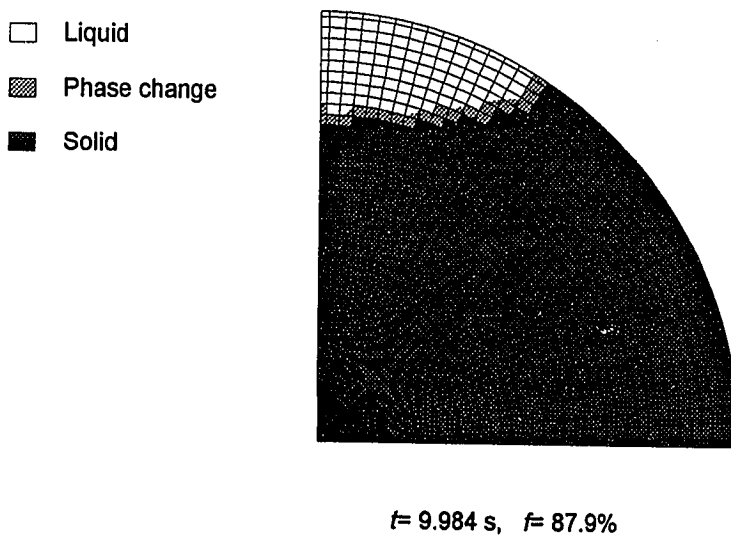
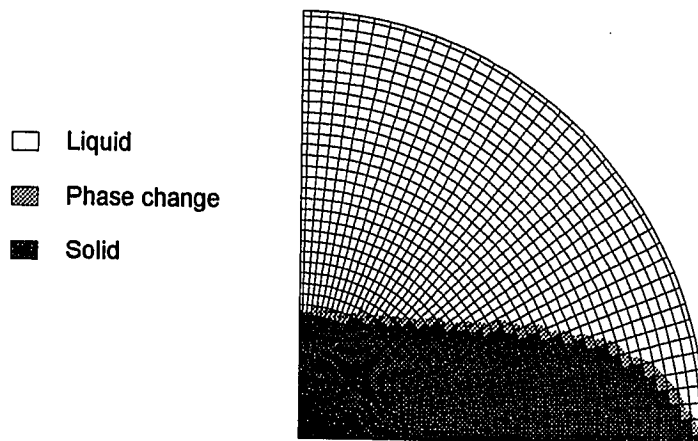
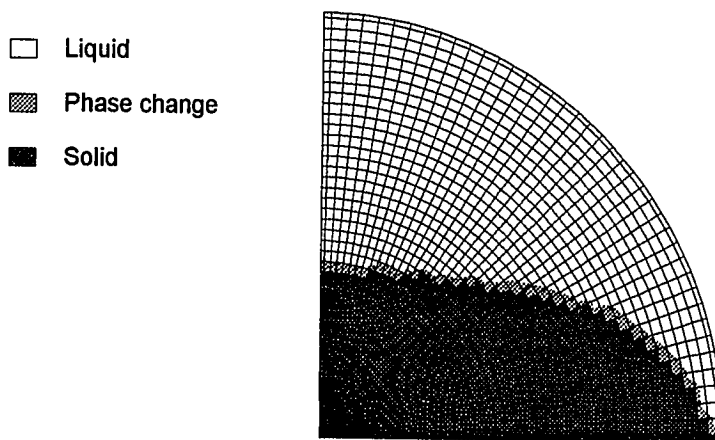


Figure 4.30 Three regions during freezing of a droplet sitting on a cold plate ($R=1.4$ mm, $T_\infty=280.4$ K, $T_w=263.7$ K, $Re=137.6$, $h=77.8$ W/m²·K, $t=9.984$ s).






$t = 1.656 \text{ s}, f = 31.8\%$

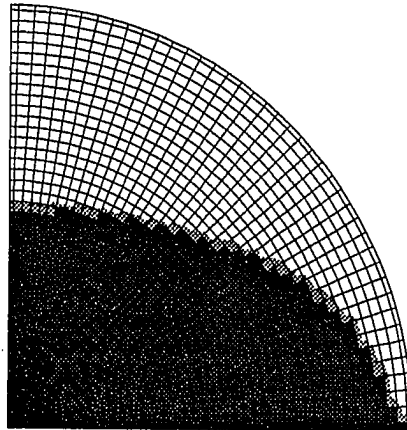
Figure 4.31 Three regions during freezing of a droplet sitting on a cold plate ($R=1.4 \text{ mm}$, $T_\infty=280.4 \text{ K}$, $T_w=263.7 \text{ K}$, $Re=137.6$, $h \rightarrow \infty$, $t=1.656 \text{ s}$).



$t = 3.32 \text{ s}, f = 41.3\%$




Figure 4.32 Three regions during freezing of a droplet sitting on a cold plate ($R=1.4 \text{ mm}$, $T_\infty=280.4 \text{ K}$, $T_w=263.7 \text{ K}$, $Re=137.6$, $h \rightarrow \infty$, $t=3.32 \text{ s}$).

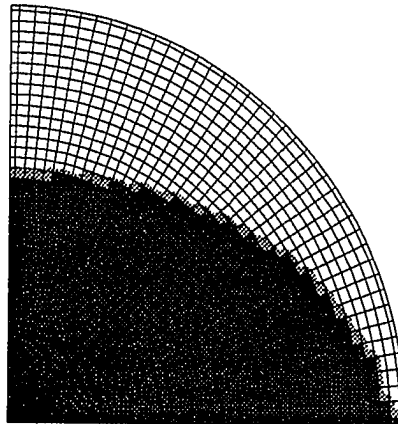
-  Liquid
-  Phase change
-  Solid



$t = 6.656 \text{ s}$, $f = 51.8\%$

Figure 4.33 Three regions during freezing of a droplet sitting on a cold plate ($R=1.4 \text{ mm}$, $T_\infty = 280.4 \text{ K}$, $T_w = 263.7 \text{ K}$, $Re = 137.6$, $h \rightarrow \infty$, $t=6.656 \text{ s}$).

-  Liquid
-  Phase change
-  Solid



$t = 9.984 \text{ s}$, $f = 58.0\%$

Figure 4.34 Three regions during freezing of a droplet sitting on a cold plate ($R=1.4 \text{ mm}$, $T_\infty = 280.4 \text{ K}$, $T_w = 263.7 \text{ K}$, $Re = 137.6$, $h \rightarrow \infty$, $t=9.984 \text{ s}$).

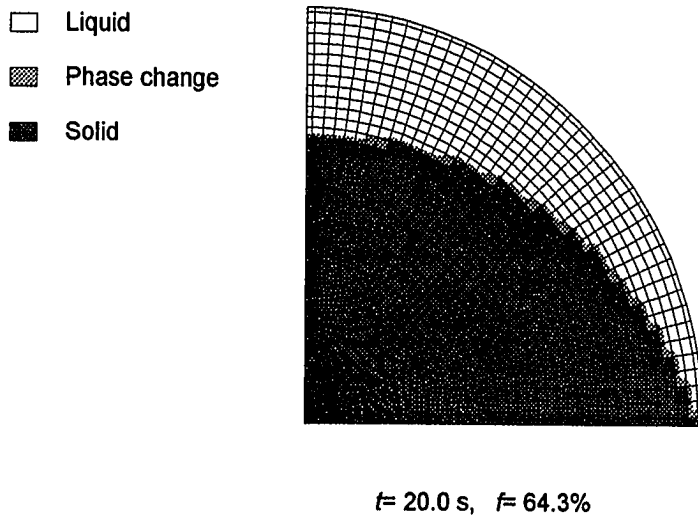


Figure 4.35 Three regions during freezing of a droplet sitting on a cold plate ($R=1.4$ mm, $T_\infty= 280.4$ K, $T_w= 263.7$ K, $Re= 137.6$, $h \rightarrow \infty$, $t=20.0$ s).

could also be drawn. The top node had the highest temperature in the computational domain and was always frozen last.

The numerical simulation for the limiting case, an infinite air-side convection coefficient at the droplet surface, was illustrated in Figures 4.31 through 4.35. The shape of the freezing front was different from that shown in Figures 4.27 through 4.30. Because the temperature at the droplet surface approached to ambient air temperature, the nodes at the droplet surface could never be frozen to ice. Figure 4.35 shows the steady-state phase regions at time $t=20$ s with three regions existing within a droplet. The temperature distributions are shown in Figures 4.25 and 4.26.

Model Predictions of the Velocity of Freezing Front

The local velocities of freezing front at different locations of a droplet, shown in Figure 4.36, were calculated by using Eq.(3.33) and presented in Figure 4.37. After ice nucleation, the freezing front moved at a high speed and then decreased with the buildup of ice at the base of the droplet. The local velocity of freezing front at position III was higher than that at position I, which were also shown in Figures 4.27 through 4.30. During freezing, the freezing front did not constantly move upward. There were some hesitations because of the energy transfer among nodes. As a result, the local velocity at some positions, i.e., position II, fluctuated.

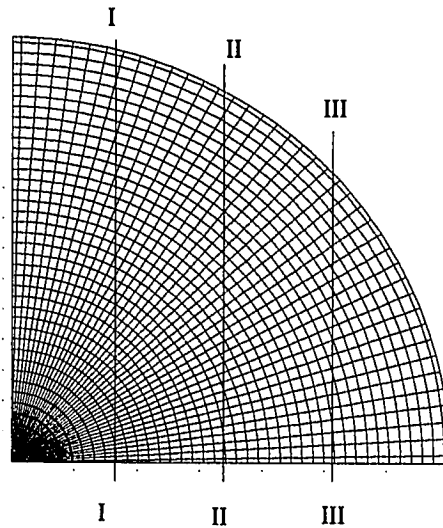


Figure 4.36 Three positions for the calculations of the freezing front.

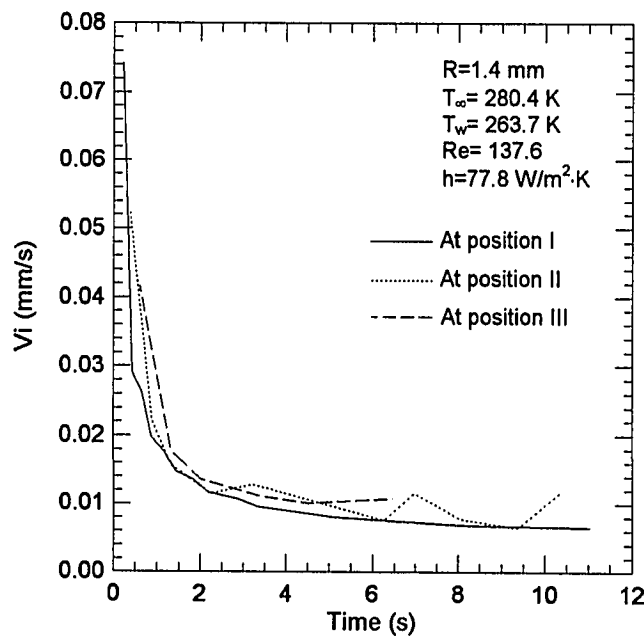


Figure 4.37 The freezing front velocities at three positions shown in Figure 4.36.

Mathematical Model Predictions for the Freezing Time

During the numerical iteration, the phase information of each nodal element was checked and updated at every time step. The time interval between the ice nucleation at the first node and the freezing of the last node was defined as the freezing time for a hemispherical droplet. In Figure 4.38, the freezing time was plotted as a function of radius when the ambient air and the plate surface were kept at certain psychrometric conditions. Freezing time increased with increasing the radius of a droplet. This result was reasonable because the basic concept told us that the latent heat released during a phase change was proportional to the volume of a droplet ($\propto R^3$), with the large droplet taking a long time to freeze to ice. On the other hand, the heat transfer rate through the base of the droplet was proportional to the base area of a droplet ($\propto R^2$), and the heat transfer through the surface of a droplet was roughly proportional to the circumference of a droplet ($\propto R$). The combination of these three aforementioned effects resulted in that the freezing time of a hemispherical droplet was roughly proportional to the square power of the radius of a droplet.

4.2 Grid Sensitivity and Program Validation

From the mathematical point of view, the development of the mathematical model could not be ended at this step. Even when the finite-difference equations have

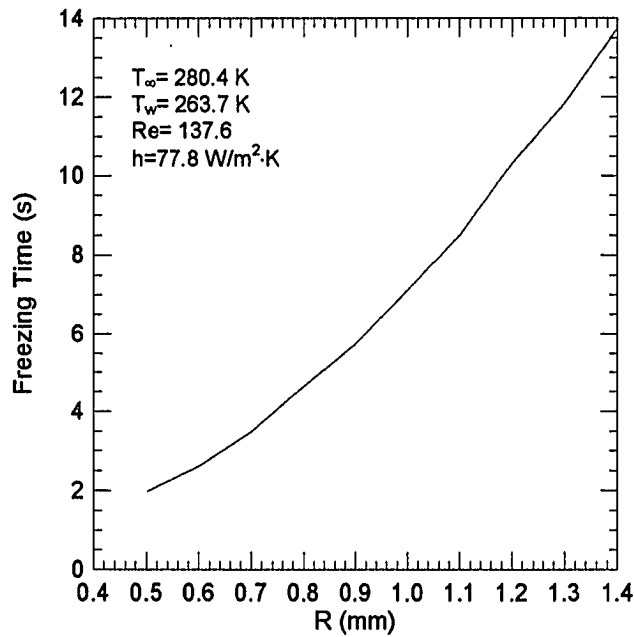


Figure 4.38 The predicted freezing time for a droplet sitting on a cold plate.

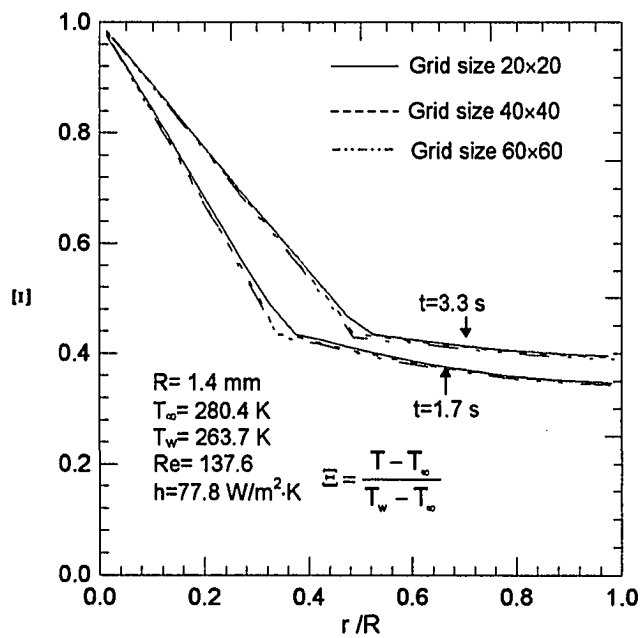


Figure 4.39 Transient temperature distributions in the radial direction predicted by the mathematical model for grid sizes.

been properly formulated and solved, the results might still represent a coarse approximation to the exact solution.

However, the finite-difference approximations could be made more accurate as the nodal network was refined. The cost is that the computer takes a longer CPU time to complete the iterations. A grid sensitivity study should be performed, whereby results obtained from a fine grid are compared with those obtained from a coarse grid. If the agreement is unsatisfactory, further grid refinements could be made until the computed results no longer depended on the choice of Δr , $\Delta \theta$, and Δt . Figure 4.39 shows the grid-independent test of the mathematical model. The test example was the calculation of the transient radial temperature distributions for a water droplet during freezing. The results using a 40×40 grid were plotted in the same graph as the values obtained using a 20×20 and a 60×60 grids. Comparison of local values of temperature for the three grid meshes revealed excellent agreement for liquid and solid regions. These locations at the phase change region appeared to agree less favorably for the 20×20 and the 40×40 grids (the maximum difference was 2.8 K), the discrepancies were mainly caused by the thickness of the phase-change region. The curves with the 40×40 grid was almost identical to that of 60×60 grid (the maximum difference was 0.2 K), therefore the 40×40 grid was chosen for using in this study.

Furthermore, various time steps were tested to determine the sensitivity of the mathematical model to time step. The test example was calculating the transient radial temperature distributions by using $\Delta t = 0.03$ s and $\Delta t = 0.008$ s. Results shown in Figure

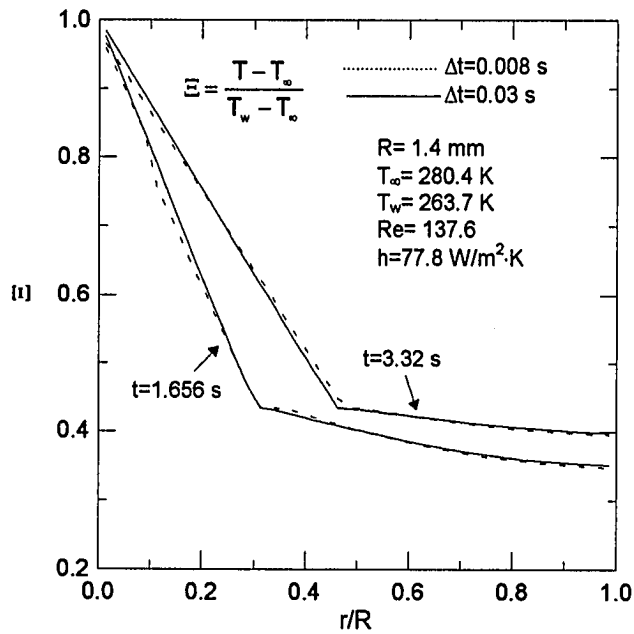


Figure 4.40 The sensitivity test of the mathematical model to time step.

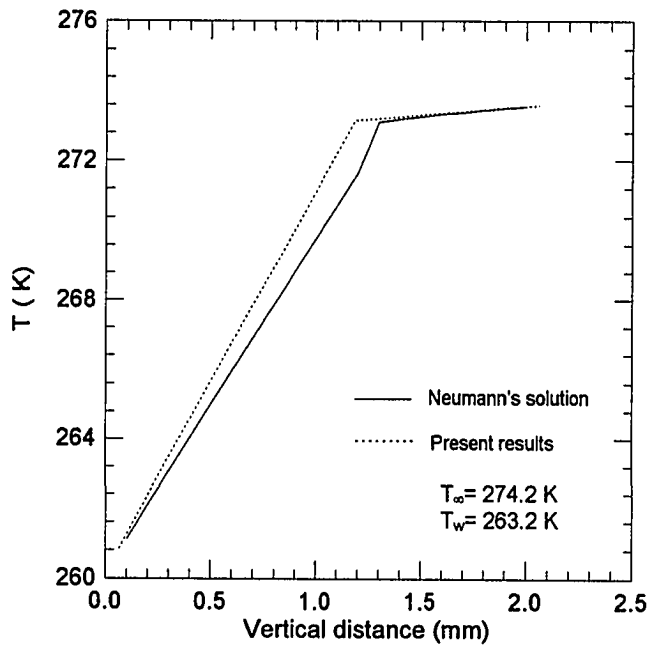


Figure 4.41 Comparison of present model results and Neumann's exact solution for Stefan problem.

4.40 indicated that the mathematical model was relatively insensitive to the time step (the maximum difference was 0.2 K).

All computations were performed with a personal computer (486DX2/66 MHz, 8 MB RAM) in which solution convergence, with the 40×40 spatial grid and 0.03 s time step, required 40 to 50 minutes.

Next, the mathematical model was used to solve some phase-change examples, and the results were compared with previously published results obtained by different methods. Because the exact solutions on the temperature field and heat transfer during freezing of a hemispherical droplet was not applicable, the model was tested by applying it to solve some simple versions of the problems.

The first test problem was the classical Stefan problem (Carslaw and Jaeger, 1959). In this problem, a material occupied the semi-infinite region was initially in the liquid phase at a constant temperature $T_o=0^\circ\text{C}$. At time $t=0$ the base temperature was instantaneously lowered and maintained at $T_w=-10^\circ\text{C}$. This would cause a layer of solid to be formed adjacent to the base surface and as time increased this layer would grow into the liquid. Figure 4.41 shows that the temperature distribution in the solid phase and liquid phase obtained by the model conformed to Neumann's solution very well with a maximum deviation 1.01 K.

The second test case was the calculation of the steady-state one-dimensional temperature distribution within a spherical annular shell, with an inner radius of 0.9 mm and 0.5 mm thick, as shown in Figure 4.42. The inner and outer surface temperatures were maintained at 240 K and 260 K, respectively. The temperature distribution could

be determined by solving conduction equation and applying boundary conditions. It had the form (Incropera and DeWitt, 1990)

$$T - T_1 = (T_2 - T_1) \frac{r_1 r_2}{(r_1 - r_2)} \left(\frac{1}{r} - \frac{1}{r_1} \right) \quad (4.1)$$

The comparison of the analytical solution and the model results was plotted in Figure 4.43. The present model results agreed well with the analytical solution with maximum difference less than 1%.

The third test problem was calculating the central temperature history at the center of a sphere. As an example, a solid sphere initially at T_o and with its surface $r=R$ suddenly changed to, and maintained at, T_1 for $t>0$ was considered in the problem. In this case the general and central temperature history were found to be (Schneider, 1955):

$$\frac{T - T_1}{T_o - T_1} = \frac{2}{\pi} \left(\frac{r}{R} \right) \sum_{m=1}^{\infty} \frac{(-1)^{m+1}}{m} e^{-(m\pi)^2 Fo} \sin(m\pi \frac{r}{R}) \quad (4.2)$$

$$\frac{T_c - T_1}{T_o - T_1} = 2 \sum_{m=1}^{\infty} (-1)^{m+1} e^{-(m\pi)^2 Fo} \quad (4.3)$$

Figure 4.44 shows the comparison between the model results and exact solution. It was seen that the agreement was very good with maximum difference less than 1%.

Finally, a problem of other geometries reported in a pervious published paper (Neilson and Incropera, 1990) was solved by the mathematical model. It was the solidification of an aqueous Na_2CO_3 solution in a cylindrical annulus. Phase change was induced on an isothermal ($T_s = -20^\circ\text{C}$), horizontal cylinder ($R_i = 12.7$ mm), while a well-insulated condition was maintained at the outer cylinder ($R_o = 50.8$ mm). The temperature history of a nodal element ($r = 14.3$ mm) was compared with the results of Neilson and

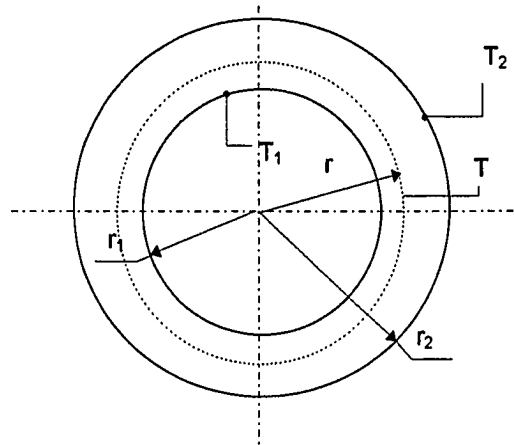


Figure 4.42 A hollow sphere with isothermal surface conditions.

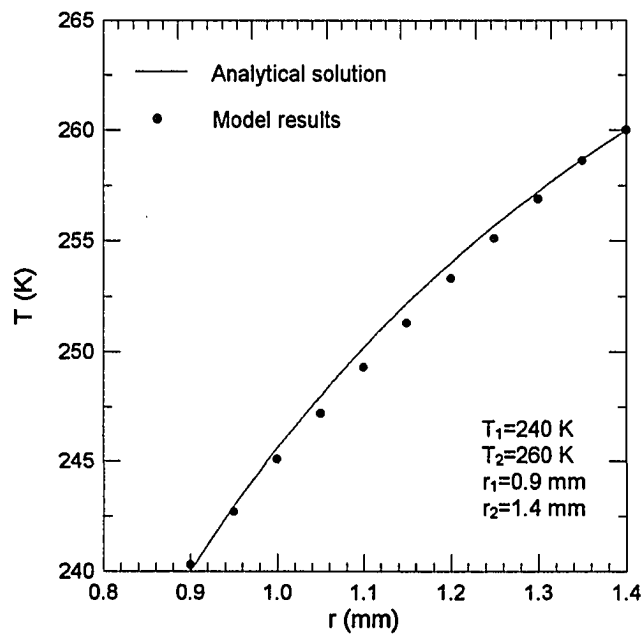


Figure 4.43 The comparison of analytical solution and model results.

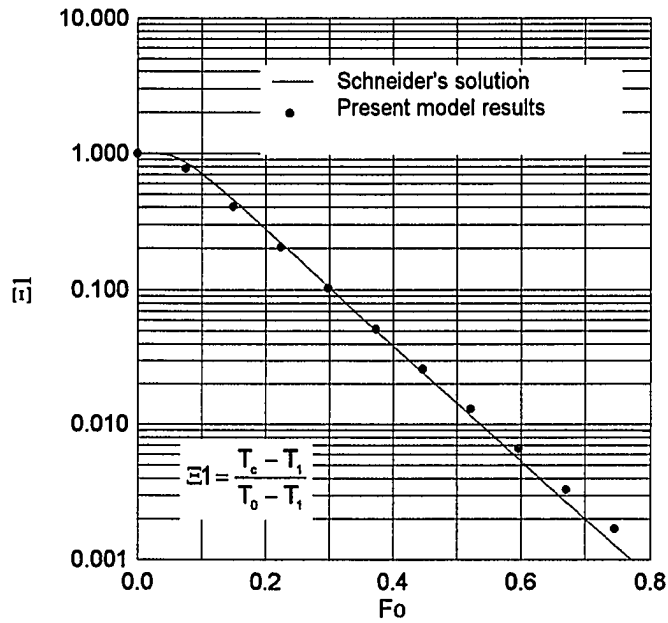


Figure 4.44 Central temperature history: Comparison between model results and exact solution

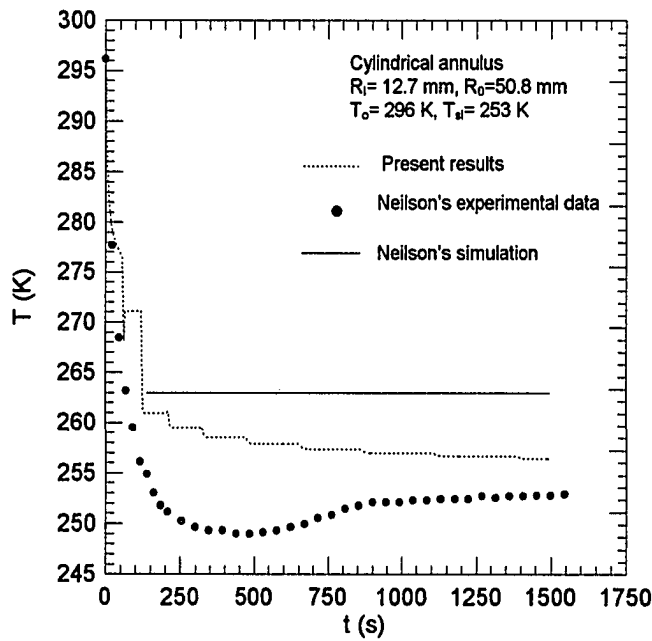


Figure 4.45 Comparison of present model results with Neilson's simulation and experimental data.

Incropera shown in Figure 4.45. It could be seen that the present mathematical model agreed better with the experimental temperature history at a point during the freezing process than Neilson and Incropera's simulation.

4.3 Summary

The mathematical model developed here was able to solve a transient two-dimensional temperature distribution for a phase change problem in spherical coordinates. And, the algorithm was adaptable to different geometries and boundaries (Figures 4.41 and 4.45). Furthermore, this computational strategy could be extended to the other forms of phase change problems.

The control volume method was applied to model the freezing of a water droplet resting on a cold metal plate. The transient temperature distribution, temperature history curve, heat transfer through the surface and the base of a water droplet, freezing front velocity, and the position of freezing front could be predicted. Comparisons had been made between the analytical solution and model results predicted by the present model with a good agreement, indicating that the mathematical model could properly simulate the freezing process of a water hemisphere. Combining heat transfer of a single droplet with dropsize distribution, overall heat transfer through a surface could be calculated.

The edge of a droplet played a particular important role in heat transfer for the problem illustrated in Figures 4.3 and 4.6. The vicinity of the droplet perimeter acted as a ring-heat-sink, which transferred heat from ambient air into the cold plate. The top of

a droplet exerted a comparatively high heat-transfer resistance. The droplet became a mechanism for supplying a thin cooled liquid perimeter onto which the vapor could readily condense.

The occurrence of condensation on a cold plate first appears as very small droplets at the sites of these nuclei. Then droplets grow through both continuous condensation and coalesce with neighboring droplets. A conclusion of engineering importance emerged from examination of the temperature distribution at the surface of the droplet (Figure 4.4). Because of the low temperature and high heat transfer rates around the vicinity of the droplet perimeter (Figures 4.2 and 4.5), the formation of a new liquid embryo was most likely to occur right on this area. If the vapor in air condensed at the surface of a droplet, the low-surface-energy liquid surface was well wetted by the liquid condensate, producing film condensation instead of dropwise condensation. The expansion of a droplet perimeter intended to connect the droplet with all of the neighboring droplets and formed a thin film among condensate droplets on a cold metal plate. When condensation on a cold metal plate reached this stage, the surface coatings used to promote dropwise condensation were inactivated. Later continuous condensation was filmwise on droplet surface and film sublayer. This phenomenon had been observed in present experiments.

When droplets became large enough, they were generally removed from the surface by the action of gravity or drag forces resulting from the motion of the surrounding air. As the drops rolled or fell from the surface, they merged with droplets in their path, effectively sweeping the surface clean of droplets. New droplets then

began to grow on the freshly exposed surface. The sweeping and renewal of the droplet process were responsible for the high heat transfer coefficients associated with dropwise condensation. In fact, the aforementioned drainage of condensate was just the idealized circumstance. Because of the complicated surface configuration of a heat exchanger operating on actual outdoor environment, only could large droplets fall from the surface. However, drainage condensate droplets played a major role in the design of heat exchanger when the dropwise condensation was used to enhance heat transfer.

The next important conclusion had to do with the microscopic mechanism of frost formation as the dropwise condensation on a cold plate. The temperature distribution (Figure 4.12) shows that the perimeter ring area is frozen to ice first, while the temperature at the top of a droplet may be higher than the freezing temperature. The crystal growth should start with the vicinity of the droplet perimeter, forming a thin ice layer on the plate and insulating the plate surface from contacting the ambient air. If the surface temperature of the ice layer was still lower than the dew point of the ambient air, the film condensation would continue at the top of the ice layer.

Although this mathematical model produced stable, physically reasonable temperature field during the freezing of a water droplet, it slightly underpredicted heat transfer by neglecting the effect of internal circulation. Further research is needed to find a significant indicator for presence of convection heat transfer. More experimental data are needed to correlate local convection transfer coefficient at the surface of a droplet.

CHAPTER V

EXPERIMENTAL SETUP

5.1 Test Setup

To study the microscopic mechanisms of dropwise condensation, frost formation, and freezing of the water droplet, an experimental setup was constructed by a previous graduate student (Bryant, 1995) at the Energy Systems Laboratory of Texas A&M University. As shown in Image 5.1, the test section was connected with a closed duct loop. The fully developed, conditioned air stream driven by a blower passed through the test section. A micromanipulator, a CCD camera, and a stereo microscope were mounted on the test bench.

Figure 5.1 shows the layout of the experimental setup and the locations of its elements. The test loop was constructed of one-half inch thick insulating ductwork. A chiller supplied glycol-water solution to the primary cooling heat exchanger and to the secondary cooling/dehumidification heat exchanger. A 500 Watt resistance heater located downstream of the fan section was used as the final air temperature control element. This arrangement allowed air conditions to be controlled to $\pm 0.3^{\circ}\text{C}$ and varied over a range of 1°C to 35°C . Moisture content was controlled through the use of the resistance heater and/or steam added from a small boiler. This arrangement allowed control of the relative humidity from 20 to 90%.

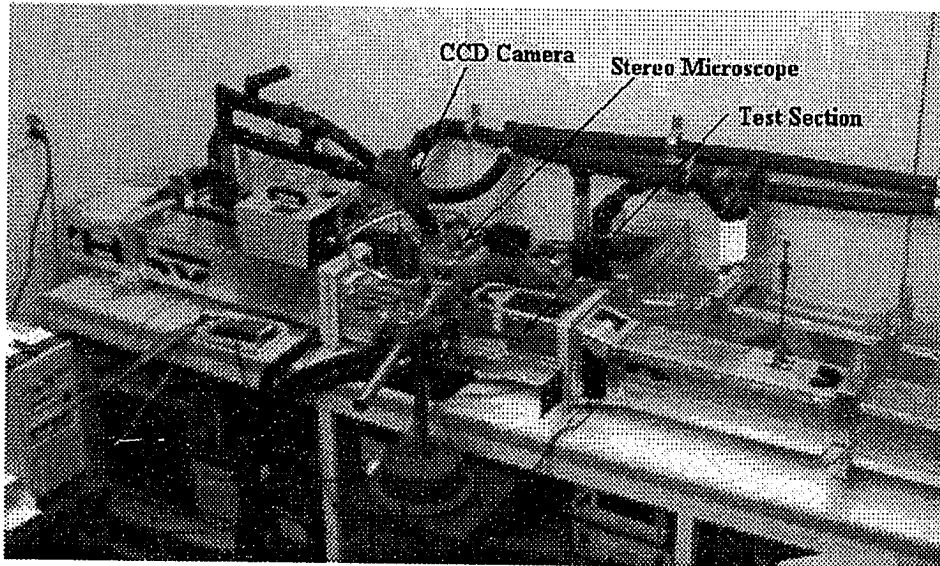
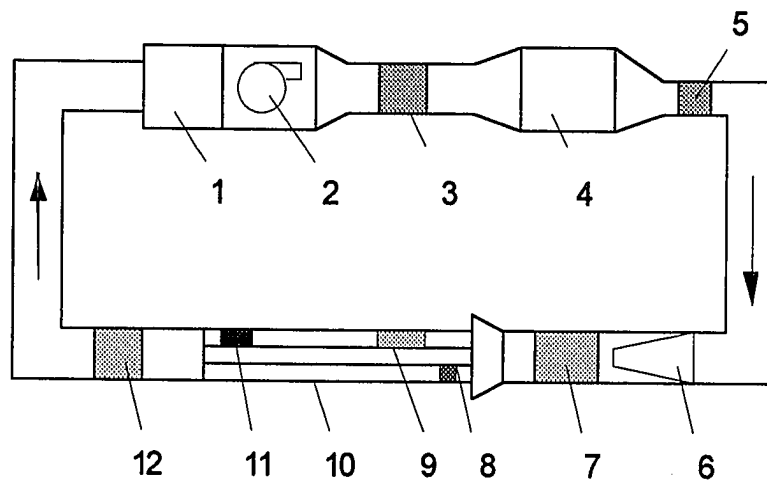


Image 5.1 The experimental setup



1. Aqueous Glycol cooler
2. Blower
3. Humilification section
4. Aqueous Glycol cooler
5. Resistance heater
6. Converging section
7. Upstream turbulent and flow development mixing section
8. Flow rate controller
9. Test section
10. Bypass
11. Velocity control
12. Downstream mixing section

Figure 5.1 The schematic of experimental setup

The velocity was controlled with a damper in the bypass duct (part #8 in Figure 5.1) and flow area adjustment device in the test duct (part #11 in Figure 5.1).

A schematic of the 15 mm × 60 mm Plexiglas test channel is shown in Figure 5.2. The test channel was constructed to allow viewing of the dropwise condensation, condensate droplets undergoing freezing, and frost layer growth without disturbing the process. The test channel was enclosed by an annulus that ensured a uniform temperature profile enter the point where the test cell was mounted. In addition, a bypass duct with a damper was constructed to maintain proper air temperature and moisture content in the primary duct.

Figure 5.3 illustrates some features of the test cell. Heat was released at the surface of copper plate by condensation or freezing of water droplets and supplied by the air flow over the copper plate. Then it was conducted vertically downward through a thermoelectric heating and cooling module (TEC) below a 30 mm × 30 mm copper surface plate and a glycol-water chiller at the bottom of TEC. A thin-film heat flux gauge was mounted between the TEC and copper plate and allowed the measurement of heat flux perpendicular to the copper plate. The TEC was capable of cooling the copper plate to -20°C and heating the plate to 120°C.

Distilled water is transparent, allowing for optical and photographic observation of the freezing. Its properties were well established and thus facilitate the proper non-dimensionalization which is necessary in generalizing the results.

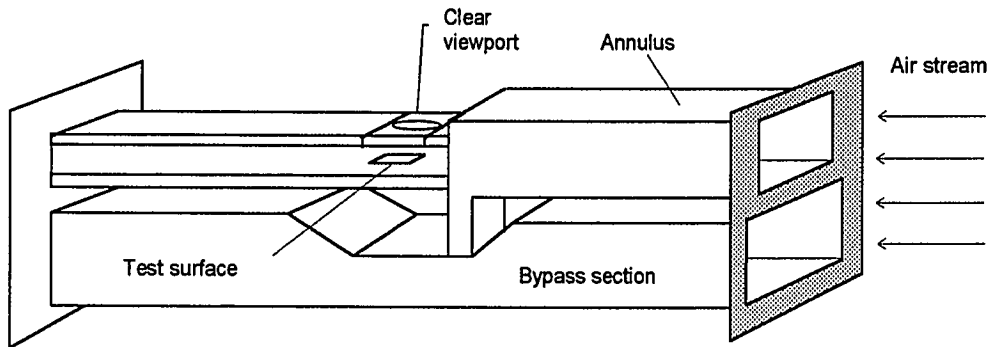


Figure 5.2 The sketch of the test channel

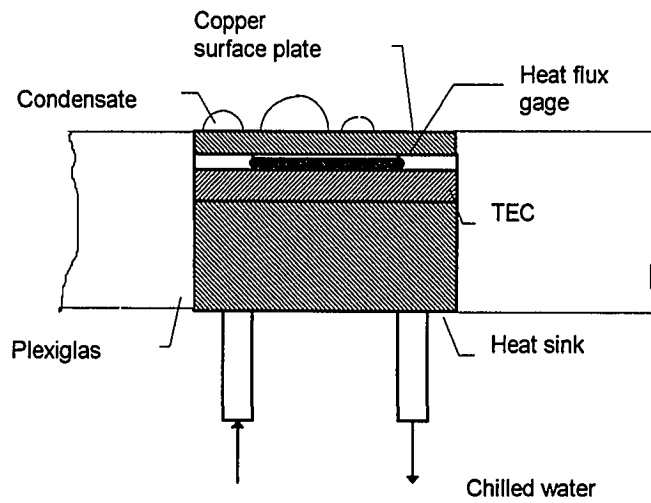


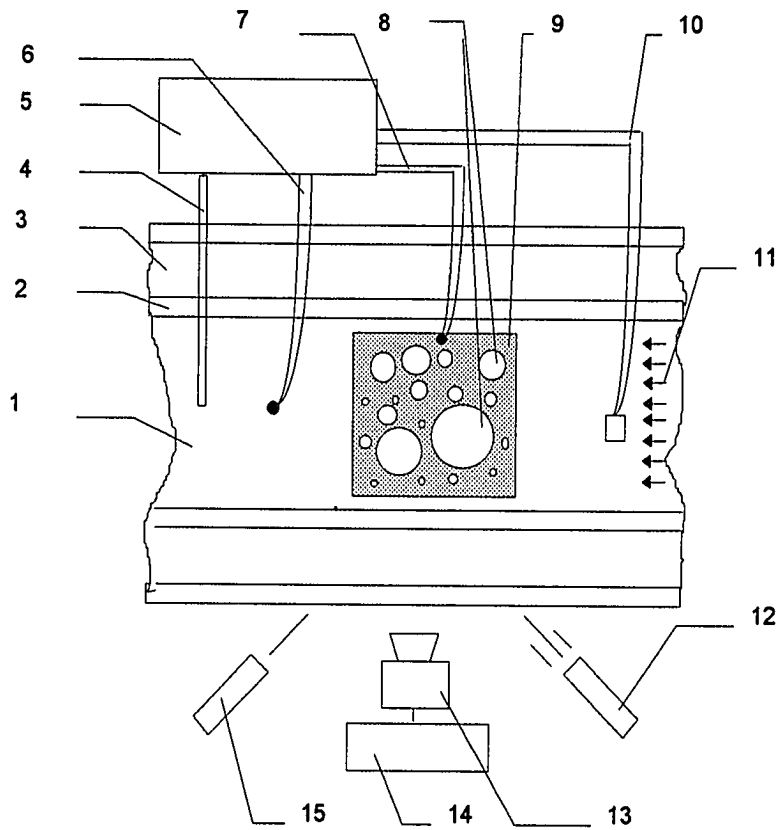
Figure 5.3 A cross-section of the test cell

5.2 Instrumentation

A data acquisition system and image recording system were employed in the study of frost formation. There were six measuring devices presented in the experimental setup shown in Figure 5.4: temperature, velocity, heat flux, relative humidity, size, and time. Each is discussed below.

Temperature Measurement

Three thermocouples constructed from 32 gauge (diameter= 0.203 mm) copper-constantan wires were inserted into the test loop to measure air temperature at different locations: upstream, at, and downstream of the test cell. One thermocouple constructed from 37 gauge (diameter= 0.11 mm) copper-constantan wires was inserted into a droplet to measure the temperature inside the droplet. These thermocouples were connected individually to a data acquisition system named WorkBench PC 2.0 (Strawberry Tree Incorporated, 1991) whose output was directly in °F or °C. The accuracy specification of the thermocouple was at $\pm 0.5^{\circ}\text{C}$ or 0.4% of the temperature guaranteed by the manufacturers. If the digitizing error resulting from the A/D conversion process was taken into account, the uncertainty of temperature measurement was estimated at $\pm 1^{\circ}\text{C}$.



- 1, Test section
- 2, Plexiglas rectangular cross section annular pipe
- 3, Guard area
- 4, Anemometer
- 5, Data acquisition system
- 6, Thermocouple
- 7, Thermocouple
- 8, Water droplets
- 9, Copper plate
- 10, Relative humidity sensor
- 11, Moist air stream
- 12, Conventional light source
- 13, CCD camera
- 14, Image recording system
- 15, Laser beam

Fig. 5.4 Schematic diagram of experimental setup

Velocity Measurement

The air velocity was measured with a hot-wire anemometer. Because the thermal mass of the sensing element was extremely small, its response to flow velocity was rapid. A standard Pitot-static tube was utilized to calibrate the anemometer and then the output voltage was converted to velocity by following expression:

$$V = \frac{0.3048}{60} (52.15 + 14.138 \cdot \ln(u) + 114.795 \cdot u - 1.577 \cdot u^2) \quad (4.1)$$

where u is in mV and V is in m/s.

The specification of the probe was 2.5% of reading or ± 0.01 m/s. The uncertainty of the velocity measurement was estimated 5% of reading.

Heat Flux Measurement

A thin-film heat flux gauge was mounted between the surfaces of the TEC and the copper plate and used to measure the average heat flux through the copper plate, as shown in Figure 5.3. The specification of the thin-film gauge was 2.5% of the reading. The estimated uncertainty of the heat flux measurement was 5% of the full range.

Relative Humidity

The relative humidity was measured by electrical conductivity humidity sensor, which has a fast response to change in humidity. The specification of the sensor was $\pm 2\%$ guaranteed by the manufacturer. The uncertainty of the relative humidity measurement was estimated at $\pm 5\%$.

Data Acquisition System

A continuous record of the plate surface temperature, air temperature, relative humidity, heat flux, and air flow velocity was obtained by a data acquisition system called WorkBench PC 2.0 (Strawberry Tree Incorporated, 1991). All of the measured values could be displayed instantaneously on the monitor, which allowed the observation of any transducer and/or acquisition system malfunctions.

Image Acquisition System

A stereo microscope was mounted above the test section to view the microscopic stages of the phase change process. Attached to the eyepiece of the microscope was a high resolution charge coupled device (CCD) camera. The combination of the camera and microscope provided magnifications of 100 to 280 \times with the ability to resolve liquid droplets as small as five microns in diameter. A laser beam was employed to highlight the copper

plate and the freezing front. Time-lapse motion pictures of the moving freezing front were taken at 30 frames every 1 second. The images from the microscope system were either recorded on a videotape or acquired by a digital image capture board installed in a micro-computer. These images were then analyzed with measurement imaging software called MOCHA for droplet size, micro-thermocouple placement, and freezing time.

5.3 Experimental Procedure

The experimental procedure consisted of forming droplets onto the copper plate, inserting a micro-thermocouple into the droplet, measuring and recording the pertinent variables, recording the images on videotape or installing in a micro-computer, and analyzing the measured data and images.

Complete details of the apparatus and test procedure are given as follow.

Freezing Time

Transient runs were performed while temperature, velocity, and relative humidity within the test channel were maintained at steady state values. These runs were used to provide data for comparison of freezing time predicted by the mathematical model. Droplets were made by using a hypodermic syringe and place the droplets onto a dry area on the copper surface. By adjusting the light source and focusing the camera, the target droplet and its adjacent droplets could be clearly displayed on the screen. The

metal surface was maintained at a temperature slightly higher than the dew point of the air flow. This would minimize the humidity ratio difference between the droplet surface and the air flow and reduce the evaporation and condensation at the droplet surface. While the camera was continuously tracing the target droplet, the metal surface temperature was suddenly lowered by the thermoelectric module until expected condition was reached. The first ice nucleation could be seen at a few points. Furthermore, the neighbor droplets of the target droplet began freezing, the data and image acquisition systems were activated to continuously record images and thermal parameters until the target droplet was frozen to ice. The motion of the freezing front was continuous recorded on a video tape. Thus, the freezing time of a droplet could be obtained by analyzing the video tape.

The thermoelectric heating and cooling module was designed to permit a rapid change in heat flux (both cooling and heating) below the copper plate. Thus the phase change process could be caused to happen in either freezing or melting, which made it possible to repeat the freezing process several times for a droplet.

Temperature Field

One of the objectives of this investigation was to determine the temperature field in condensate droplets resulting from conditions imposed on its boundaries. Two experiments were conducted : steady state temperature distribution inside a droplet and temperature history at a certain position in a droplet during freezing.

A micromanipulator was used to insert a very thin thermocouple into a droplet and to move the thermocouple up and down in a vertical direction. The size of a droplet, the position of the thermocouple junction, and the traverse distance could be recorded on a videotape and then measured with image processing software. The temperatures could be plotted on the monitor and checked if the steady state has been reached.

To measure the temperature history, or cooling curve, at a position inside a droplet, the thermocouple junction was placed into a droplet using the micromanipulator. At first, the plate surface temperature was kept at a temperature higher than the freezing point of water. Then the surface temperature was suddenly dropped to a value below the freezing point of water. The droplet began to cool and after a period of subcooling the liquid would nucleate to ice. When the droplet was totally frozen to ice, it continued to cool until reached to a steady state.

Freezing Front Velocity

The freezing experiments provided evidence about the freezing front and gave immediate insight into the nature of the transport processes in the phase change region.

A good arrangement of the conventional light and laser beam could highlight the freezing front. At the moment of ice nucleation, there was a sudden change of the color of a droplet, but the freezing front could still be identified. Images from the CCD camera were recorded on a videotape at a record rate of 30 frames/s. All measurements

on the videotape then were accurately analyzed with MOCHA. The length and area were calibrated by means of the image of a standard vernier caliper.

Experimental runs were made at different test conditions with distilled water. The runs differed in the air-to-plate temperature difference, the radius of the droplet, the relative humidity, and the velocity of the air stream.

Air-Side Convection Coefficient

The air-side convection coefficient at the surface of a droplet affected the calculation of heat transfer and temperature field inside a droplet. In this study, no experiment was conducted on the air-side convection coefficient for an individual droplet surface. The average convection coefficient for a metal surface covered with many condensate droplets was measured under different test conditions. During a test the air temperature, the surface temperature, and the heat flux through the metal plate were measured under the of steady state and steady flow within the test loop. The average air-side convection coefficient could be calculated according to the Newton's cooling law, which would be elaborated in Chapter VI.

CHAPTER VI

EXPERIMENTAL RESULTS AND DATA REDUCTION

The proposed experimental work concentrated on the measurement of the freezing of hemispherical droplets on a cold metal surface. Specific measurements included:

- **Droplet freezing time.** The digital imaging system was used to record the freezing process and time of hemispherical droplets under a range of test conditions.
- **Shape and position of the freezing front.** A laser beam was used to highlight the phase change zone. The shapes and the positions of the freezing front as the droplet changed phases were recorded with the digital imaging system. By analyzing the consecutive images of the freezing front, the freezing rate and direction were obtained.
- **Temperature field in the droplet.** Thermocouples were used to measure the steady state temperature distributions and the transient cooling curves in droplets during freezing.
- **Average air-side convection coefficient.** Conventional heat transfer techniques were used to estimate the average air-side convection coefficient for a surface covered with condensate droplets.

In the test setup, the air temperature was varied from 0 to 35°C while the air relative humidity was controlled from 15 to 70%, which represented environmental conditions relevant to heat pumps. The temperature and relative humidity of the air

could be maintained at constant within $\pm 0.2^{\circ}\text{C}$ and $\pm 3\%$, respectively. The surface temperature of the copper plate could be varied with a thermoelectric heating and cooling module from -15 to 40°C . The surface temperature variations during an experiment were $\pm 0.5^{\circ}\text{C}$. The air velocity could be changed from 0.2 to 3.5 m/s (39 to 689 ft/min.). Typical air velocity variations through the test section were within ± 0.03 m/s (± 5.9 ft/min). The size of the hemispherical droplet was varied by using different sizes of hypodermic syringes. The radius of droplets ranged from 0.5 to 1.5 mm. The CCD camera was used to measure the contact angles of the droplets and ensure that they were approximately 90° .

A test matrix was developed to perform the proposed work. The experimental results obtained from the aforementioned tests were presented in tabular form (see Appendix A) with uncertainty values at a 95% confidence level and in graphic forms. Two correlation equations relating droplet freezing time and air-side convection coefficient were developed from experimental data and given much more compact representations of the data than tabular listings or even graphics.

6.1 Dimensional Analysis

Dimensional analysis is an important tool that can help identifying the important physical variables affecting a process. It can be used to extend the results of a few experiments to a wide variety of other conditions, geometries, and substances.

Over the years, several hundred different dimensionless groups had been identified (Omega Engineering, 1994). Unfortunately, none of them could be applied directly to the freezing of hemispherical droplets, which depended on geometric, flow, and ambient psychrometric variables. There was a need to identify non-dimensional groups that could provide special physical interpretations to the freezing process on a cold metal plate.

During the freezing of a hemispherical droplet, the freezing time could vary with many system parameters: body size D , surface temperature T_w , ambient temperature T_∞ , surrounding air velocity V , and fluid properties. If this variation was expressed functionally as:

$$t = f(T_\infty - T_w, D, V, \mu_\infty, h, k_\infty, \rho_\infty, h_{sf}) \quad (6.1)$$

This was a list of nine variables. They could all be expressed in terms of four primary dimensions: mass, length, time, and temperature. Then, by the Buckingham Pi theorem, Eq.(5.1) was expected to be rewritten as a function of several dimensionless variables. The particular variables obtained could differ according to the manner of grouping chosen. The following functional list was a proposed grouping:

$$\frac{\alpha_L t}{D^2} \cdot \frac{VD}{\alpha_L} = f \left[\frac{k_\infty(T_\infty - T_w)}{\rho_\infty V^3 D}, \frac{\mu_\infty}{\rho_\infty VD}, \frac{k_s(T_f - T_w)}{h_{sf}} \right] \quad (6.2)$$

or

$$(Fo \cdot Pe)_L = f(Am_\infty, Re_\infty, Ste_L) \quad (6.3)$$

In this dimensionless list it was recognized the Stefan number Ste , the Reynolds number Re , the Fourier number Fo , and the Peclet number Pe . The subscript on dimensionless number denoted the substance being used, either water or air. The

characteristic length in Eq.(6.3) was the diameter of a hemispherical droplet. The new parameters, Am , was defined as the ratio of heat flux through the body by conduction from the cold plate to the kinetic energy flux of ambient fluid flow. There were several important implications of this dimensionless number. For small Am , the kinetic energy flux of the ambient flow was sufficiently large relative to the heat flux through the body by conduction. Hence the surface temperature of the droplet would tend to be close to the ambient temperature. With increasing Am , the kinetic energy effect became progressively less important relative to conduction effects, and the temperature of the droplet would begin to approach the plate temperature.

Introduction of the dimensionless freezing time defined as

$$\tau = (Fo \cdot Pe)_L \quad (6.4)$$

permitted scaling of the product of the Fourier number and the Peclet number for the freezing of hemispherical droplet on a cold metal plate. The physical interpretation of τ followed its definition as a ratio of the distance covered by the ambient fluid during time t to the body size D . τ provided a measure of relative magnitude of droplet size and the speed of the ambient flow and stood for the dimensionless freezing time. A large τ meant long freezing time: For example, the high speed of the ambient flow enhanced heat transfer between the droplet surface and the surrounding air. As a result, a water droplet took a long time to freeze to ice.

Base on the dimensional analysis and the test classification, the experimental data of the freezing of hemispherical droplets were presented in four groups: freezing time, average air-side convection coefficient, the position of the freezing front, and the

temperature field. The tabular presentations in Appendix A gave both dimensional and nondimensional form, while the graphics only gave the nondimensional form.

6.2 Freezing Time

The experimental data for the freezing time of hemispherical water droplets were presented in Table A.1. The relationships among the dimensionless numbers were shown in Figures 6.1, 6.2, and 6.3.

In Figure 6.1, the dimensionless freezing time τ decreased with increasing Am . A large Am meant a large ambient-to-plate temperature difference, a slow ambient flow, and a small hemispherical droplet. In this case, the conduction heat transfer drew the temperature at everywhere of the droplet to the cold plate temperature. During this fast temperature dropping, the droplet experienced a phase change process and changed its state from liquid to solid. For small Am , the effect of heat transfer at the surface of a droplet became stronger and tried to keep the surface temperature of the droplet to the ambient temperature. In this way, the temperature dropping rate was lowered and the freezing time became longer.

Figure 6.2 shows the effect of Re on freezing time of hemispherical droplets. The concentration of the test data gave a clear relationship between those two numbers. When Re was large, which meant a high velocity of the ambient air or a large radius of the droplet, the heat transfer between the droplet and the ambient air was high. So that the cooling process of the droplet was prolonged.

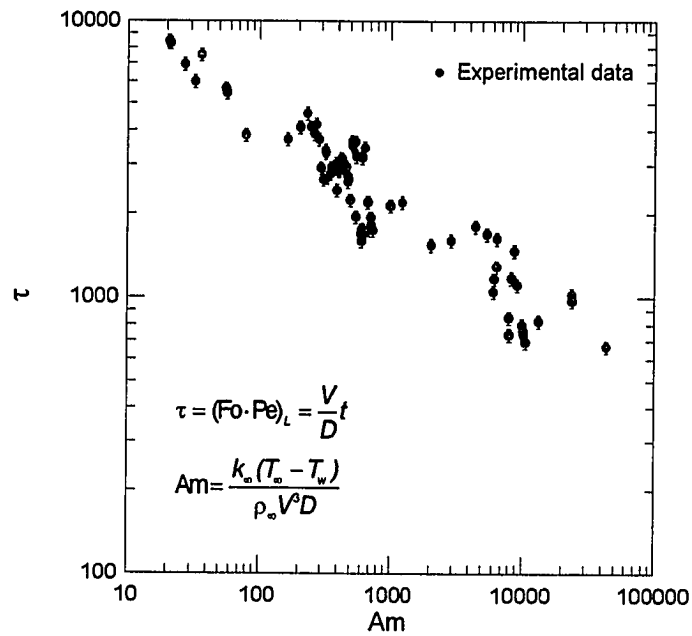


Figure 6.1 Effect of Am on freezing time for hemispherical droplets.

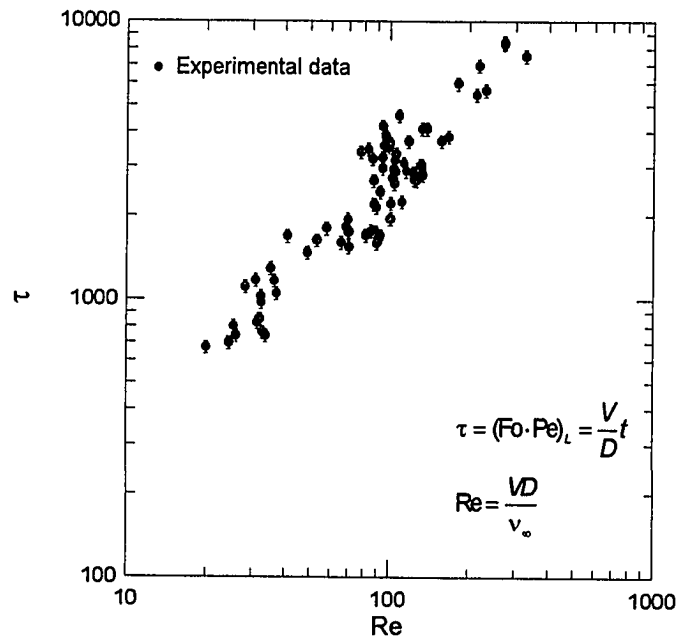


Figure 6.2 Effect of flow field on freezing time for hemispherical droplets.

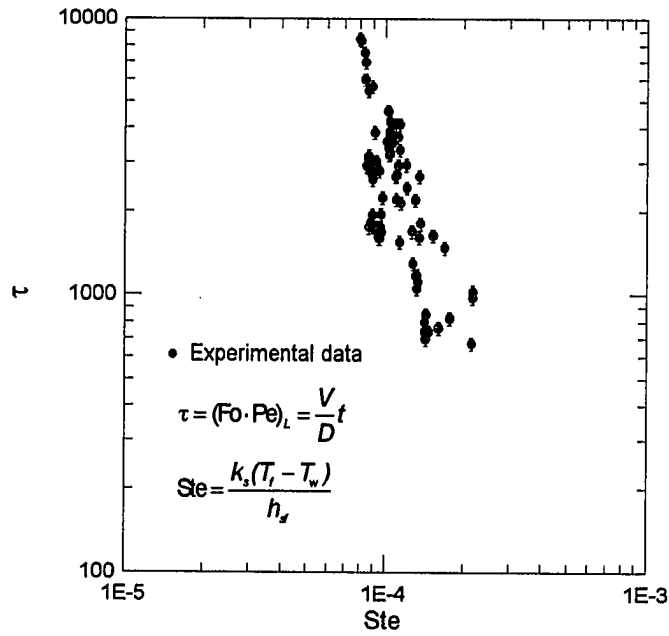


Figure 6.3 Effect of heat transfer on freezing time for hemispherical droplets.

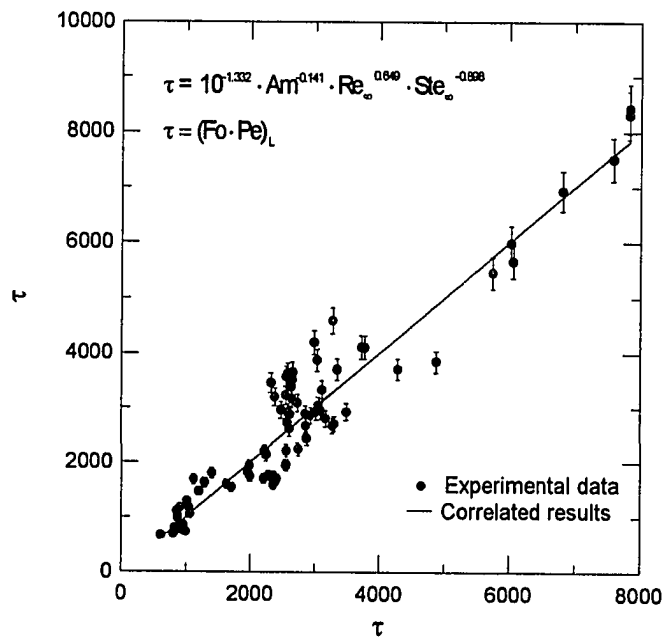


Figure 6.4 The comparison of correlation predictions and experimental data.

Figure 6.3 shows the experimental data of τ versus Ste . The Stefan number represented the importance of the heat capacity of the solid relative to the latent heat. If the latent heat of freezing for water/ice was considered fixed, then the Stefan number stood for the cold plate temperature depression below the freezing temperature. A large Stefan number meant a lower plate temperature, which accelerated the cooling process of droplet and decreased the freezing time.

Dimensional analysis reduced typically a freezing problem to four variables shown in Eq.(6.3). For a given body shape, the functional relationship could be established by take a large number of experiments, Because the data fell on reasonably straight lines when plotted on *log-log* scale, it was customary to fit the functional relation to a power-law:

$$\tau = C \cdot Am_{\infty}^m \cdot Re_{\infty}^n \cdot Ste_L^q \quad (6.5)$$

where m , n , and q were exponents and the dimensionless constant C depended on generic shape. The power-law relation was suggested for laminar flow and all of the constants would be determined by experiments.

Based on the discrete data points in Table A.1, the multiple linear regression was used to get the empirical correlation among τ , Am , Re , and Ste as following:

$$\tau = 10^{-1.332} Am_{\infty}^{-0.141} Re_{\infty}^{0.649} Ste_L^{-0.898} \quad (6.6)$$

$$20 < Am_{\infty} < 4 \times 10^4$$

$$20 < Re_{\infty} < 300$$

$$8 \times 10^{-5} < Ste_L < 2 \times 10^{-4}$$

In this expression the properties of air flow were evaluated at the film temperature $(0.5(T_w + T_\infty))$. The characteristic length equaled to the radius of a droplet.

The comparison of experimental data and correlated results was shown in Figure 6.4. The coefficient of determination was 0.58 and the correlation coefficient was 0.76. These results indicated that 76 percent of the original uncertainty had been explained by Eq.(6.6).

The following conclusions could be drawn based on the above analysis:

- The introduction of the dimensionless number Am was very helpful for data reduction of the freezing of hemispherical droplet on a cold metal plate. Note that the data fell on reasonably straight bands, which yielded to develop a nice correlation among these variables and made the freezing time of hemispherical droplets predictable.
- Because the empirical correlation, Eq.(6.6), was obtained by a least-squares fit of the experimental data when heat was transferred by conduction only within a droplet, there should be no dependence on the Rayleigh number or the Grashof number. However, the ranges of the Ra and the Gr in table A.1 were listed here for reference: Rayleigh number, from 15 to 390, Grashof number, from 1 to 15.

6.3 The Average Air-Side Convection Coefficient

For the study of heat transfer and temperature distribution of condensate droplets during phase transition, the boundary condition of the third kind corresponded to the existence of convection heating at the surface of droplets. The air-side convection coefficient played a key role in the energy transfer.

An empirical approach involving performing heat transfer measurements under controlled laboratory conditions and correlating the data in forms of dimensionless parameters was conducted in this investigation. Figure 6.5 illustrates the schematic of the test section in the experimental setup. A conditioned air stream flew over the plate at a low speed to maintain a uniform ambient air temperature. The surface temperature, T_w , was kept at a constant value within $\pm 0.5^\circ\text{C}$ of the dew point of the air by the thermal electric module. Convection heat transfer occurred from ambient air to the cold plate. It would be a simple matter to measure T_w and T_∞ , as well as the q'' , which was measured with a film thermal meter. The air-side convection coefficient, \bar{h} , which was an average value associated with the entire plate, could be computed from Newton's law of cooling. Moreover, from knowledge of the plate length, H , and the fluid properties, the Nusselt, Reynolds, and Am numbers could be computed from their definitions.

The equivalent thermal circuit for Figure 6.5 is shown in Figure 6.6. If the system was under steady state and steady flow, then

$$q'' = \bar{h}(T_\infty - T_w) = h_i(T_\infty - T_i) = \frac{k}{\delta}(T_i - T_w) \quad (6.7)$$

Note that there was a problem in the definition of \bar{h} . Technically speaking, h_i was the value at the droplet surface. \bar{h} was the overall heat transfer coefficient and differed from h_i . The reasons why \bar{h} was measured included:

- A method was not available to measure the surface temperature of a liquid droplet.
- On a cold plate, there were a number of droplets with different sizes. The local surface temperature of the droplets could be expected to vary by size and time.
- In industrial design, the ambient temperature and the surface temperature of a heat exchanger were often known. The introduction of \bar{h} allowed for a correlation that could be more readily applied.

The procedure for measuring the average air-side convection coefficient could be repeated for a variety of test conditions. The velocity U_∞ , T_∞ , and T_w could be varied, while the working fluid remained the same. The experimental data were presented in Table A.2. Many different values of the Nusselt number corresponding to a wide range of Re and Am were obtained and the results were plotted on a *log-log* scale, as shown in Figure 6.7 and Figure 6.8. If the surface temperature was maintained at a constant value, the Nu increased with either decreasing ambient air temperature or increasing Re but with decreasing Am.

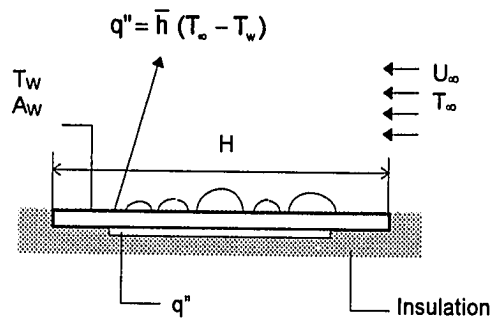


Figure 6.5 Experiment for measuring the average air-side convection coefficient \bar{h} .

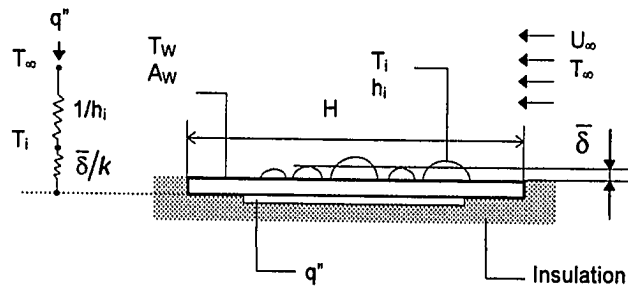


Figure 6.6 The equivalent circuit for Figure 6.5.

The primary objective of this study was to determine the air-side convection coefficient for flat plate covered with condensate droplets. In particular a specific form of the function represented the coefficient was expected to be obtained by experiments. By nondimensionalizing analysis, the average air-side convection coefficient might be correlated by equation of the form

$$\text{Nu}_\infty = f(\text{Re}_\infty, \text{Am}_\infty) \quad (6.8)$$

As was often the case, the results fell close to straight lines in Figure 6.7 and Figure 6.8, which might be represented by a algebraic expression of the form

$$\text{Nu}_\infty = C \text{Re}_\infty^m \text{Am}_\infty^n \quad (6.9)$$

The specific values of the coefficient C and exponents m and n varied with the surface geometry and the type of flow.

By using multiple linear regression, C , m and n could be determined and the correlation could be expressed as following

$$\text{Nu}_\infty = 10^{6.094} \text{Re}_\infty^{-1.238} \text{Am}_\infty^{-0.478} \quad (6.10)$$

$$20 < \text{Re}_\infty < 1000$$

$$3 < \text{Am}_\infty < 1000$$

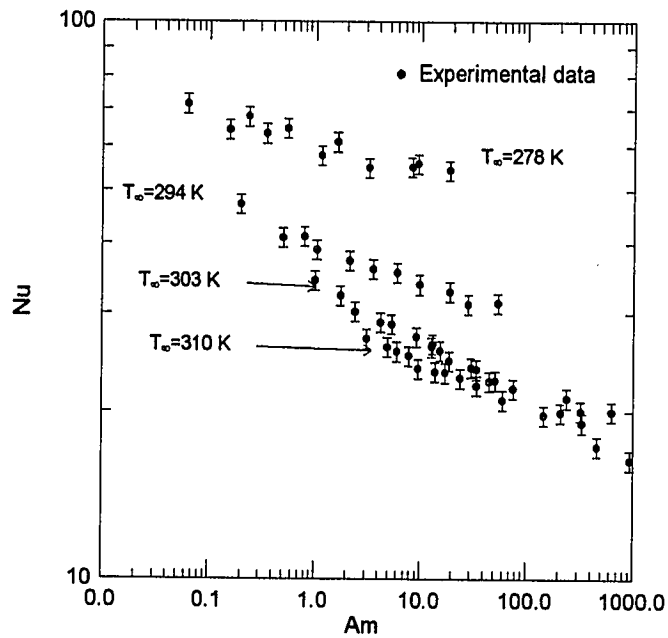


Figure 6.7 Effect of Am on convective heat transfer.

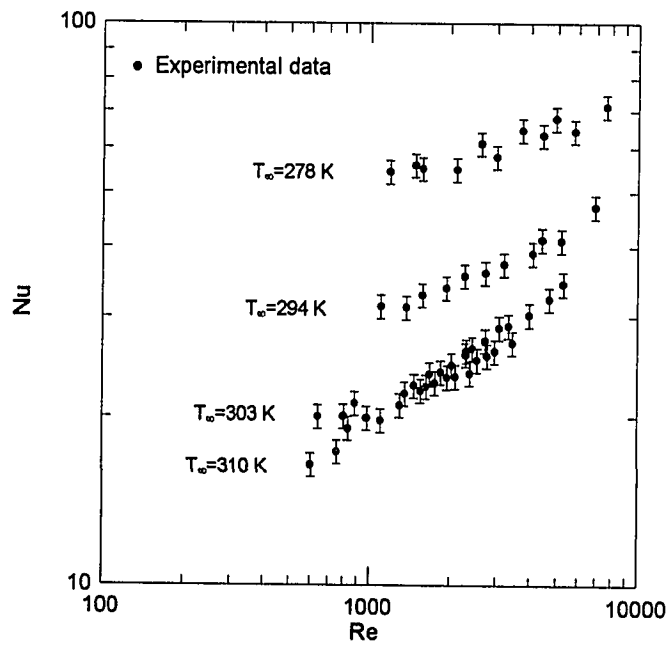


Figure 6.8 Effect of Re on convective heat transfer.

In this expression the properties of air flow were evaluated at the film temperature $(0.5(T_w + T_\infty))$. The characteristic length equaled to the radius of a droplet.

Figure 6.9 shows that the average air-side convection coefficient h varies with respect to Am .

The cold plate in the test section was sketched in Figure 6.11, which was a plate with an unheated starting length. The \bar{h} values were estimated by the following correlation (Incropera and Dewitt, 1990):

$$\overline{Nu} = \frac{H\bar{h}}{k} = 0.334 \left(\frac{V_\infty}{\nu} \right)^{1/2} \text{Pr}^{1/3} \int_{\xi}^{H+\xi} \frac{x^{1/2}}{x \left[1 - \left(\frac{\xi}{x} \right)^{3/4} \right]^{1/3}} dx \quad (6.11)$$

were also plotted in Figure 6.9.

The comparison of experimental data and correlated results was plotted in Figure 6.10. The coefficient of determination was 0.97 and the correlation coefficient was 0.98, indicating that 98 percent of the original uncertainty had been explained by Eq.(6.10).

Some preliminary conclusions could be drawn here:

- The air-side convection coefficient decreased with increasing air-to-plate temperature difference. Put in other words, if the plate temperature was constant, the higher the air temperature, the lower the air-side convection coefficient.
- When a plate was covered with condensate droplets, the average air-side convection coefficient would be bigger than that of a bare plate. The main

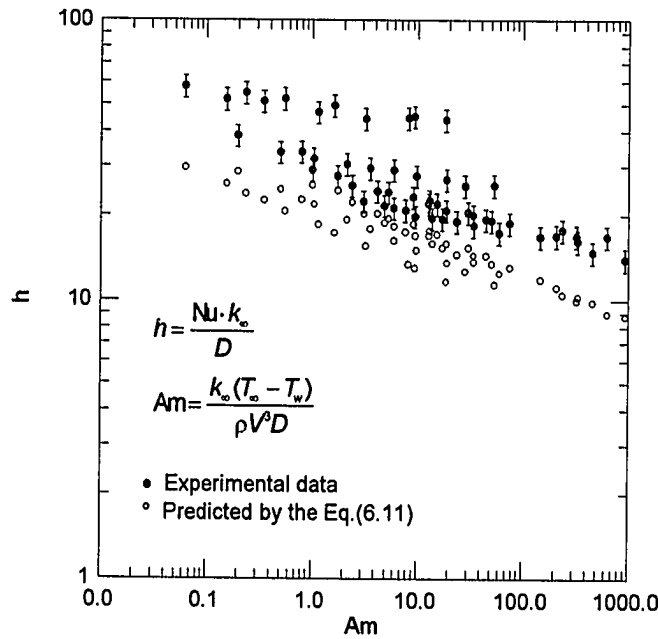


Figure 6.9 Effect of Am on average convective coefficient.

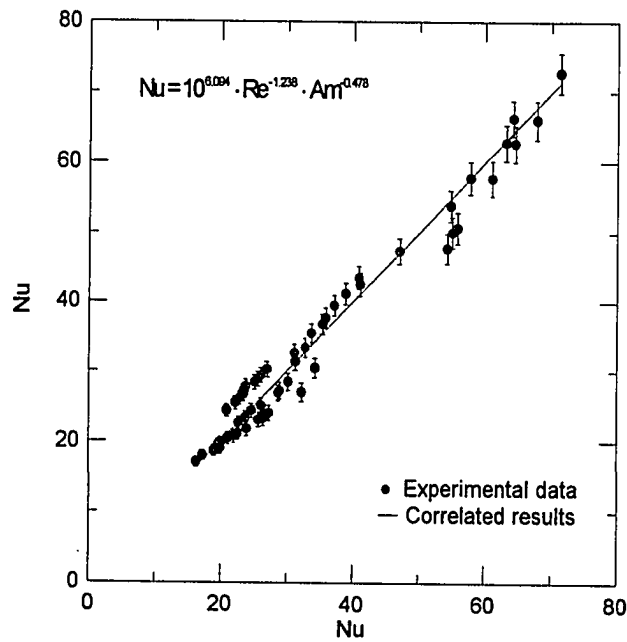


Figure 6.10 The comparison of correlation predictions and experimental data.

reason was that the droplets on the surface disturbed the formation of laminar boundary layer. The fluid fluctuations and flow turbulent enhanced the convective heat transfer.

- The average air-side convection coefficient for a plate with condensate droplets was much more sensitive than that for a bare surface to the change of ambient temperature.

6.4 Shape and Velocity of the Freezing Front

For the freezing of a hemispherical droplet on a cold plate, the ice nucleated at the base of the droplet and the freezing front moved up. Because of the density difference between water and ice, there was a small sharp projection at the top of a droplet after a droplet had been totally frozen to ice. With well-arranged light, the phase-change region could be highlighted and recorded on a videotape. In Figure 6.12, the gray band illustrates the freezing front at a time.

In order to accurately obtain the freezing rate, the area fraction of solid was introduced into this study and was discussed in detail in Chapter IV. The area fraction of solid was the ratio of the area below to above the gray band.

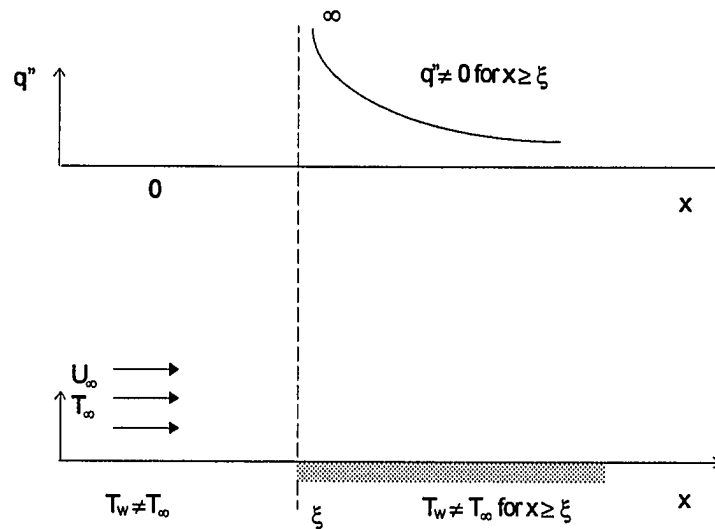


Figure 6.11 Sketch of flat plate flow with an unheated starting length.

The freezing front was not a flat surface and did not parallel to the horizontal copper plate. To make it easy to compare, the freezing front velocity was defined as:

$$V = \frac{\Delta S}{t_2 - t_1} = \frac{\Delta S}{\Delta t} \quad (6.12)$$

where ΔS , t_1 , t_2 were shown in Figure 6.13.

Videotape pictures provided images of freezing front locations versus time. Results were presented in Figure 6.14 for a typical freezing case. The freezing front moved very fast at the beginning of ice nucleation and slowed down with the built-up of ice at the base of the droplet. During freezing, there were several hesitations in the phase-change region movement.

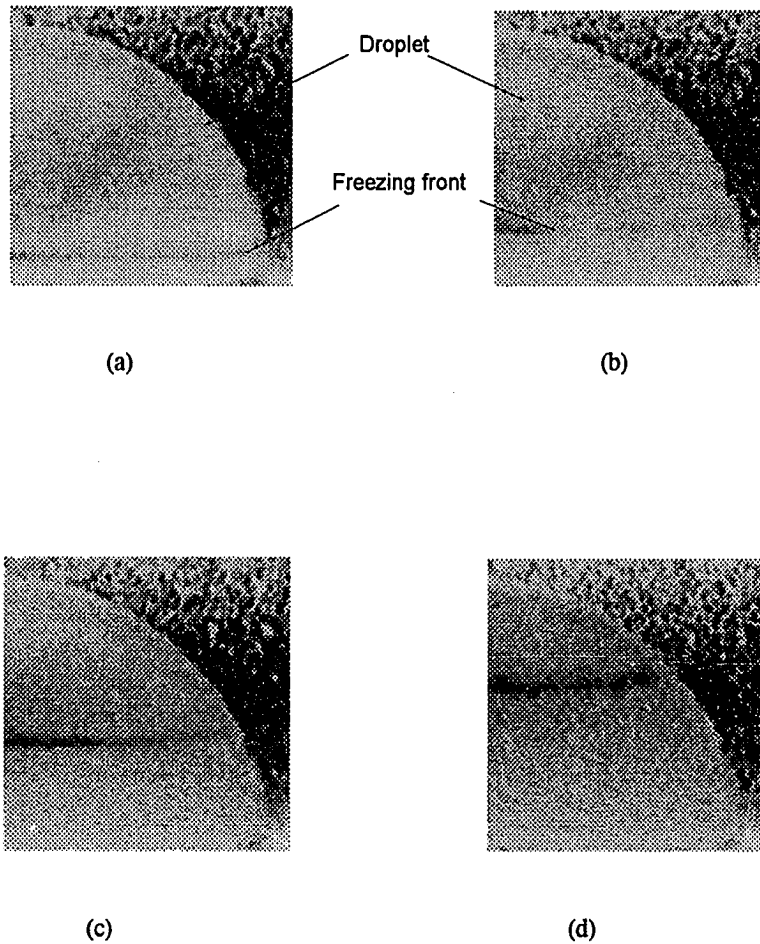


Figure 6.12 Freezing front acquired by the camera at (a) $t=0.12$ s, $f_s=0.14$, (b) $t=0.3$ s, $f_s=0.28$, (c) $t=0.75$ s, $f_s=0.52$, (d) $t=1.62$ s, $f_s=0.8$ ($R=0.9$ mm, $T_w = 263.3$ K, $T_\infty = 280.2$ K, $Re = 89.65$).

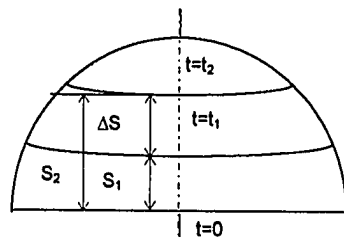


Figure 6.13 The locations of freezing front at different time.

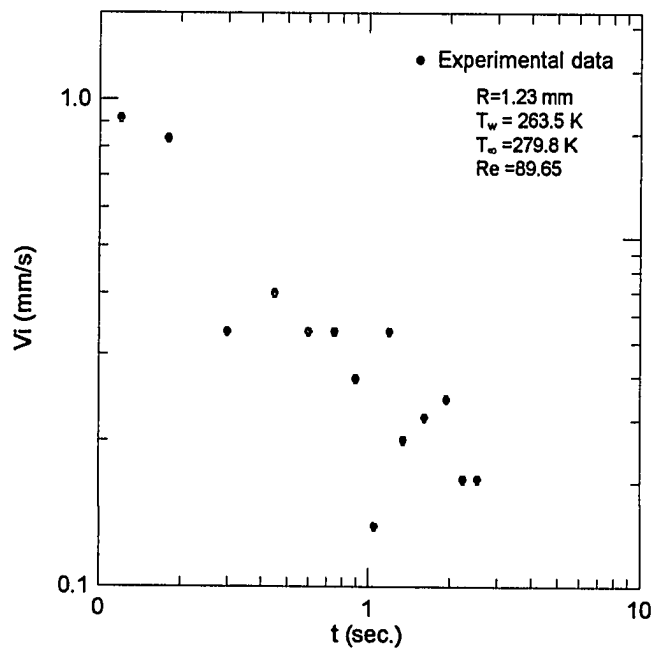


Figure 6.14 The measured freezing front velocity during freezing.

The freezing front information was very important to the development of mathematical model because phase-change region acted as the boundary between two phases. It was a special region that was belong neither to the liquid nor to the solid. In general, the following conclusions could be obtained:

- The ice initiated at the base of a droplet and the freezing front moves upward. The projection tip should be at the top of a droplet or the top point was frozen last.
- The velocity of freezing front reached immediately a maximum value after nucleation and then kept decreasing until to a stable value. The fluctuation of velocity implied that the freezing was not a continuous process. There were some hesitations during phase transition.

6.5 Temperature Field

To measure the temperature field in condensate droplet resulting from conditions imposed on its boundaries, a micro-thermocouple was inserted into the droplet with a micromanipulator as shown in Figure 6.15 and Figure 6.16.

When the test system ran at steady state and steady flow, the thermocouple probe was moved up and down within a droplet to obtain the temperature values at different positions. The bead of the thermocouple could also be located and monitored by means of the digital image system. The detail of the droplet and the relative position of the

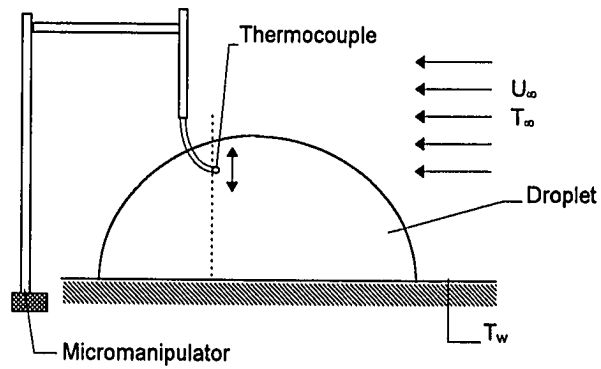


Figure 6.15 The schematic of inserting a thermocouple into a droplet with a micromanipulator.

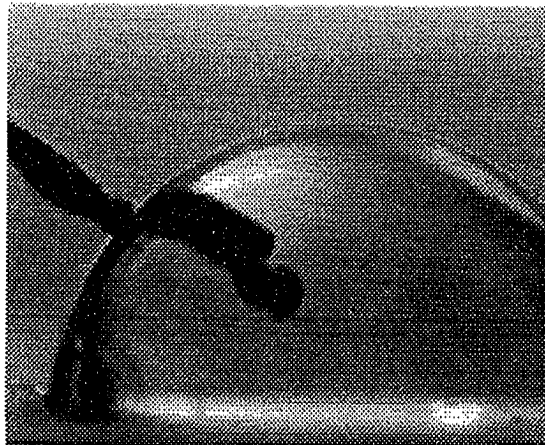


Figure 6.16 Micro-thermocouple placed in a 2.3 mm diameter water droplet.

thermocouple was shown in Figure 6.17. Some typical temperature distributions obtained from aforementioned method were shown in Figures 6.18, 6.19, and 6.20. The temperature gradient increased as the surface was approached from the base of the droplet.

Figure 6.21 shows the temperature distribution along a vertical line when the plate temperature was below the freezing temperature of purified water. The whole droplet was at the supercooling state. During the experiment, the surface temperature, the air temperature, and heat flux through the base of the droplet were displayed on the screen to make sure a steady state had been reached. The temperature distribution maintained the same as shown in Figure 6.21 for a long time. Then all of a sudden the ice started to nucleate at the base. The temperature at nucleation zone would go back to the freezing temperature and hold on that value until this zone was totally frozen to ice. Figure 6.22 shows the temperature rebound and Figure 6.23 shows the cooling curve at a location in ice region within a droplet.

The temperature distribution and temperature history were important in determining the reliability of a mathematical model. Of course, the above information could prove to be helpful in understanding the mechanism of heat transfer for a hemispherical droplet during freezing. The following were preliminary conclusions:

- The condensate droplets could be subcooled well below the freezing temperature.

As soon as the ice nucleated at a small zone, the sudden release of latent heat

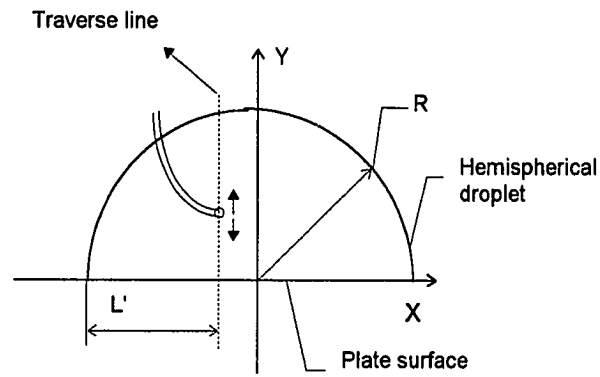


Figure 6.17 The position and the traverse line of a thermocouple in a droplet.

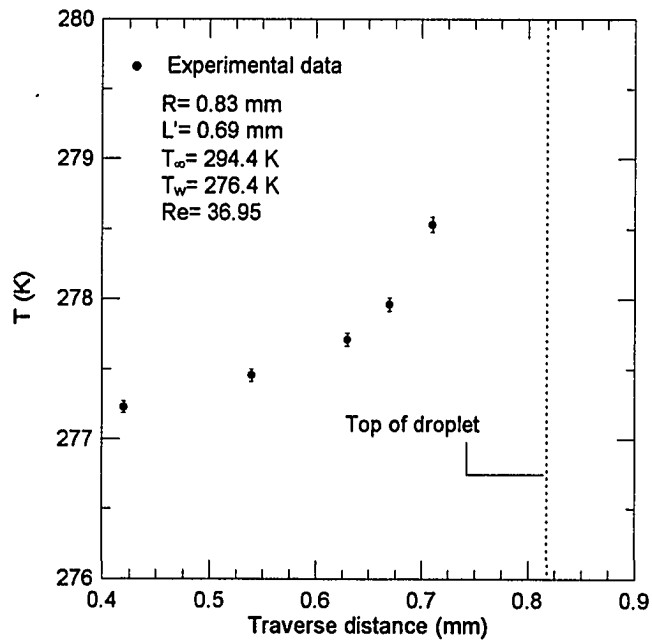


Figure 6.18 The temperature distribution along a traverse line ($R=0.83 \text{ mm}$).

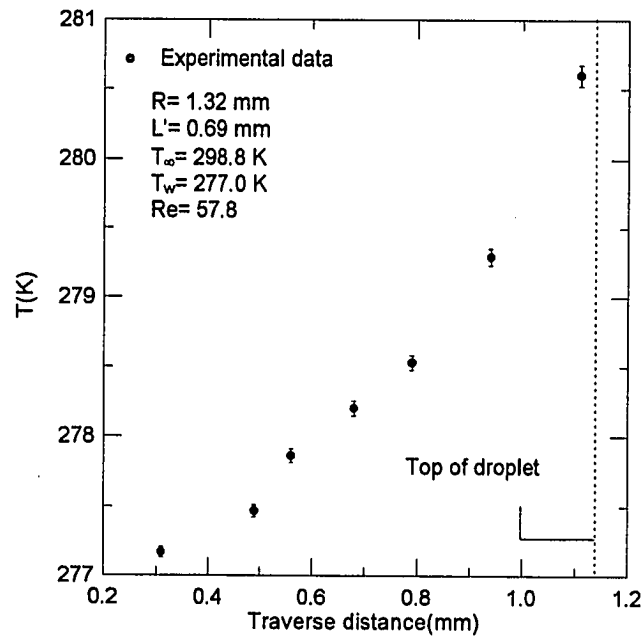


Figure 6.19 The temperature distribution along a traverse line ($R=1.32$ mm).

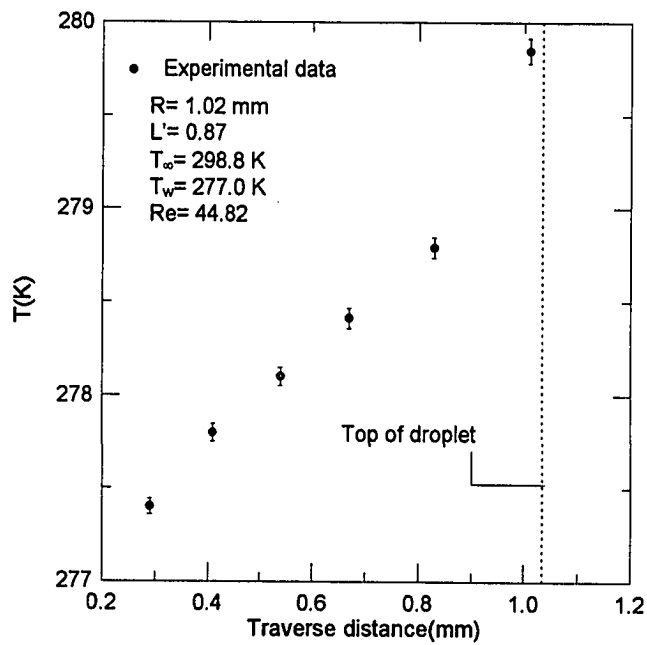


Figure 6.20 The temperature distribution along a traverse line ($R=1.02$ mm).

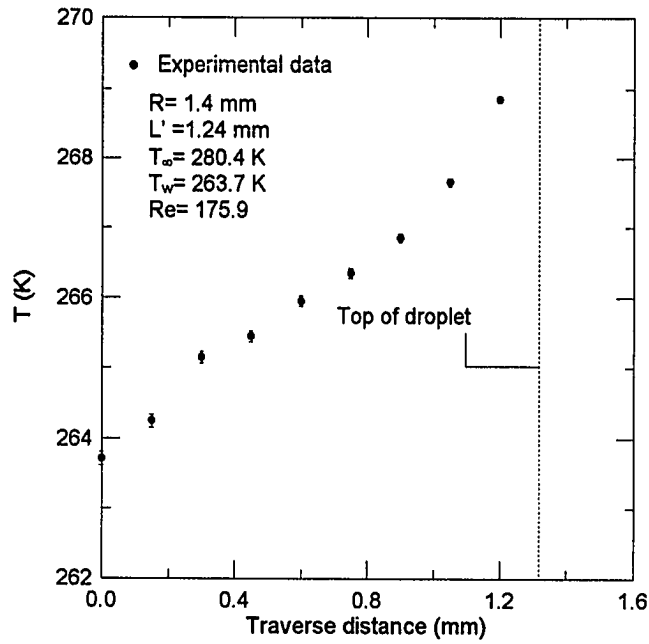


Figure 6.21 The temperature distribution along the traverse line in Figure 5.14 ($R=1.4$ mm).

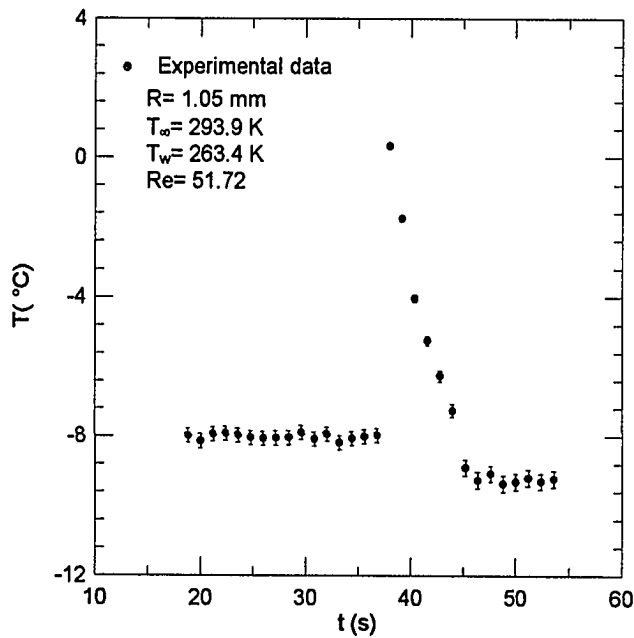


Figure 6.22 The temperature history at a point within a droplet.

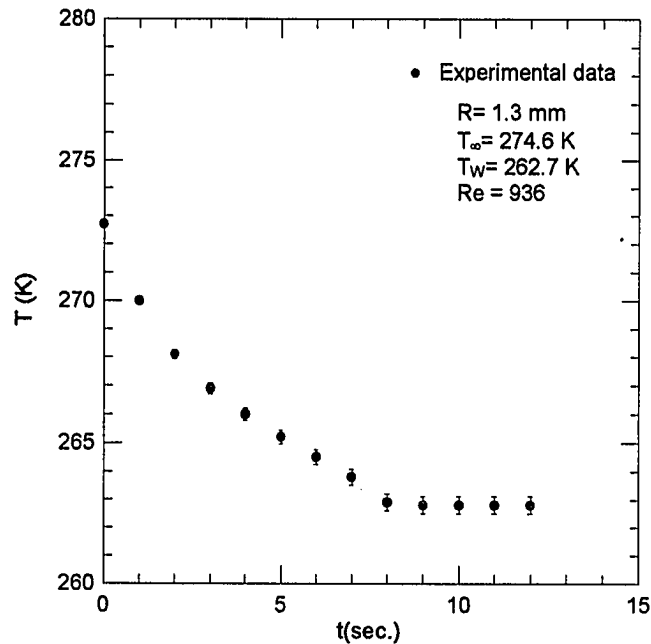


Figure 6.23 The cooling curve at nodal element ($r=0.77$ mm, $\theta=36^\circ$).

caused the local temperature to go back to the freezing temperature and to hold on that value throughout the freezing process.

- Although a droplet looked very small, the temperature gradient within the liquid could not be neglected. It was because the temperature gradient existed in a droplet that the heat transfer rate through the copper plate was reduced significantly. When dropwise condensation was used to enhance the heat transfer in heat exchanger design, drainage of the condensate was very important. Otherwise, condensate droplets would insulate the heat exchanger surface and made its performance even worse.

6.6 Summary

In this chapter, the experimental results had been presented and discussed. Droplet freezing time, temperature field, average air-side convection coefficient, and velocity of the freezing front had been presented. Two empirical correlations were developed for the study of the heat transfer during freezing of hemispherical droplets.

Wherever possible, the results had been qualitatively compared with what had been reported in literature. In general, the experimental results from present study compared well with what have been reported by previous investigators.

CHAPTER VII

COMPARISON OF EXPERIMENTAL AND MODEL RESULTS

In this chapter, the experimental results were compared to those predicted by the mathematical model. Because of the limitations of the test setup, some quantities relating to water droplet surfaces could not be measured. Comparisons of following variables for a single droplet at different test conditions were presented in this chapter.

- Steady-state temperature distribution and nodal temperature history
- Freezing front velocity
- Freezing front position and the area fraction of solid
- Freezing time

7.1 Steady-State Temperature Distribution and Nodal Temperature History

Figures 7.1 through 7.3 show comparisons of the measured and estimated steady-state temperature distributions in the vertical direction within droplets (L' was shown in Figure 6.17). The dashed lines show the temperature distributions predicted by the mathematical model based on the air-side convection coefficient calculated with Whitaker's correlation, while the solid lines represented the predicted temperature distributions with air-side convection coefficient calculated with Eq.(6.10). Whitaker's correlation was obtained by using curve-fit with the experimental data of Vliet and Leppert (1961) and the supporting data of Yuge (1960) on heat transfer between metal

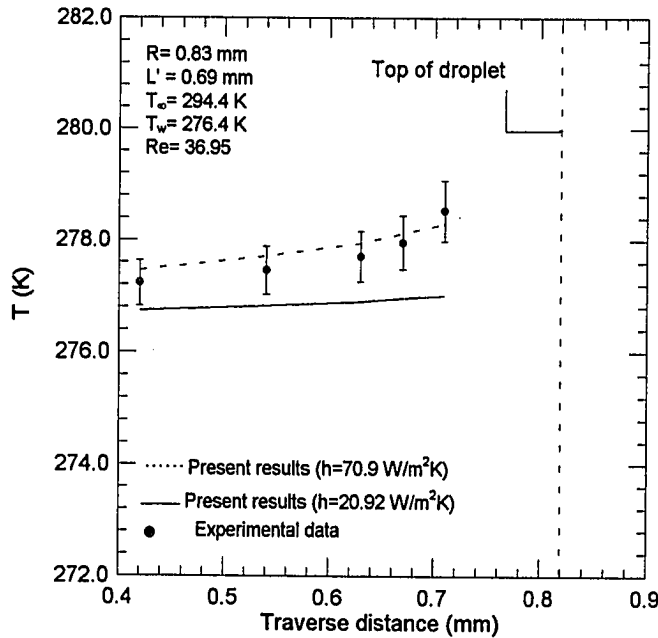


Figure 7.1 Temperature distribution along a vertical line: Comparison between model and experiment ($R=0.83 \text{ mm}$).

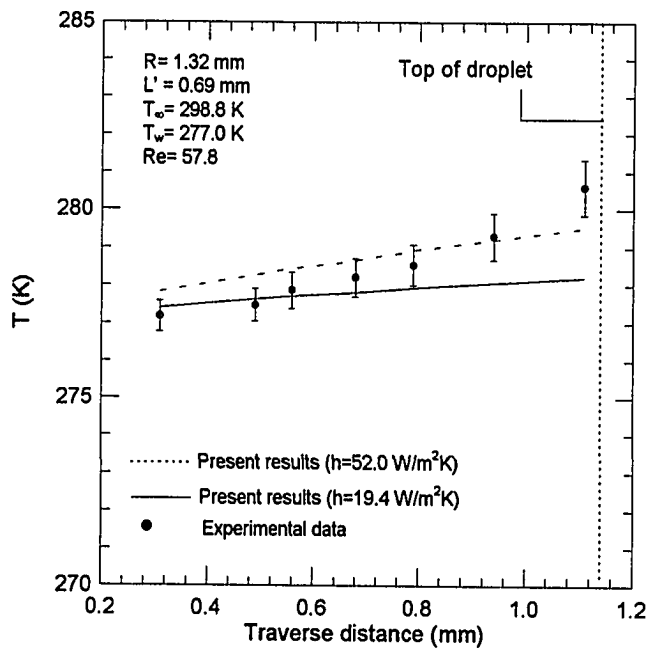


Figure 7.2 Temperature distribution along a vertical line: Comparison between model and experiment ($R=1.32 \text{ mm}$).

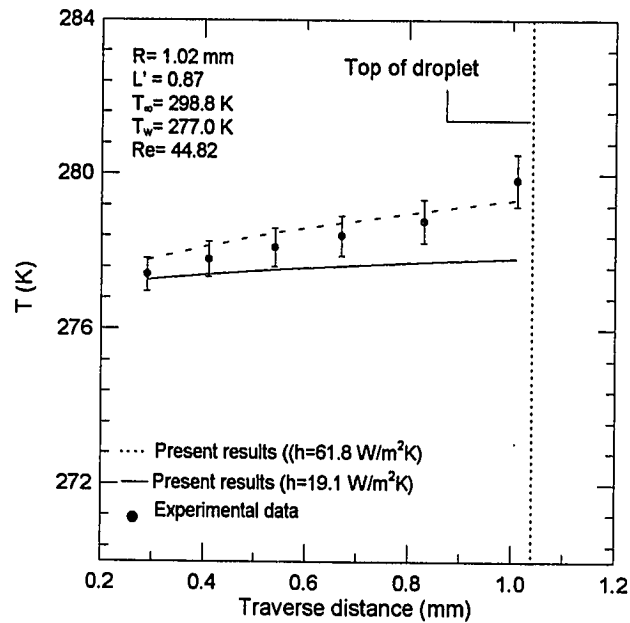


Figure 7.3 Temperature distribution along a vertical line: Comparison between model and experiment ($R=1.02$ mm).

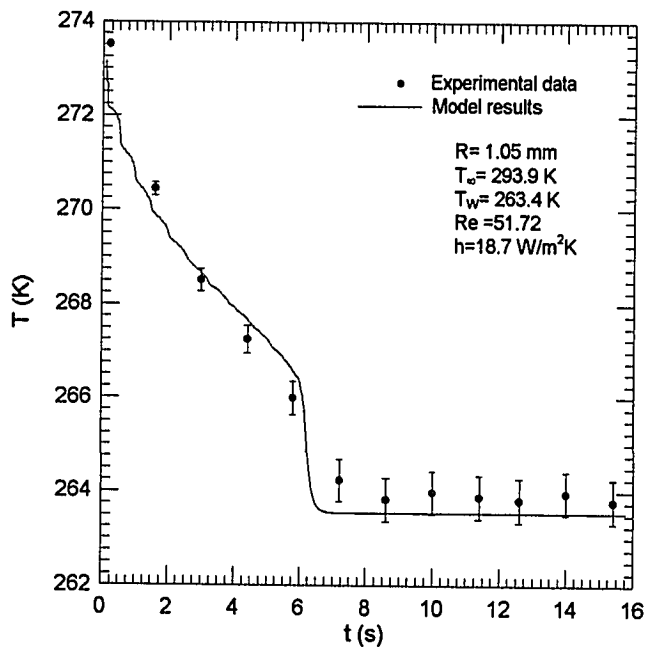


Figure 7.4 The temperature history: Comparison of model and experiment ($r=0.39$ mm, $\theta=81.2^\circ$).

spheres and air flow. It could be extended to calculate the air-side convection coefficient for flow past single liquid droplet. Because the experiments described in Chapter VI could not measure the droplet surface temperature, the air-side convection coefficient calculated by using Eq.(6.10) was lower than that obtained from Whitaker's correlation. It was the main reason why the dashed lines had good agreements with the experimental data. For instance, in Figure 7.2 the average difference was 0.1°C between the dashed lines and the measured data, and 0.3°C between the solid lines and the measured data.

One other important observation from Figures 6.1 through 6.3 was that when the edge of a droplet was reached, the discrepancies between the experimental data and the model results increased appreciably. There were several possible reasons that might explain the difference between the predicted and measured temperatures near the edge of the droplets. First, when a thermocouple junction was pulled near the surface of a droplet, the heat gain by conduction through the leads were not negligible. Second, there was circulation of water induced by the viscous force at the droplet surface. This motion was confirmed and recorded onto a videotape in the present study. Surface circulation should have enhanced the heat transfer between the droplet surface and ambient air and led to a large temperature gradient across the surface of a droplet. Third, the mathematical model that neglected the effect of mass transfer at the droplet surface ensured that all of the interior nodes did not interact directly with surrounding air at T_{∞} . It ignored the energy transfer occurred at the air-liquid interface. As a result, the model results were always lower than the experimental data near the droplet surface.

Figures 7.4 and 7.5 illustrate the temperature histories (or the cooling curves) at two nodes within the droplets during freezing. The average difference between the experimental data and model predictions was 0.3°C for Figure 7.4, and 0.6°C for Figure 7.5. The predicted temperature distribution showed a sudden drop just before the steady state value was reached. This behavior could be explained by the nature of the numerical formulation. As shown in Figure 3.10, when a nodal element stepped into the phase-change region, its heat capacity was set to a very large value (10^{20}) to hold a constant temperature at this node. At a time step during the model calculation, a number of nodes released latent heat in the phase-change region and slowed down the cooling process of a droplet. After the final node, usually at the top of a droplet, finished freezing, all of the nodes in the computational region were frozen to solid with ice properties. The droplet cooled down to a steady-state at no time and thus caused a sudden temperature drop.

The good agreement in temperature shows that conduction was a valid assumption on which to base the calculation of heat flow through droplet on horizontal surface during phase change. The comparison provided a direct experimental justification for the pure conduction in the freezing analysis of a hemispherical droplet.

7.2 Freezing Front Velocity

The Freezing front velocity was calculated by using Eq.(3.33) for a droplet with a 0.9 mm radius, ambient temperature of 7°C , and surface temperature of -9.9°C (Figure 7.6). At $t=0.1$, the base of the droplet was freezing and the Freezing front velocity

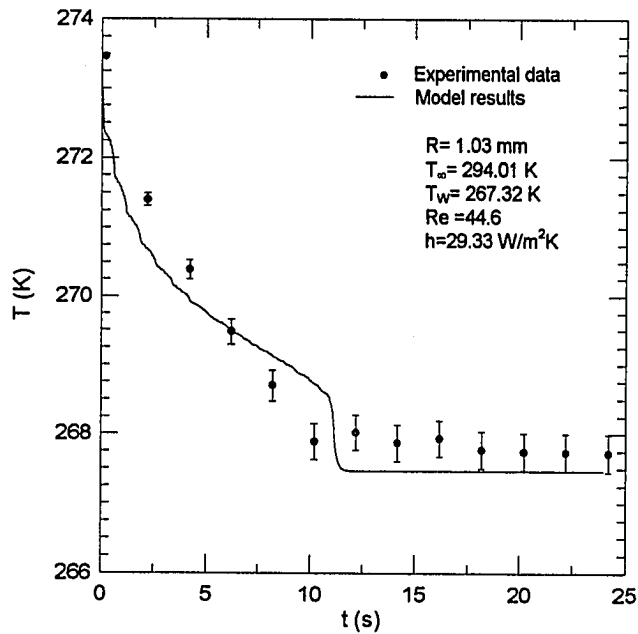


Figure 7.5 The temperature history: Comparison of model and experiment ($r=0.33$ mm, $\theta=79.4^\circ$).

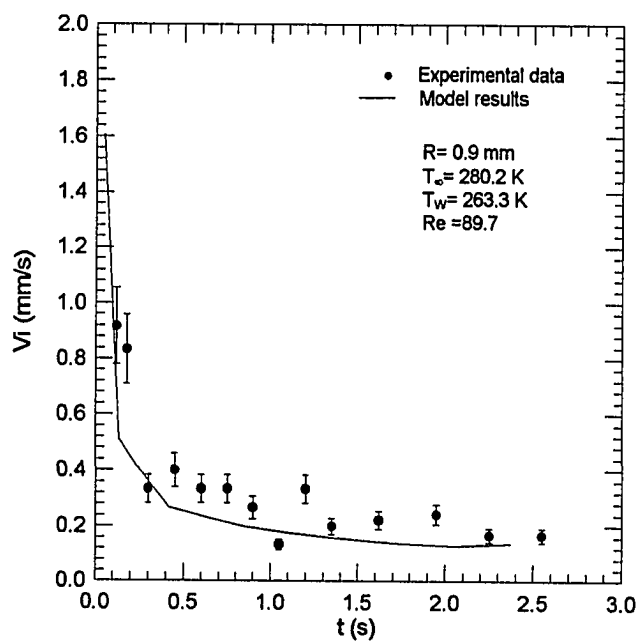


Figure 7.6 The velocity of the freezing front: Comparison of the numerical predictions and the experimental results.

reached 1.6 mm/s. With the ice thickness increased, the velocity of the freezing front decreased significantly to 0.22 mm/s at $t=0.5$ s. In the experimental study, the freezing process for the same droplet, same metal surface temperature, and same air temperature was taped. The time interval between video frames was 1/30 s. The Freezing front velocity was obtained by measuring the advancing freezing front from one frame of the video to the next, as plotted in Figure 7.6 for comparison. At $t<0.1$ s, the observed freezing front velocity was lower than that predicted. The mathematical model overestimated the Freezing front velocity by as high as 0.32 mm/s. The agreement between data and predictions was reasonably good for $t>0.5$ s, with the average difference less than 0.11 mm/s. Figure 7.7 shows the Freezing front velocity for a droplet of 1.23 mm radius, ambient temperature of 6.8°C, and surface temperature of -9.5°C. It displayed a common trend as that plotted in Figure 7.6. Note also that the measured freezing front velocity showed some fluctuations, while the predicted Freezing front velocity decreased during the freezing. Explanations of the fluctuations occurring during freezing were given in Chapter IV.

7.3 Freezing Front Position and the Area Fraction of Solid

For a droplet with a 0.9 mm radius, ambient air temperature of 7.1°C, and cold plate temperature of -9.4°C, the measured and predicted total freezing times were 4.35 s and 5.26 s, respectively.

The area fractions of solid at different times were measured (Figures 7.8, 7.10, 7.12, and 7.14) and compared with the predictions of mathematical model (Figures 7.9, 7.11, 7.13, 7.15). The freezing rate was relatively high due to the sharp temperature gradient at the base of a droplet but gradually decreased due to the increase in the thermal resistance of the ice layer. The predicted freezing rates were lower than the measured ones. Both the experimental images and the numerical simulation showed the inclined planar freezing front, with the outer edge higher than that at the symmetric plane.

Comparisons between predicted and experimental area fractions of solid were shown in Figure 7.16. The model underestimated the area fraction of solid by as low as 28% at $t=1.62$ s. Nevertheless, Qualitative agreement was obtained.

7.4. Freezing Time

The dimensionless freezing times obtained from numerical simulation and experiments are compared in Figure 7.17. The dimensionless variables τ and Am , rather than the dimensional parameters, were used because they correlated the results for the various values of radii of droplets, freezing times, the velocities of ambient air, and the air-to-plate surface temperature differences. The motivation for using the dimensionless

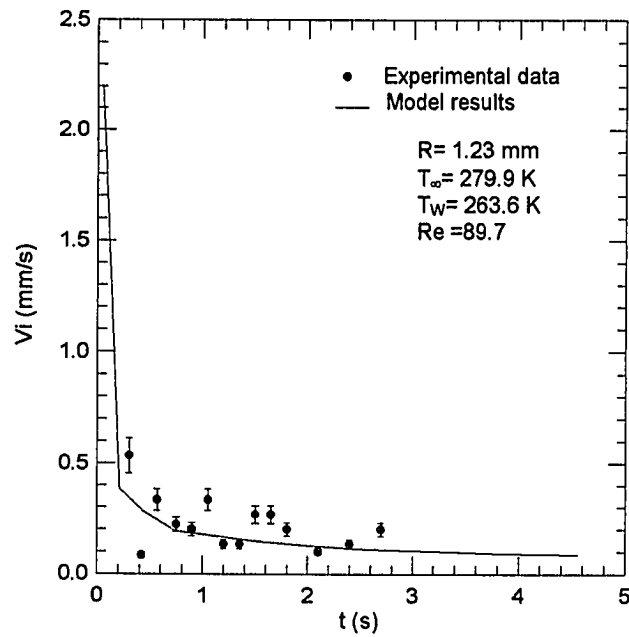
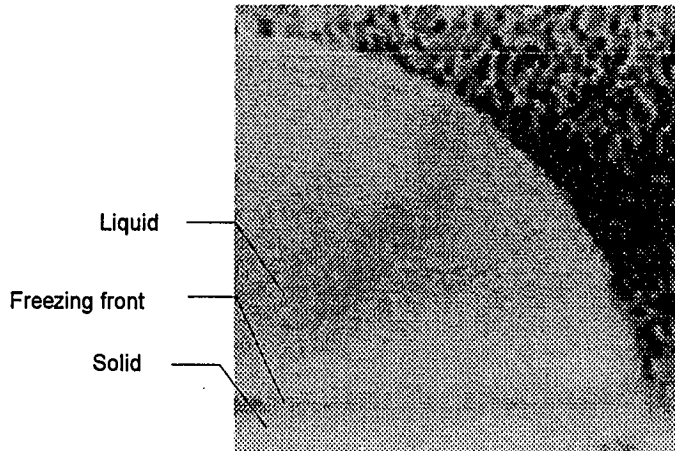


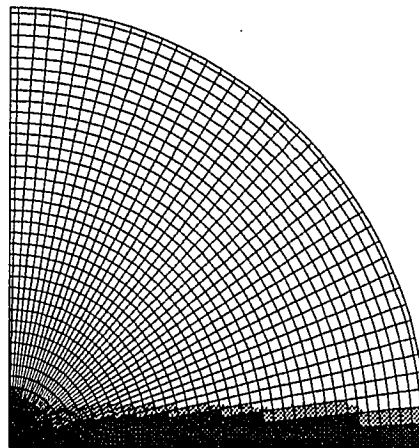
Figure 7.7 The velocity of the freezing front: Comparison of the numerical predictions and the experimental results.



$$f_s = 14\%$$

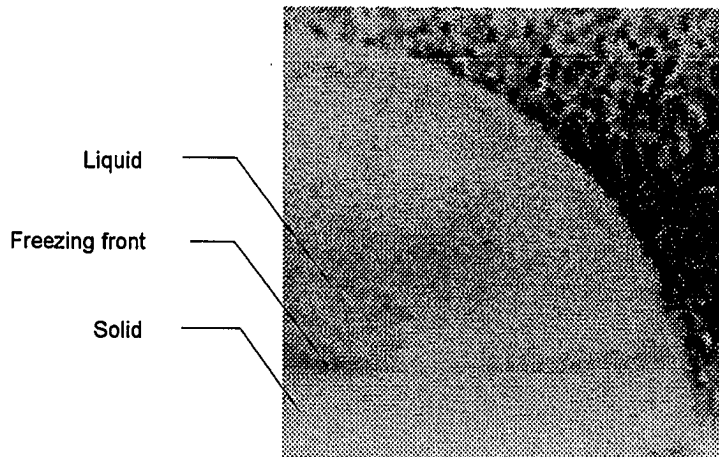
Figure 7.8 Freezing front position measured with the image acquisition system at $t=0.12$ s ($R=0.9$ mm, $T_w = 263.3$ K, $T_\infty = 280.2$ K, $Re = 89.65$).

- Liquid
- Phase change
- Solid



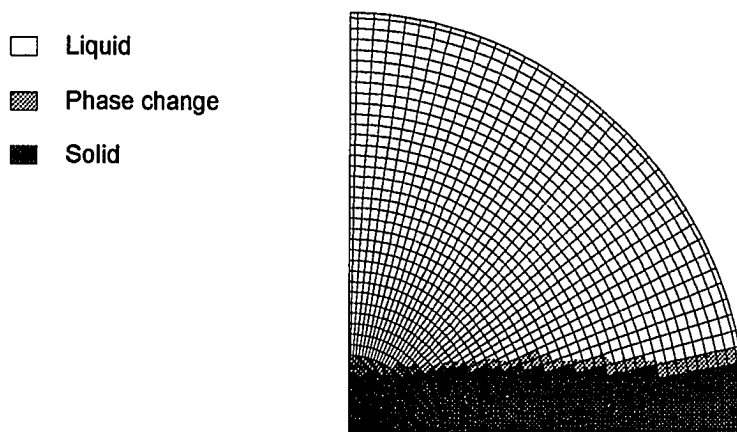
$$f_s = 13.1\%$$

Figure 7.9 Freezing front position predicted with the mathematical model at $t=0.12$ s ($R=0.9$ mm, $T_w = 263.3$ K, $T_\infty = 280.2$ K, $Re = 89.65$).



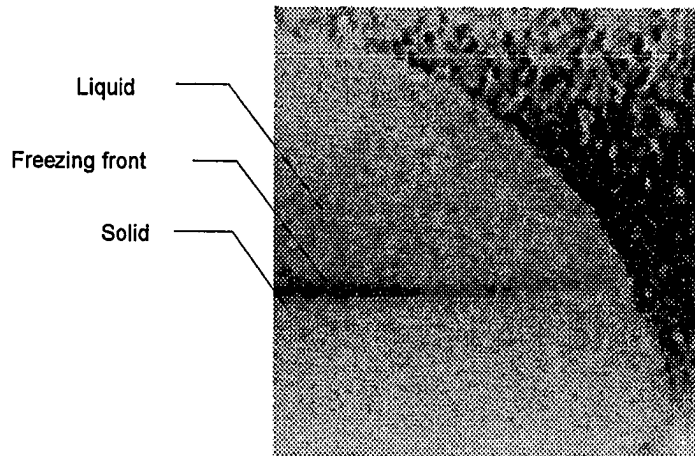
$f_s = 28\%$

Figure 7.10 Freezing front position measured with the image acquisition system at $t=0.3$ s ($R=0.9$ mm, $T_w = 263.3$ K, $T_\infty = 280.2$ K, $Re = 89.65$).



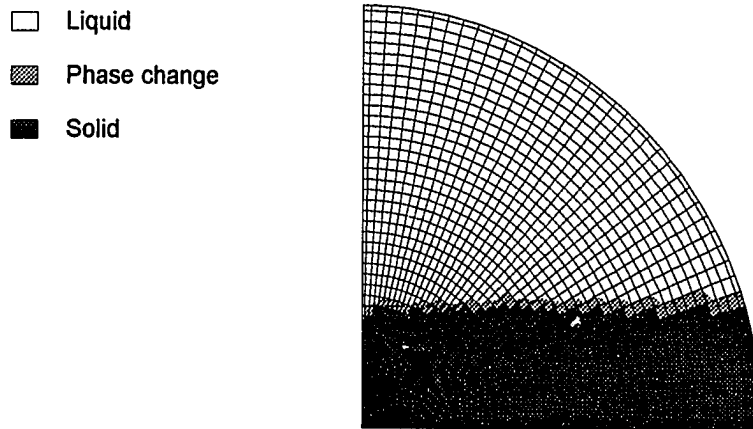
$f_s = 23.6\%$

Figure 7.11 Freezing front position predicted with the mathematical model at $t=0.3$ s ($R=0.9$ mm, $T_w = 263.3$ K, $T_\infty = 280.2$ K, $Re = 89.65$).



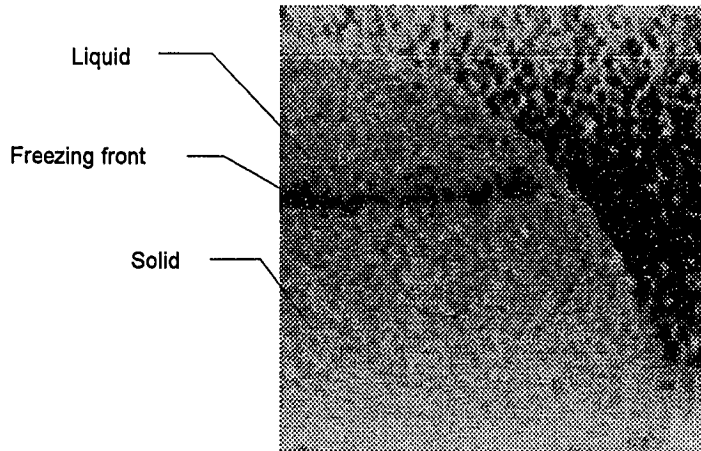
$$f_s = 52\%$$

Figure 7.12 Freezing front position measured with the image acquisition system at $t=0.75$ s ($R=0.9$ mm, $T_w = 263.3$ K, $T_\infty = 280.2$ K, $Re = 89.65$).



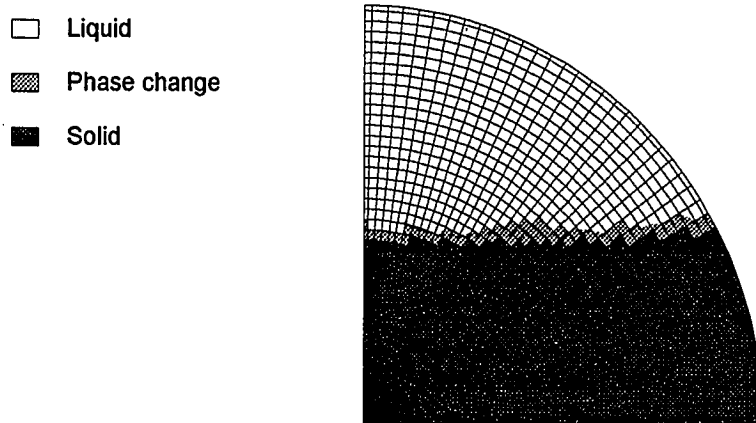
$$f_s = 38.4\%$$

Figure 7.13 Freezing front position predicted with the mathematical model at $t=0.75$ s ($R=0.9$ mm, $T_w = 263.3$ K, $T_\infty = 280.2$ K, $Re = 89.65$).



$f_s = 80\%$

Figure 7.14 Freezing front position measured with the image acquisition system at $t=1.62$ s ($R=0.9$ mm, $T_w = 263.3$ K, $T_\infty = 280.2$ K, $Re = 89.65$).



$f_s = 57.8\%$

Figure 7.15 Freezing front position predicted with the mathematical model at $t=1.62$ s ($R=0.9$ mm, $T_w = 263.3$ K, $T_\infty = 280.2$ K, $Re = 89.65$).

variables came from an examination of the random test conditions. A brief description of the physical significance of each dimensionless variable was presented in Chapter VI. The results of Figure 7.17 indicated that the use of the new defined dimensionless variables accounted for most of the dependence of τ on Am .

The predicted values were lower than experimental data, which indicated that the mathematical model underestimated the freezing time. This discrepancy might be caused by the supercooling at the very beginning of a freezing. However, the model predictions had the same trends as the experimental data.

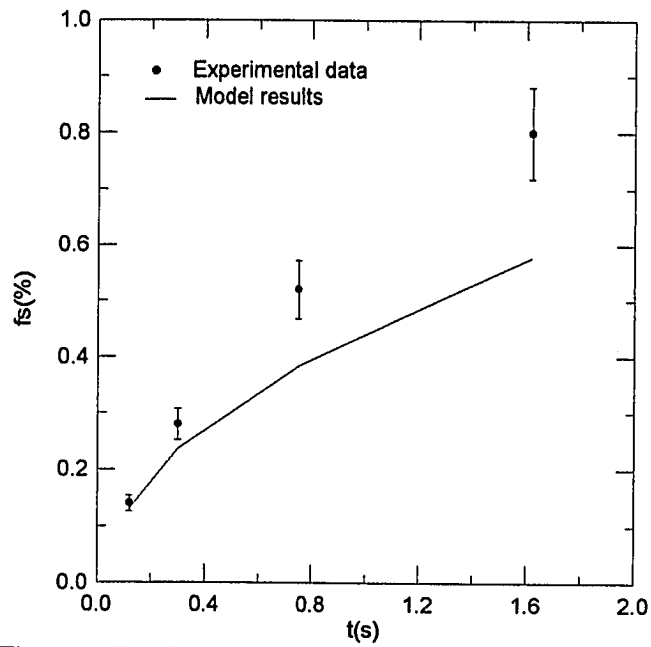


Figure 7.16 The area fraction of solid: Comparison of the experimental and numerical results.

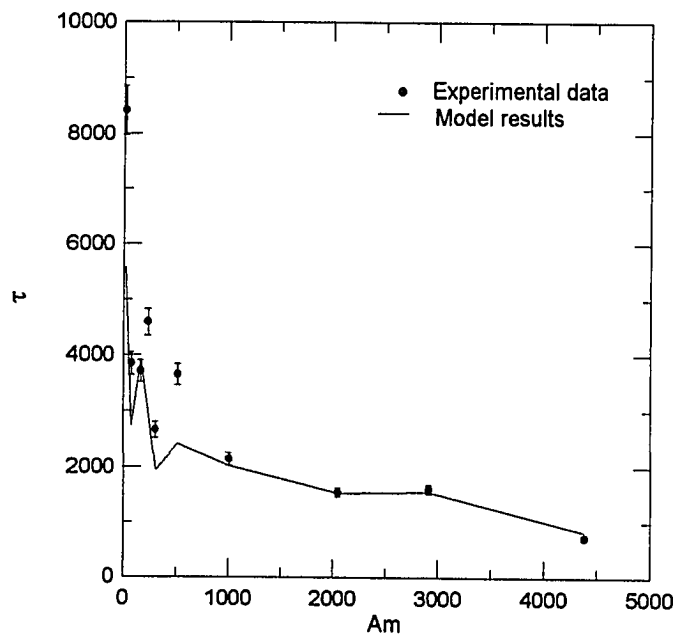


Figure 7.17 The freezing time: Comparison of the experimental and numerical results.

CHAPTER VIII

CONCLUSIONS AND RECOMMENDATIONS

8.1 Background and Statement of the Problem

Frost layer has been shown by numerous investigators to be a detrimental problem for insulating heat transfer from a cold surface. Consequently, a considerable amount of work has been conducted to obtain information on heat transfer rates for use in the design of heat exchangers. The chief conclusions that could be reached from a study of all of these investigations, however, were that frost was a complicated phenomenon. The factors which must be considered include such things as heat exchanger surface material and surface shape, the coating(or promoter) used on the surface, the thermal and flow parameters of ambient air(i.e., relative humidity, velocity, and temperature), and many unknowns involving the presence of non-condensable gases.

In spite of all the work that has been done, no basic microscopic mechanism of frost formation for dropwise condensation has been investigated. In this study, attempts to establish such a microscopic mechanism of frost formation have been concentrated around analysis of the freezing of single droplets, but these analyses have based on pure conduction and constant thermophysical property assumptions. These restrictive conditions ensured that the investigation center on energy equation and avoid the time-consuming calculation of velocity field. The analysis has not taken the entire frost

formation process into account, and have focused on the important phase change process.

The object of this investigation was to see if the basic mechanism of frost formation could be better understood by a more comprehensive and transient single droplet analysis. The temperature field and the freezing of a hemispherical droplet sitting on a cold surface have been studied both experimentally and mathematically. The conclusions drawn from this study were presented and discussed in this chapter. The limitations and drawbacks of the investigation as well as recommendations for future work were also presented.

8.2 Mathematical and Experimental Investigations

The basic system considered in this study included a hemispherical droplet and a cold plate on which it was resting. The temperature and velocity of the air above the droplet and the surface temperature of the cold plate were specified, but all temperatures with the droplet during phase transition were determined only by the basic energy conservation equations. The mass transfer to the droplet was neglected so that the size of a droplet did not change. The transient heat conduction equations were used to calculate temperature distributions and heat flows through the boundaries of the droplet during freezing.

The equations necessary to describe this phase change problem were too complicated for analytical solution. Consequently, a finite-difference method was adopted.

The experimental investigation was designed to measure the temperature distribution, temperature history, air-side convection coefficient, and to visualize the freezing process. Both data and image acquisition systems were employed to record and to analyze the experimental data.

8.3 Mathematical Model

A mathematical model to simulate the temperature field for a hemispherical droplet under different conditions has been developed. The results predicted by the mathematical model have been compared with previously published results and experimental data. The good agreements indicated that the model could be used to predict steady-state and transient temperature distribution, temperature history, freezing front velocity, and freezing time. Combined with some visualization software, the mathematical model could also be used to simulate the freezing process.

The numerical analysis indicated a large heat-transfer rate around the droplet perimeter. Unfortunately, limitations on the experimental apparatus prevented the direct measurement of the heat transfer rate in this sensitive region. However, this conclusion gave a logical explanation for the mechanism of the dropwise condensation on a cold metal plate. The action of diffusing heat laterally underneath and around a droplet made

the perimeter area a favorite place for continuous condensation. If the droplets on a cold metal plate could not be removed by the action of gravity or drag force, the high growth rate at the base of a droplet promoted the coalescence among droplets. Therefore, the cold metal plate would be covered by a thin layer of condensate film, which totally inactivated the dropwise promotion of the special coating.

The mathematical simulation of the freezing of a hemispherical droplet showed that the narrow ring around the droplet perimeter was a good place for continued ice nucleation. The ice deposit around the droplet perimeter would form a layer of ice on the cold surface. This lateral growth of ice encouraged a new understanding of frost formation. The frost layer was divided into two zones: the ice sublayer and the dendritic zone. At positions close to the cold plate in the ice sublayer, the continuous condensate deposition was frozen to ice. The thermophysical properties of this zone were exactly the same as those of ice. In the dendritic zone, the freezing rate of the condensate deposition was much slower than that of the ice sublayer. The slow freezing allowed that a dendritic frost structure was formed. It was a porous material and increased the thickness of frost very fast. All of the properties in this zone should be significantly different from those of ice.

8.4 Experimental Work

The proposed experimental work was performed on the test setup at Energy System Laboratory. In general, the experimental results could be said to have followed

the expected trend. Specific comparisons of the experimental and numerical results were conducted in Chapter VII, but it was worth noting here that the agreement between them was fairly close. Some generalized conclusions might be reiterated in this chapter.

Freezing time was a strong function of the size of droplet and the ambient conditions. The important factors included the plate surface temperature, the velocity and the temperature of ambient air, and the radius of droplet.

The two new introduced dimensionless numbers, Am and τ , reduced effectively the number of variables and presented the experimental results in a good shape.

The following empirical relation was recommended for calculating the freezing time of a hemispherical water droplet sitting on a cold plate:

$$\tau = 10^{-1.332} Am_{\infty}^{-0.141} Re_{\infty}^{0.649} Ste_L^{-0.898} \quad (8.1)$$

$$20 < Am_{\infty} < 4 \times 10^4$$

$$20 < Re_{\infty} < 300$$

$$8 \times 10^{-5} < Ste_L < 2 \times 10^{-4}$$

The following empirical correlation was recommended for calculating the average air-side convection coefficient for a cold surface covered with condensate droplets:

$$\text{Nu}_\infty = 10^{6.094} \text{Re}_\infty^{-1.238} \text{Am}_\infty^{-0.478} \quad (8.2)$$

$$20 < \text{Re}_\infty < 1000$$

$$3 < \text{Am}_\infty < 1000$$

The above correlations assumed that the net mass transferred at the surface of droplets equaled to zero. The analysis failed to consider nonequilibrium interactions between the mass evaporating from the droplet surfaces and that condensing to the droplet surfaces. Inclusion of this effects made analysis of this problem considerably more difficult.

8.5 Recommendations for Further Research

The macroscopic mechanism of frost formation is still not well understood. There are some recommendations for future work that can be based on the present investigations.

1. It is necessary to make a more thorough investigation of the dropsize distribution, which is the bridge connecting the microscopic and macroscopic phenomena. As a result, the total heat transferred through a heat exchanger surface covered with condensate droplets or frost layer could be determined.

2. The ultimate goal of the mathematical model would be to predict the frost growth rate, density, thermal conductivity, and other thermophysical properties at different ambient air conditions. It may be useful to consider extending the mathematical model to the dendritic zone.
3. Work should be undertaken to better measure the air-side convection coefficient in the presence of condensate or frost. This coefficient is a major input in modeling the freezing of condensate droplets. The data currently available showed a wide variation in value and was not suitable for the operating range of most heat pumps.
4. It should also be noted that the mathematical model developed in this study is not limited to the analysis of hemispherical droplets in spherical coordinates. Some test problems in cylindrical and rectangular coordinates have been solved and compared with the results reported in the previous published papers. The good agreements of the comparisons and the flexibility of the mathematical model enhance the credibility to the numerical simulation. It would be predicted that the mathematical model can be applied to the melting and liquid-vapor phase-change problems.

NOMENCLATURE

a	= coefficient in the discretization equation	S	= displacement of the freezing front
Am	= dimensionless number = $k_{\infty}(T_{\infty}-T_w)/(\rho V^3 D)$	t	= time
b	= constant term in the discretization equation	T	= temperature
C	= heat capacity	T_v	= ambient vapor temperature
D	= characteristic length	u	= anemometer output voltage
f_s	= the area fraction of solid	U	= Uncertainty of a variable
Fo	= Fourier number = $\alpha t/R^2$	V	= velocity
H	= the length of cold metal plate	v_{lv}	= specific volume difference between vapor and liquid
h	= local convection coefficient	x	= distance from the leading edge
\bar{h}	= average convection coefficient	α	= thermal diffusivity
h_{lv}	= latent heat of vaporization per unit mass	θ	= zenith angle in spherical polar coordinate system
i	= index denoting the position in θ	ϕ	= azimuth angle in spherical polar coordinate system
j	= index denoting the position in r	Ω	= computational domain
k	= thermal conductivity	Γ	= boundary of computational domain
h_{sf}	= latent heat of freezing	Ξ	= nondimensional temperature = $(T-T_{\infty})/(T_w-T_{\infty})$
L	= value of I for the boundary grid line	Ξ_1	= nondimensional temperature = $(T_c-T_1)/(T_0-T_1)$
M	= value of J for the boundary grid line	ξ	= unheated starting length
\bar{M}	= molecular weight	ε	= ice thickness
m	= integer	μ	= absolute viscosity
n	= outward normal vector	$\hat{\sigma}$	= accommodation coefficient
\bar{Nu}	= average Nusselt number, = hD/k	τ	= dimensionless freezing time = $(Fo \cdot Pe)_L$
Pe	= Peclet number, = VD/v	δ	= average thickness of the condensate layer
Pr	= Prandtl number, = v/α	ρ	= density
P_v	= ambient vapor pressure	ζ	= an experimental result
q''	= heat flux	β	= absolute sensitivity coefficient
Q	= total heat transfer rate	κ	= constant
St_e	= Stefan number, = $k_s(T_f-T_w)/h_{sf}$		
r	= radial distance in spherical polar coordinate system		
\bar{R}	= universal gas constant		
Re	= Reynolds number		

NOMENCLATURE (CONTINUED)**Subscripts**

a	=	apparent	t	=	time
c	=	central	V	=	velocity
D	=	diameter	q''	=	heat flux
eff	=	effect	w	=	surface
f	=	freezing point	∞	=	ambient air
i	=	interface	θ	=	θ direction
j	=	variable	ϕ	=	phase-change region or ϕ direction
L	=	liquid	$L\phi$	=	boundary between liquid and two-phase region
P	=	constant pressure	$S\phi$	=	boundary between solid and two-phase region
nb	=	general neighbor grid point			
o	=	initial value			
r	=	radial direction			
S	=	solid			
T	=	temperature			

Superscripts

0	=	old value
n	=	n th iteration

REFERENCES

- Bathelt, A. G., Viskanta, R., 1979, " An Experimental Investigation of Natural Convection in the Melted Region around a Heated Horizontal Cylinder," *Journal of Fluid Mechanics*, Vol. 90, Part 2, pp.227-239.
- Baxter, D. C., 1962, "The Fusion Times of Slabs and Cylinders," *ASME Journal of Heat Transfer*, Vol. 84, pp.317-326.
- Boger, D. V., and Westwater, J. W., 1967, "Effect of Buoyancy on the Melting and Freezing Process," *ASME Journal of Heat Transfer*, Vol. 89, pp. 81-89.
- Brian, P. L. T., Reid, R. C., Brazinsky, I., 1969, "Cryogenic Frost Properties," *Cryogenic Technology*, September/October, pp.205-212.
- Brian, P. L. T., Reid, C. R., and Shah, Y. T., 1970, "Frost Deposition on Cold Surfaces," *Ind. Eng. Chem. Fundam.*, Vol.9, No.3, pp.375-380.
- Bryant, J. A., 1995, "Effects of Hydrophobic Surface Treatments on Dropwise Condensation and Freezing of Water," Ph.D. Dissertation, Texas A&M University, College Station.
- Bushko, W., and Grosse, I. R., 1991, " New Finite Element Method for Multidimensional Phase Change Heat Transfer Problems," *Numerical Heat Transfer*, Part B, Vol.19, pp.31-48.
- Cames-Pintaux, A. M., and Nyuyen-Lamba, M., 1986, " Finite-Element Enthalpy Method for Discrete Phase Change," *Numerical Heat Transfer*, Part B, Vol. 9, pp.403-417.
- Carre, P., and Delaunay, D., 1985, "Simultaneous Measurement of the Thermal Properties of Phase-Change Material and Complex Liquid Using a Nonlinear Thermocinetic Model," *Measurement Techniques in Heat and Mass Transfer*, Edited by Soloukhin, R.I. and Afgan, N., Hemisphere Publishing Corporation, pp. 279-293, Washington, D. C..
- Carslaw, H. S., and Jaeger, J. C., 1959, *Conduction of Heat in Solids*, Oxford University Press, London.
- Chen, C. S., 1988, " Systematic Calculation of Thermodynamic Properties of an Ice-Water Systems at Subfreezing Temperatures," *Transactions of the ASAE*, Vol. 31 pp.1602-1606.

Chiang, C. H., Raju, M. S., Sirignano, W. A., 1992, "Numerical Analysis of Convecting, Vaporizing Fuel Droplet with Variable Properties," *Int. J. Heat Mass Transfer*, Vol. 35, pp. 1307-1324.

Crank, J., 1981, "How to Deal with Moving Boundaries in Thermal Problems," *Numerical Methods in Heat Transfer*, Edited by Lewis, R. W., Morgan, K., and Zienkiewicz, O. C., John Wiley & Sons Ltd., New York.

Cremers, C. J. and Mehra, V. K., 1980, "Frost Formation on Vertical Cylinders in Free Convection," ASME Papers, 80-WA/HT-22.

Crowley, A. B., 1978, "Numerical Solution of Stefan Problems," *Int. J. Heat Mass Transfer*, Vol. 21, pp.215-219.

Dorsey, N. E., 1947, "The Freezing of Supercooled Water," *Trans. Am. Phil. Soc.*, Vol.38, pp.248-328.

Flemings, M. C., 1974, *Solidification Processing*, McGraw-Hill, Inc., New York.

Gau, C. and Viskanta, R., 1986, "Melting and Solidification of a Pure Metal on a Vertical Wall," *ASME Journal of Heat Transfer*, Vol. 108, pp.174-181.

Ghosh, S., and Moorthy, S., 1993, "An Arbitrary Lagrangian-Eulerian Finite Element Model for Heat Transfer Analysis of Solidification Processes," *Numerical Heat Transfer*, Part B, Vol.23, pp.327-350.

Gong, Y., Bryant, J. A., and O'Neal, D. L., 1995, "Heat Transfer and Temperature Distribution of a Water Droplet during Phase Transition," *The Proceedings of the 30th National Heat Transfer Conference*, Portland, Oregon, Vol. 11, pp.65-79.

Goodman, T. R., 1961, "The Heat-Balance Integral-Further Considerations and Refinements," *ASME Journal of Heat Transfer*, Vol. 83, pp.83-86.

Gupta, S. C., 1987, "Analytical and Numerical Solutions of Radially Symmetric Inward Solidification Problems in Spherical Geometry," *Int. J. Heat Mass Transfer*, Vol. 30, No.12, pp.2611-2616.

Hale, N. W. Jr., and Viskanta, R., 1980, "Solid-Liquid Phase-Change Heat Transfer and Interface Motion in Materials Cooled or Heated from Above or Below," *Int. J. Heat Mass Transfer*, Vol. 23, pp.283-292.

Hashemi, H. T., and Sliepcevich, C. M., 1967, "A Numerical Method for Solving Two-Dimensional Problems of Heat Conduction with Change of Phase," *Chemical Engineering Process Symposium Series*, Vol. 63, pp.34-41.

Hayashi, Y., and Aoki, A., 1977, "Study of Frost Properties Correlating with Frost Formation Types," *ASME Journal of Heat Transfer*, Vol. 99, May, pp.239-249.

Incropera, F. P., and Dewitt, D. P., 1990, *Fundamental of Heat and Mass Transfer*, John Wiley & Sons Ltd., New York.

Huffman, G. D. and Sepsy C. F., 1967, "Heat Transfer and Pressure Loss in Extended Surface Heat Exchangers Operating under Frosting Conditions--Pt.2," *ASHRAE Transactions*, Vol. 73, Pt.2.

Hurst, C. L., 1966, "Transient Droplet Growth During Dropwise Condensation," M. Sc. thesis, Penn State University, University Park.

Hurst, C. L., 1973, "Conduction through Droplets during Dropwise Condensation," *ASME Journal of Heat Transfer*, Vol. 95, pp.12-20.

Knight, C. A., 1967, *The Freezing of Supercooled Liquids*, D. Van Nostrand Company, Princeton.

Kondepudi, S. N., 1988, "The Effects of Frost Growth on Finned Tube Heat Exchangers under Laminar Flow," Ph. D. Dissertation, Texas A&M University, College Station.

Lane, G., A., 1983, *Solar Heat Storage: Latent Heat Material*, Vol.I, CRC Press, Boca Raton, Florida.

Lemmon, E.C., 1981, "Multidimensional Integral Phase Change Approximations for Finite Element Conduction Codes," *Numerical Methods in Heat transfer*, Edited by Lewis, R.W. and Zienkiewicz, O.C., John Wiley & Sons Ltd., New York.

Lorenz, J., and Mikic, B., 1970, "The Effect of Thermocapillary Flow on Heat Transfer in Dropwise Condensation," *ASME Journal of Heat Transfer*, Vol. 92, pp.46-52.

Mao, Y., Besant, R. W., and Rezkallah, K. S., 1991, "A Method of Measuring Frost Density Using Flush-Mounted Removable Disks," *ASHRAE Transactions*, Vol. 97, Pt. 1, pp.26-30.

Marinyuk, B. T., 1980, "Heat and Mass transfer under Frosting Conditions," *International Journal of Refrigeration*, Vol. 3, No. 6, Nov. 1980, pp.366-368.

Medjani, K., and Watts, R. G., 1993, "Freezing of the NaCl-H₂O Binary Compound from Above in a Partially Open Cylindrical Geometry, " *ASME Journal of Heat Transfer*, Vol. 115, pp.777-781.

Measurement Uncertainty, 1986, ANSI/ASME, PTC, 19.1-1985, Part 1, Fairfield, New Jersey.

Murray, W. D. and Landis, F., 1959, "Numerical and Machine Solutions of Transient Heat-Conduction Problems Involving Melting or Freezing," *ASME Journal of Heat Transfer*, May, 1959, pp.106-112.

Tables of Thermal Properties of Gases, 1955, National Bureau of Standards Circular 564, Galthersburg, Maryland.

Neilson, D. G., and Incropera, F. P., 1990, " Numerical Simulation of Solidification in a Horizontal Cylindrical Annulus Charged with an Aqueous Salt Solution," *Int. J. Heat Mass Transfer*, Vol.33, No.2, pp.367-380.

Neumann, F., 1912, " Die Partiellen Differentialgleichungen der Mathematischen Physik," Riemann-weber, Vol.2, pp.121.

OMEGA Engineering Inc., 1994, "Chart of Dimensionless Numbers," *OMEGA Measurement Handbook & Encyclopedia*, Stamford, Connecticut.

O'Neal, D. L., 1982, "The Effect of Frost Formation on the Performance of a Parallel Plate Heat Exchanger," Ph.D. Dissertation, Purdue University, West Lafayette.

O'Neal, D. L. , and Tree, D. R., 1982, "Measurement of Frost Growth and Density in a Parallel Plate Geometry," *ASHRAE Transactions*, Vol. 88, Pt. 2, pp.278-290.

O'Neal, D. L. , and Tree, D. R., 1985, "A Review of Frost Formation in Simple Geometries," *ASHRAE Transactions*, Vol. 91, Pt. 2.

Patankar, S. V., 1980, *Numerical Heat Transfer and Fluid Flow*, McGraw-Hill Book Company, New York.

Patankar, S. V., 1991, *Computation of Conduction and Duct Flow Heat Transfer*, Innovative Research, Inc., Maple Grove, Minnesota.

Poirier, D., and Salcudean, M., 1988, "On Numerical Methods Used in Mathematical Modeling of Phase Change in Liquid Metals," *ASME Journal of Heat Transfer*, Vol.110, pp.562-570.

Prakash, S. and Sirignano, W. A., 1978, "Liquid Fuel Droplet Heating with Internal Circulation," *Int. J. Heat Mass Transfer*, Vol.21, pp.885-895.

Runnels, S. R., and Carey, G. F., 1993, " A Domain-Decomposition Strategy for Finite-Element Simulation of Phase Change," *Numerical Heat Transfer*, Part B, Vol. 24, pp.181-189.

Saito, H., and Tokura, I., 1991, "Heat and Mass Transfer in the Frosting Process on Cold Surfaces," *Freezing and Melting Heat Transfer in Engineering, Selected Topics on Ice-water Systems and Welding and Casting Processes*, Chapter 13, Edited by Cheng, K.C. and Seki, N., Hemisphere Publishing Corporation, New York.

Salcudean, M., and Abdullah, Z., 1986, " Numerical Simulation of Casting Process," *Proceedings of the VIII International Heat Transfer Conference and Exhibition*, San Francisco, CA, pp.459-464.

Samarskii, A. A., Vabishchevich, P. N., Iliev, O. P., and Churbanov, A. G., 1993, "Numerical Simulation of Convection/Diffusion Phase Change Problems--a Review," *Int. J. Heat Mass Transfer*, Vol.36, No.17, pp.4095-4106.

Schneider, H. W., 1978, "Equation of the Growth Rates of Frost Forming on Cooled Surfaces," *Int. J. Heat Mass Transfer*, Vol.21, pp.1019-1024.

Scott, C. J., (1976), " Transient Experimental Techniques for Surface Heat Flux rates," *Measurement in Heat Transfer*, 2nd Edition, Edited by Eckert, E.R. and Goldstein, R.J., Hemisphere Publishing Corporation, pp. 375-396, Washington, D. C..

Shamsundar, N. , and Sparrow, E. M., 1975, " Analysis of Multidimensional Conduction Phase Change Via the Enthalpy Model," *ASME Journal of Heat Transfer*, Vol. 97, pp. 333-340.

Shih, T. M., and Chen, Y. N., 1983, "Comparison of Finite Difference Method and Finite Element Method," *Numerical Properties and Methodologies in Heat Transfer*, Edited by Shih, T. M., Hemisphere Publishing Corporation, Washington, D. C..

Silver, R. S., and Simpson, H. C., 1961, " The Condensation of Superheated Steam," *Proceedings of a Conference Held at the National Engineering Laboratory*, Glasgow, Scotland.

Smith, G. D., 1978, *Numerical Solution of Partial Differential Equations—Finite Difference Methods*, 2nd ed., Clarendon Press, Oxford.

Schneider, P.J., 1955, *Conduction Heat Transfer*, Addison-Wesley Publishing Company, Inc., Cambridge, Massachusetts.

Sparrow, E. M., et al, 1979, " Freezing Controlled by Natural Convection," *ASME Journal of Heat Transfer*, Vol. 101, pp.578-584.

Sparrow, E. M., et al, 1981, " The Transition from Natural-Convection-Controlled Freezing to Conduction-Controlled Freezing," *ASME Journal of Heat Transfer*, Vol. 103, pp.7-12.

Stoecker, W. F., 1960, "Frost Formation on Refrigeration Coils," *ASHRAE Transactions*, Vol.66, pp.71-103.

Tantakitti, C. and Howell R. H., 1986, "Air to Air Heat Pumps Operating under Frosting Conditions on the Outdoor Coil," *ASHRAE Transactions*, Vol.92, Pt.1.

Tao, Luh C., 1967, " Generalized Numerical Solutions of Freezing a Saturated Liquid in Cylinders and Spheres," *A. I. Ch. E. Journal*, Vol.13, No. 1, pp165-169.

Tao, Y. X., Besant, R. W., and Mao, Y., 1993, "Characteristics of Frost Growth on a Flat Plate During the Early Growth Period," *ASHRAE Transactions*, Vol. 99, Pt. 1.

Tao, Y. X., Besant, R. W., and Rezkallah, 1992, "A Mathematical Model for Predicting the Densification and Growth of Frost on a Flat Plate," *Int. J. Heat Mass Transfer*, Vol.35, No.16.

Thomas, L. J., and Westwater, J. W., 1963, "Microscopic Study of Solid-Liquid Interfaces during Melting and Freezing," *A. I. Ch. E., Chemical Engineering Progress Symposium Series*, Vol.59, pp.155-164.

Tanasawa, I., 1978, " Dropwise Condensation: The way to Practical Applications, " *Proceedings of the 6th International Heat Transfer Conference*, Toronto, Canada.

Trefethen, L., 1958, " Dropwise Condensation and the Possible Importance of Circulation Within Drops Caused by Surface Tension Variation , " Report, General Electric Co., No. 58GL47, Schenectady, New York.

Umur, A. and Griffith, P., 1965, " Mechanism of Dropwise Condensation," *ASME Journal of Heat Transfer*, Vol.87, pp.275-282.

Vick, B., and Nelson, D. J., 1993, " The Boundary Element Method Applied to Freezing and Melting Problems," *Numerical Heat Transfer*, Part B, Vol.24, pp.263-277.

Vliet, G. C. and Leppert, G., 1961, "Forced Convection Heat Transfer fro An Isothermal Sphere to Water," *ASME Journal of Heat Transfer*, May 1961, pp.163-175.

Voller, V. R., and Prakash, C., 1987, " A Fixed Grid Numerical Modeling Methodology for Convection-Diffusion Mushy Region Phase-Change Problems," *Int. J. Heat Mass Transfer*, Vol.30, No.8, pp.1709-1719.

Whitaker, S., 1972, "Forced Convection Heat Transfer Correlations for Flow in Pipes, Past Flat Plates, Single Cylinders, Single Spherers, and for Flow in Packed Beds and Tube Bundles," *A. I. Ch. E. Journal*, Vol.18, No.2, pp.361-371.

Witte, L.C., 1968, "An Experimental Study of Forced-Convection Heat Transfer from a Sphere to liquid Sodium," *ASME Journal of Heat Transfer*, Vol.90, pp.9-12.

Yonko, J. D., and Sepsy, C. F., 1967, "An Investigation of the Thermal Conductivity of Frost while Forming on a Flat Horizontal plate," *ASHRAE Transactions*, Vol. 73, pp.I.1.1-I.1.9.

Yuge, T., 1960, "Experiments on Heat Transfer from Sphere Including Combined Natural and Forced Convection," *ASME Journal of Heat Transfer*, August, 1960, pp.214-220.

APPENDIX A

EXPERIMENTAL DATA

Table A.1 Experimental Results for Freezing of Hemispherical Water Droplets*

No.	T_{∞} (°C)	T_w (°C)	V_{∞} (m/s)	R (mm)	t (sec)	τ	Am_{∞}	Re_{∞}	Ste_L	U_t	U_{Am}	U_{Re}	U_{Ste}
1	10.8	-9.6	0.56	1.1	8.0	2136.14	1003.17	89.21	1.14E-4	111.03	166.39	4.67	7.91E-6
2	10.9	-8.9	0.82	1.0	6.7	2697.67	332.12	124.19	1.10E-4	140.61	55.45	6.52	7.91E-6
3	10.8	-8.7	1.02	1.0	7.5	3704.72	165.98	157.65	1.09E-4	192.84	27.77	8.27	7.91E-6
4	10.9	-9.1	0.84	1.1	7.3	2917.10	298.30	131.99	1.12E-4	151.68	49.69	6.92	7.91E-6
5	10.8	-8.8	0.63	1.1	7.5	2201.33	679.07	101.02	1.10E-4	114.30	113.43	5.29	7.91E-6
6	10.9	-9.3	0.44	1.1	7.4	1542.12	2048.27	70.19	1.13E-4	80.13	340.47	3.68	7.91E-6
7	15.5	-8.5	0.42	1.1	8.2	1599.79	2912.09	65.75	1.35E-4	83.08	471.10	3.44	7.91E-6
8	15.5	-7.7	0.55	1.1	8.7	2197.02	1235.18	87.40	1.30E-4	113.94	200.77	4.57	7.91E-6
9	15.6	-8.5	0.74	1.2	8.3	2664.73	483.44	126.08	1.35E-4	137.65	78.16	6.56	7.91E-6
10	15.6	-11.4	0.45	0.6	2.0	723.85	4403.80	41.82	1.51E-4	40.19	707.99	2.34	7.91E-6
11	15.5	-11.1	0.46	0.6	1.8	719.03	4384.09	40.02	1.49E-4	40.42	706.73	2.26	7.91E-6
12	15.3	-11.0	0.37	0.6	2.5	737.09	8064.97	33.80	1.47E-4	40.94	1300.39	1.89	7.91E-6
13	18.1	-10.6	0.34	0.7	2.9	760.18	10268.80	32.79	1.60E-4	41.88	1639.65	1.82	7.91E-6
14	20.9	-10.8	0.33	0.7	3.4	822.88	13344.73	31.38	1.77E-4	45.15	2111.20	1.73	7.91E-6
15	28.9	-9.8	0.26	0.9	6.5	973.86	24014.15	32.53	2.17E-4	51.48	3731.73	1.73	7.91E-6
16	29.1	-9.7	0.26	0.9	6.7	1023.98	23920.69	32.45	2.17E-4	54.16	3717.12	1.73	7.91E-6
17	29.1	-9.3	0.25	0.6	3.1	668.05	43677.88	20.06	2.15E-4	37.69	6844.61	1.14	7.91E-6
18	28.0	-8.8	0.26	1.1	3.6	434.98	19956.72	38.65	2.06E-4	22.61	3104.39	2.02	7.91E-6
19	21.2	-9.0	0.31	1.1	10.2	1470.68	8813.53	48.87	1.69E-4	76.31	1390.95	2.55	7.91E-6
20	18.0	-9.3	0.33	1.1	10.7	1628.42	6500.90	53.04	1.52E-4	84.43	1036.25	2.77	7.91E-6
21	15.2	-9.2	0.36	1.1	10.7	1798.93	4476.86	57.76	1.36E-4	93.34	723.04	3.02	7.91E-6
22	3.9	-12.3	1.31	0.8	4.9	3843.12	79.26	167.58	9.09E-5	204.29	13.83	8.98	7.91E-6
23	4.0	-11.9	1.31	1.2	10.0	5658.01	55.88	232.57	8.89E-5	292.26	9.78	12.11	7.91E-6
24	3.9	-10.9	1.32	1.6	18.4	7506.04	36.19	327.84	8.29E-5	381.69	6.45	16.81	7.91E-6
25	4.0	-11.3	1.32	1.1	8.7	5454.40	57.01	214.16	8.60E-5	283.60	10.07	11.22	7.91E-6
26	4.0	-10.9	1.88	0.6	4.0	5986.90	32.41	182.14	8.35E-5	331.39	5.80	10.15	7.91E-6
27	4.0	-11.0	1.87	0.8	5.7	6929.72	27.18	219.58	8.38E-5	372.23	4.85	11.88	7.91E-6
28	4.1	-10.3	1.87	1.0	8.5	8309.50	21.00	272.52	8.03E-5	435.62	3.79	14.40	7.91E-6
29	4.0	-10.2	1.87	1.0	8.6	8422.67	20.65	272.98	7.93E-5	441.56	3.74	14.42	7.91E-6
30	10.1	-11.5	0.91	0.7	3.6	2429.77	392.38	92.13	1.21E-4	133.15	64.86	5.08	7.91E-6
31	10.1	-11.4	0.90	0.8	4.9	2932.71	354.73	103.41	1.20E-4	157.67	58.57	5.60	7.91E-6
32	10.2	-10.0	0.90	1.0	9.3	4106.68	249.52	138.52	1.13E-4	213.96	41.50	7.27	7.91E-6
33	10.3	-9.9	0.91	0.8	5.7	3321.18	325.65	105.48	1.13E-4	178.02	54.30	5.69	7.91E-6
34	10.3	-9.6	0.90	0.9	7.2	3698.31	288.04	118.35	1.11E-4	195.44	48.11	6.30	7.91E-6
35	10.0	-9.4	1.00	0.9	7.3	4103.42	205.77	132.38	1.09E-4	216.66	34.48	7.04	7.91E-6
36	10.3	-9.2	1.01	0.6	3.1	2660.05	308.30	87.20	1.09E-4	149.80	52.01	4.94	7.91E-6
37	10.1	-8.1	1.00	0.7	6.7	4589.20	233.83	108.54	1.02E-4	248.23	39.80	5.91	7.91E-6
38	10.3	-8.0	1.01	0.5	3.5	3381.20	322.27	77.75	1.02E-4	195.47	55.21	4.52	7.91E-6
39	10.2	-8.4	1.00	0.6	5.3	4193.39	273.50	94.22	1.04E-4	232.26	46.49	5.25	7.91E-6
40	10.2	-8.3	1.00	0.7	5.0	3870.60	266.25	96.83	1.03E-4	213.18	45.29	5.37	7.91E-6

Table A.1 Continued

No.	$T_a(^{\circ}\text{C})$	$T_w(^{\circ}\text{C})$	$V_w(\text{m/s})$	$R(\text{mm})$	$t(\text{sec.})$	τ	Am_w	Re_w	Ste_L	U_c	U_{Am}	U_{Re}	U_{Ste}
41	10.2	-8.7	0.72	0.9	9.1	3509.14	521.11	98.98	1.06E-4	184.42	87.79	5.24	7.91E-6
42	10.3	-8.4	0.71	0.9	9.7	3644.23	518.18	99.82	1.05E-4	191.23	87.47	5.28	7.91E-6
43	10.2	-8.5	0.71	0.9	8.1	3223.13	553.05	94.00	1.04E-4	170.08	93.44	5.00	7.91E-6
44	10.2	-7.8	0.71	0.9	9.1	3562.44	524.11	95.43	1.01E-4	187.66	89.23	5.06	7.91E-6
45	10.2	-8.2	0.70	0.8	7.6	3190.44	613.18	86.30	1.03E-4	169.58	104.04	4.62	7.91E-6
46	10.2	-8.3	0.70	0.9	9.6	3620.64	545.19	96.88	1.03E-4	190.23	92.26	5.13	7.91E-6
47	10.2	-8.3	0.70	0.8	7.9	3454.69	641.08	83.04	1.04E-4	184.49	108.64	4.47	7.91E-6
48	17.2	-8.1	0.36	0.5	2.0	737.19	10322.83	26.03	1.42E-4	43.20	1682.52	1.53	7.91E-6
49	18.0	-7.5	0.37	0.5	1.7	694.75	10674.45	24.58	1.43E-4	41.52	1742.86	1.48	7.91E-6
50	16.7	-8.6	0.37	0.5	2.0	798.21	10052.70	25.60	1.42E-4	47.32	1640.95	1.53	7.91E-6
51	16.7	-8.9	0.37	0.6	2.7	847.96	7996.73	32.09	1.43E-4	47.63	1294.89	1.81	7.91E-6
52	16.7	-6.8	0.38	0.7	3.7	1050.74	6128.38	37.25	1.32E-4	57.51	999.85	2.05	7.91E-6
53	16.6	-6.8	0.38	0.7	4.1	1165.11	6221.16	36.53	1.31E-4	63.97	1016.20	2.02	7.91E-6
54	16.7	-6.1	0.37	0.7	4.5	1288.42	6464.92	35.32	1.28E-4	70.92	1060.32	1.96	7.91E-6
55	16.6	-7.0	0.36	0.6	3.9	1172.33	8394.62	30.93	1.32E-4	65.61	1373.15	1.74	7.91E-6
56	16.5	-7.4	0.36	0.5	3.4	1109.72	9231.43	28.26	1.34E-4	63.43	1511.25	1.62	7.91E-6
57	16.4	-6.2	0.37	0.8	6.8	1685.49	5493.31	40.94	1.26E-4	90.73	899.90	2.22	7.91E-6
58	7.5	-10.1	0.49	0.6	2.8	1170.14	2295.88	44.00	9.85E-5	65.67	395.17	2.48	7.91E-6
59	7.2	-8.6	0.67	0.7	3.9	1952.89	746.81	66.23	8.80E-5	107.29	131.77	3.66	7.91E-6
60	7.1	-8.6	0.67	0.7	3.7	1823.04	720.67	68.29	8.76E-5	99.66	127.23	3.76	7.91E-6
61	7.0	-9.0	0.67	0.7	4.0	1933.49	713.58	69.64	8.91E-5	105.44	125.41	3.82	7.91E-6
62	7.1	-9.3	0.67	0.7	3.6	1741.13	739.66	69.56	9.19E-5	94.96	128.99	3.82	7.91E-6
63	7.2	-8.3	0.67	0.7	3.7	1746.57	686.19	70.37	8.64E-5	95.04	121.54	3.86	7.91E-6
64	6.7	-9.6	0.66	0.8	4.2	1701.16	635.91	81.45	9.11E-5	90.70	110.88	4.37	7.91E-6
65	6.7	-9.8	0.66	0.9	4.5	1756.42	617.63	85.26	9.22E-5	93.13	107.34	4.55	7.91E-6
66	6.5	-10.5	0.66	0.9	4.7	1747.94	607.27	88.84	9.51E-5	92.33	104.71	4.73	7.91E-6
67	7.1	-9.9	0.66	0.9	4.4	1590.85	607.89	89.65	9.47E-5	83.87	104.92	4.76	7.91E-6
68	7.1	-10.1	0.66	0.9	4.7	1675.49	603.58	91.76	9.64E-5	88.13	103.73	4.86	7.91E-6
69	7.1	-9.9	0.66	0.9	3.2	1136.09	588.25	92.64	9.47E-5	59.71	101.50	4.90	7.91E-6
70	7.3	-9.8	0.66	0.9	4.8	1694.89	600.22	92.34	9.58E-5	89.06	103.26	4.89	7.91E-6
71	6.8	-8.6	0.67	1.0	9.0	2952.38	467.03	102.89	8.65E-5	153.90	82.37	5.41	7.91E-6
72	7.0	-8.8	0.67	1.0	8.3	2721.94	482.22	102.83	8.85E-5	141.85	84.55	5.40	7.91E-6
73	7.5	-9.7	0.65	1.0	6.1	1943.67	549.12	101.78	9.59E-5	101.23	94.38	5.34	7.91E-6
74	6.9	-8.3	0.67	1.0	9.0	2909.16	454.63	104.10	8.48E-5	151.47	80.62	5.46	7.91E-6
75	6.9	-9.1	0.67	1.0	8.1	2603.39	474.75	104.99	8.93E-5	135.49	83.03	5.51	7.91E-6
76	6.9	-8.4	0.67	1.0	8.9	2866.77	450.32	105.28	8.54E-5	149.17	79.68	5.52	7.91E-6
77	7.0	-8.4	0.67	1.1	10.6	3158.20	427.47	112.78	8.61E-5	163.46	75.45	5.88	7.91E-6
78	7.0	-8.4	0.67	1.1	10.4	3075.86	425.95	113.18	8.61E-5	159.16	75.18	5.90	7.91E-6
79	7.1	-10.3	0.66	1.1	7.8	2236.89	496.02	113.36	9.71E-5	115.66	84.95	5.91	7.91E-6
80	6.8	-9.6	0.67	1.2	10.6	2880.73	409.18	124.54	9.17E-5	148.28	71.01	6.46	7.91E-6
81	6.7	-9.6	0.66	1.3	11.0	2847.15	405.31	127.79	9.11E-5	146.26	70.43	6.62	7.91E-6
82	6.7	-9.8	0.66	1.3	11.5	2914.84	394.55	131.87	9.22E-5	149.52	68.37	6.82	7.91E-6
83	6.9	-9.6	0.66	1.3	12.2	3029.01	389.57	133.76	9.19E-5	155.24	67.55	6.91	7.91E-6
84	6.7	-9.6	0.66	1.4	13.7	3317.40	376.36	137.62	9.11E-5	169.79	65.38	7.10	7.91E-6
85	7.3	-9.6	0.66	1.5	13.1	2792.23	354.30	153.30	9.46E-5	142.24	60.98	7.87	7.91E-6

Uncertainty values are for $U \approx B$ and are at a 95% confidence level.

Table A.2 Experimental Results for Heat Transfer from a Horizontal Plate Covered with Droplets*

No.	T_{∞} (°C)	T_w (°C)	q'' (W/m ² K)	V_{∞} (m/s)	Nu_{∞}	Re_{∞}	Am_{∞}	U_h (W/m ² K)	U_{Nu}	U_{Re}	U_{Am}
1	21.01	-0.57	369.71	0.62	20.95	1301.13	60.29	1.43	1.73	65.56	9.87
2	21.15	-0.32	385.06	0.74	22.25	1558.27	34.41	1.52	1.84	78.52	5.64
3	21.26	-0.19	397.17	0.83	22.95	1756.79	23.96	1.57	1.90	88.52	3.93
4	20.99	-0.15	405.33	0.93	23.48	1956.79	17.29	1.62	1.96	98.60	2.84
5	21.28	-0.08	406.23	1.00	23.55	2108.61	13.80	1.62	1.95	106.25	2.26
6	21.11	0.04	412.00	1.13	23.87	2384.67	9.53	1.66	2.00	120.15	1.57
7	20.98	0.06	426.01	1.21	25.17	2540.00	7.75	1.75	2.12	127.98	1.28
8	21.03	0.20	435.20	1.32	25.62	2767.54	6.00	1.79	2.16	139.45	0.99
9	21.13	0.24	439.03	1.41	26.09	2957.85	4.87	1.82	2.20	149.04	0.80
10	21.27	0.36	455.32	1.63	26.99	3436.50	3.11	1.88	2.27	173.15	0.51
11	37.71	0.76	510.96	0.30	16.40	603.42	932.88	0.88	1.03	30.38	144.48
12	38.04	1.24	533.01	0.38	17.34	758.79	461.28	0.93	1.10	38.20	71.46
13	34.96	1.38	554.67	0.42	19.06	833.24	333.64	1.06	1.25	41.95	52.00
14	37.49	1.70	596.61	0.49	19.90	978.97	209.44	1.08	1.27	49.29	32.50
15	37.92	2.04	597.48	0.56	19.72	1104.80	146.25	1.07	1.26	55.62	22.69
16	36.80	2.55	639.99	0.68	21.99	1358.46	75.77	1.21	1.43	68.39	11.79
17	37.66	1.98	684.06	0.82	22.65	1632.54	45.25	1.23	1.45	82.19	7.02
18	37.90	2.44	719.15	0.93	23.99	1853.28	30.56	1.31	1.54	93.30	4.75
19	37.08	2.79	743.77	1.16	25.72	2306.08	15.36	1.42	1.67	116.10	2.39
20	37.77	3.02	770.41	1.23	26.42	2436.80	13.06	1.45	1.70	122.68	2.03
21	37.30	3.22	780.38	1.38	27.25	2728.81	9.15	1.51	1.77	137.38	1.42
22	37.85	4.40	917.28	2.38	32.27	4697.09	1.75	1.81	2.12	236.45	0.27
23	30.08	1.07	483.71	0.32	19.99	643.30	630.95	1.17	1.40	32.40	99.56
24	30.31	1.21	485.50	0.39	20.04	802.44	324.81	1.18	1.40	40.41	51.24
25	29.79	1.39	500.01	0.43	21.12	883.29	238.49	1.25	1.49	44.49	37.71
26	29.92	1.48	534.61	0.72	22.71	1473.51	51.06	1.35	1.60	74.21	8.07
27	30.05	1.80	555.20	0.82	23.78	1680.52	34.04	1.42	1.68	84.64	5.39
28	29.78	2.13	572.20	1.00	24.66	2038.24	18.90	1.49	1.77	102.65	3.00
29	29.90	2.26	602.08	1.14	26.12	2315.96	12.79	1.57	1.87	116.63	2.03
30	29.75	2.88	641.14	1.51	28.69	3065.83	5.33	1.76	2.08	154.40	0.85
31	30.02	2.73	651.10	1.64	28.90	3325.05	4.21	1.75	2.08	167.45	0.67
32	29.81	3.20	672.53	1.96	30.23	3976.90	2.42	1.86	2.21	200.27	0.39
33	30.04	3.81	747.60	2.61	34.34	5281.85	1.01	2.13	2.53	265.98	0.16
34	11.91	0.29	286.64	0.51	31.31	1107.07	54.17	3.37	4.12	55.81	10.47
35	11.81	0.26	288.85	0.64	31.17	1375.89	28.54	3.37	4.12	69.36	5.53
36	12.05	0.42	306.52	0.73	32.82	1576.28	19.08	3.53	4.32	79.46	3.68
37	11.73	0.39	301.42	0.90	33.78	1941.41	9.80	3.71	4.54	97.86	1.91
38	11.78	0.51	313.65	1.05	35.46	2276.14	6.02	3.91	4.79	114.74	1.18
39	12.20	0.81	328.13	1.26	35.95	2727.83	3.58	3.94	4.81	137.50	0.70

Table A.2 Continued

No.	T_a (°C)	T_w (°C)	q'' (W/m ² K)	V_a (m/s)	Nu_a	Re_a	Am_a	U_h	U_{Nu}	U_{Re}	U_{Am}
								(W/m ² K)			
40	11.71	0.61	326.61	1.48	37.25	3193.79	2.16	4.17	5.10	160.99	0.42
41	12.03	1.01	348.09	1.89	38.95	4086.05	1.04	4.39	5.36	205.96	0.21
42	11.80	1.00	354.09	2.04	41.16	4417.61	0.80	4.72	5.77	222.68	0.16
43	12.13	1.09	360.72	2.41	40.96	5197.83	0.50	4.61	5.63	262.00	0.10
44	11.80	1.44	390.50	3.21	47.08	6929.56	0.20	5.61	6.85	349.29	0.04
45	5.58	0.68	203.52	0.54	54.34	1187.59	18.78	12.90	15.93	59.88	6.12
46	5.59	0.82	202.01	0.67	55.83	1478.09	9.40	13.61	16.81	74.53	3.13
47	5.72	0.85	210.51	0.71	55.10	1571.46	8.24	13.16	16.24	79.24	2.70
48	5.44	0.62	202.17	0.96	54.87	2120.63	3.25	13.22	16.33	106.93	1.07
49	5.43	0.91	212.89	1.19	61.12	2615.68	1.63	15.68	19.37	131.89	0.57
50	5.57	0.84	212.14	1.35	57.81	2986.03	1.16	14.20	17.53	150.57	0.39
51	5.34	0.94	218.86	1.69	64.63	3726.81	0.55	17.02	21.02	187.92	0.19
52	5.65	1.05	230.16	2.02	63.27	4437.00	0.35	15.96	19.70	223.73	0.12
53	5.34	1.02	231.72	2.25	67.83	4948.76	0.24	18.19	22.46	249.53	0.09
54	5.57	1.11	233.43	2.64	64.29	5800.34	0.16	16.71	20.61	292.47	0.05
55	5.36	1.19	237.77	3.46	71.36	7625.12	0.06	19.82	24.47	384.48	0.02

*Uncertainty values are for $U_{\approx B}$ and are at a 95% confidence level.

APPENDIX B

EXPERIMENTAL UNCERTAINTY ANALYSIS

In this investigation, experiments were performed to measure the temperature field for water droplets during freezing and to verify the credibility of the mathematical model. To judge how “good” the experimental data were, an uncertainty analysis was performed on the Re, Nu, Am, τ , air-side convection coefficient, and droplet size.

The uncertainties of the direct measured variables guaranteed by the manufacturer were listed below:

$$U_T=1^\circ\text{C} (=1 \text{ K})$$

$$U_D=0.03 \text{ mm}$$

$$U_{\tau}=0.001 \text{ s}$$

$$U_{V/V}=0.05$$

$$U_{q/q'}=0.05$$

The average values of the direct measured variables at a particular state were listed below:

$$T_\infty=280.15 \text{ K}$$

$$T_w=263.15 \text{ K}$$

$$D=2 \text{ mm}$$

$$t=20 \text{ s}$$

Propagation of Uncertainties

The uncertainties in the individual variables propagate through a data reduction equation into a result. Consider a general case in which an experimental result, ζ , is function of J variables Λ_j

$$\zeta = \zeta(\Lambda_1, \Lambda_2, \dots, \Lambda_j) \quad (\text{B.1})$$

This equation is the data reduction equation used for determining r from the measured values of the variables Λ_j . Then the uncertainty in the result is given by

$$U_\zeta = \left[\left(\frac{\partial \zeta}{\partial \Lambda_1} U_{\Lambda_1} \right)^2 + \left(\frac{\partial \zeta}{\partial \Lambda_2} U_{\Lambda_2} \right)^2 + \dots + \left(\frac{\partial \zeta}{\partial \Lambda_j} U_{\Lambda_j} \right)^2 \right]^{1/2} \quad (\text{B.2})$$

where the U_{Λ_j} are the uncertainties in the measured variables.

It is assumed that the measured variables Λ_j are independent of one another, and that the uncertainties in the measured variables are independent of one another.

The partial derivatives are defined as “absolute sensitivity coefficients”.

$$\beta_j = \frac{\partial \zeta}{\partial \Lambda_j} \quad (\text{B.3})$$

When the data reduction equation has the form

$$\zeta = \kappa \Lambda_1^{\kappa_1} \Lambda_2^{\kappa_2} \Lambda_3^{\kappa_3} \dots \quad (\text{B.4})$$

where the exponents may be positive or negative constants and k is a constant, the general uncertainty analysis equation becomes

$$\left(\frac{U_{\zeta}}{\zeta}\right)^2 = \kappa_1^2 \left(\frac{U_{\Lambda_1}}{\Lambda_1}\right)^2 + \kappa_2^2 \left(\frac{U_{\Lambda_2}}{\Lambda_2}\right)^2 + \kappa_3^2 \left(\frac{U_{\Lambda_3}}{\Lambda_3}\right)^2 + \dots \quad (\text{B.5})$$

In this experimental investigation, material properties were not measured, but rather were found from reference sources, which were typically tabulated as a function of temperature. Those values were not the true values and have uncertainties associated with them. All of the thermophysical properties were estimated with curvefit equations obtained from National Bureau of Standards Circular 564(1955).

For the air obeying the ideal gas model, thermal conductivity, density, and kinematic viscosity depend only on temperature, thus

$$k(T) = 0.024061794 + 7.5939994 \times 10^{-5} \cdot (T - 273.15) \quad (\text{B.6})$$

$$\nu(T) = -2.2938017 \times 10^{-5} + 3.6276317 \times 10^{-5} \cdot e^{(T-273.15)/417.58729} \quad (\text{B.7})$$

$$\rho(T) = 0.63370723 + 0.65832423 \cdot e^{(T-273.15)/139.31335} \quad (\text{B.8})$$

If we entered the air property table at a node temperature several times, each of the values would be the same—there would be a zero precision limit associated with the value that we read from the table. This was the case regardless of the amount of scatter in the experimental data on which the table was based.

In this study, we assumed that all of the errors (both precision and bias) in the experimental property data were brought about by the measured variable, or temperature.

The general uncertainty analysis equations have the forms

$$U_k = \left(\frac{\partial k}{\partial T} \right) U_T = 7.5939994 \times 10^{-5} U_T \quad (\text{B.9})$$

$$U_v = \left(\frac{\partial v}{\partial T} \right) U_T = \left(\frac{3.6276317 \times 10^{-5}}{417.58729} \right) e^{\frac{(T-273.15)}{417.58729}} U_T \quad (\text{B.10})$$

$$U_p = \left(\frac{\partial p}{\partial T} \right) U_T = \left(\frac{0.65832423}{139.31335} \right) e^{\frac{T-273.15}{139.31335}} U_T \quad (\text{B.11})$$

If $U_T = 1^\circ\text{C}$, $T_\infty = 280.15 \text{ K}$, then

$$U_k = 7.59 \times 10^{-5}$$

$$U_v = 8.83 \times 10^{-8}$$

$$U_p = 4.97 \times 10^{-3}$$

Reynolds Number

Air flows over a horizontal flat surface as shown in Figure 3.1. How accurately could the Reynolds number be determined if the temperature was measured with an uncertainty of 1°C , the length was measured with an uncertainty of 0.03mm , and the velocity was measured with an uncertainty of 5% ?

The data reduction equation is

$$\text{Re} = \frac{V \cdot D}{\nu} \quad (\text{B.12})$$

and the general uncertainty analysis expression is

$$\frac{U_{\text{Re}}^2}{\text{Re}^2} = \left(\frac{U_V}{V}\right)^2 + \left(\frac{U_D}{D}\right)^2 + \left(\frac{U_\nu}{\nu}\right)^2 \quad (\text{B.13})$$

Values for the variables are: $U_T=1^\circ\text{C}$ ($=1\text{ K}$), $T=280.15\text{ K}$, $\nu=1.4\text{e-}5\text{ m}^2/\text{s}$, $U_\nu=8.85\text{e-}8$, $U_V/V=0.05$, $U_D=0.03\text{ mm}$, and $D=2\text{ mm}$. Substitution of the numerical values into equation yields

$$\frac{U_{\text{Re}}^2}{\text{Re}^2} = 0.05^2 + \left(\frac{0.03}{2}\right)^2 + \left(\frac{8.85\text{E-}8}{1.4\text{E-}5}\right)^2 \quad (\text{B.14})$$

$$\frac{U_{\text{Re}}}{\text{Re}} = 0.053 \text{ or } 5.2\% \quad (\text{B.15})$$

Air-side Convection Coefficient

The data reduction equation for the convection coefficient is

$$h = \frac{q''}{T_\infty - T_w} \quad (\text{B.16})$$

and the general uncertainty analysis expression is

$$\frac{U_h^2}{h^2} = \left(\frac{U_{q''}}{q''}\right)^2 + \left(\frac{U_{T_\infty}}{T_\infty - T_w}\right)^2 + \left(\frac{U_{T_s}}{T_\infty - T_w}\right)^2 \quad (\text{B.17})$$

if $U_{q''}/q''=5\%$, $U_{T_\infty}=U_{T_s}=1^\circ\text{C}$, $T_\infty=280.15\text{ K}$, $T_w=263.15\text{ K}$

$$\frac{U_h^2}{h^2} = 0.05^2 + \left(\frac{1}{17}\right)^2 + \left(\frac{1}{17}\right)^2 = 0.00942 \quad (\text{B.18})$$

$$\frac{U_h}{h} = 0.097 \text{ or } 9.7\%. \quad (\text{B.19})$$

Nusselt Number

The data reduction equation for Nusselt number is

$$\text{Nu} = \frac{hD}{k} \quad (\text{B.20})$$

and the general uncertainty analysis expression is

$$\frac{U_{\text{Nu}}^2}{\text{Nu}^2} = \left(\frac{U_h}{h}\right)^2 + \left(\frac{U_D}{D}\right)^2 + \left(\frac{U_k}{k}\right)^2 \quad (\text{B.21})$$

values for the variables are: $U_T=1^\circ\text{C}$, $T_\infty=280.15 \text{ K}$, $k=0.0246 \text{ W/m}\cdot\text{K}$, $U_k=7.59\text{E-}5$.

Substitution of the numerical values into equation yields

$$\frac{U_{\text{Nu}}^2}{\text{Nu}^2} = (0.097)^2 + \left(\frac{0.03}{2}\right)^2 + \left(\frac{7.5\text{E-}5}{0.0246}\right)^2 = 0.0096432 \quad (\text{B.22})$$

$$\frac{U_{\text{Nu}}}{\text{Nu}} = 0.0982 \text{ or } 9.82\% \quad (\text{B.23})$$

Am Number

The data reduction equation for Am number is

$$\text{Am} = \frac{k(T_{\infty} - T_w)}{\rho V^3 D} \quad (\text{B.24})$$

and the general uncertainty analysis expression is

$$\frac{U_{\text{Am}}^2}{\text{Am}^2} = \left(\frac{U_k}{k}\right)^2 + \left(\frac{U_D}{D}\right)^2 + \left(\frac{U_{\rho}}{\rho}\right)^2 + \left(\frac{U_{T_{\infty}}}{T_{\infty} - T_w}\right)^2 + \left(\frac{U_{T_w}}{T_{\infty} - T_w}\right)^2 + 9 \cdot \left(\frac{U_V}{V}\right)^2 \quad (\text{B.25})$$

values for the variables are: $U_{T_{\infty}} = U_{T_w} = 1^{\circ}\text{C}$, $T_{\infty} = 280.15\text{ K}$, $T_w = 263.15\text{ K}$, $\nu = 1.4\text{e-}5\text{ m}^2/\text{s}$, $U_{\nu} = 8.85\text{e-}8\text{ m}^2/\text{s}$, $U_V/V = 0.05$, $U_D = 0.03\text{ mm}$, and $D = 2\text{ mm}$, $k = 0.0246\text{ W/m}\cdot\text{K}$, $U_k = 7.59 \times 10^{-5}$, $U_{\rho} = 4.97 \times 10^{-3}$, $\rho = 1.23\text{ kg/m}^3$. Substitution of the numerical values into equation yields

$$\frac{U_{\text{Am}}^2}{\text{Am}^2} = \left(\frac{7.59 \times 10^{-5}}{0.0246}\right)^2 + \left(\frac{0.03}{2}\right)^2 + \left(\frac{4.97 \times 10^{-3}}{1.23}\right)^2 + 2\left(\frac{1}{17}\right)^2 + 9(0.05)^2 \quad (\text{B.26})$$

$$\frac{U_{\text{Am}}}{\text{Am}} = 0.0847 \text{ or } 8.47\% \quad (\text{B.27})$$

$\tau(\text{Fo Pe})_L$

The data reduction equation for τ is

$$\tau = \frac{Vt}{D} \quad (\text{B.28})$$

and the general uncertainty analysis expression is

$$\frac{U_\tau}{\tau} = \left(\frac{U_V}{V}\right)^2 + \left(\frac{U_D}{D}\right)^2 + \left(\frac{U_t}{t}\right)^2 \quad (\text{B.29})$$

values for the variables are: $U_V/V=0.05$, $U_D=0.03$ mm, and $D=2$ mm, $U_t=0.001$ s, $t=20$ s.

Substitution of the numerical values into equation yields

$$\frac{U_\tau}{\tau} = (0.05)^2 + \left(\frac{0.03}{2}\right)^2 + \left(\frac{0.001}{20}\right)^2 \quad (\text{B.30})$$

$$\frac{U_\tau}{\tau} = 0.0522 \text{ or } 5.22\% \quad (\text{B.31})$$

Stefan Number

The data reduction equation for Stefan number is

$$\text{Ste} = \frac{k_s(T_f - T_w)}{h_{sf}} \quad (\text{B.32})$$

and the general uncertainty analysis expression is

$$\frac{U_{\text{Ste}}}{\text{Ste}} = \left(\frac{U_{k_s}}{k_s}\right)^2 + \left(\frac{U_{h_{sf}}}{h_{sf}}\right)^2 + \left(\frac{U_{T_f}}{T_f - T_w}\right)^2 + \left(\frac{U_{T_w}}{T_f - T_w}\right)^2 \quad (\text{B.33})$$

values for the variables are: $U_{T_f} = U_{T_w} = 1^\circ \text{C}$, $T_f=273.15 \text{ K}$, $T_w=263.15 \text{ K}$. Substitution of the numerical values into equation yields

$$\frac{U_{\text{ste}}}{\text{Ste}} = 0.072 \text{ or } 7.2 \% \quad (\text{B.34})$$

VITA

Ying Gong was born on August 20, 1962 in the town of Mishan, Heilongjiang, China. His parents are Xiangshan Gong and Lanzhen Han. He has been married to Youhong Chen since May 1989.

He graduated from Jiaotong University, Xi'an, China in July 1983 with a Bachelor of Science degree in Mechanical Engineering. He then worked for the General Machinery Research Institute, China. In 1985, he went back to Jiaotong University for his Master of Science degree in Mechanical Engineering and completed it in 1988. Following this, he was employed as a Research Engineer with the Design Institute of the Ministry of Commerce, China. In 1992, he came to Florida International University for further education. He transferred to Texas A&M University in Spring, 1993 to pursue his doctoral degree in mechanical engineering.

His research interests include heat and mass transfer, computational fluid dynamics, phase change, latent heat of fusion thermal energy storage, electronic equipment cooling device, heating, ventilating, air-conditioning, and refrigeration.

His permanent mailing address is in China:

Ying Gong

1-46-403

Jiaotong University

Xi'an, Shaanxi 710048

P. R. China